Titre: Title:	Local Coils and Prospective Shimming for MRI of the Spinal Cord
Auteur: Author:	Ryan Topfer
Date:	2021
Type:	Mémoire ou thèse / Dissertation or Thesis
Référence: Citation:	Topfer, R. (2021). Local Coils and Prospective Shimming for MRI of the Spinal Cord [Ph.D. thesis, Polytechnique Montréal]. PolyPublie. https://publications.polymtl.ca/10011/

URL de PolyPublie: PolyPublie URL:	https://publications.polymtl.ca/10011/
Directeurs de recherche: Advisors:	Julien Cohen-Adad
Programme: Program:	Génie biomédical

POLYTECHNIQUE MONTRÉAL

affiliée à l'Université de Montréal

Local coils and prospective shimming for MRI of the spinal cord

RYAN TOPFER

Institut de génie biomédical

Thèse présentée en vue de l'obtention du diplôme de *Philosophiæ Doctor*

Génie biomédical

Décembre 2021

POLYTECHNIQUE MONTRÉAL

affiliée à l'Université de Montréal

Cette thèse intitulée :

Local coils and prospective shimming for MRI of the spinal cord

présentée par **Ryan TOPFER**

en vue de l'obtention du diplôme de *Philosophiæ Doctor*

a été dûment acceptée par le jury d'examen constitué de :

Nikola STIKOV, président
Julien COHEN-ADAD, membre et directeur de recherche
Sylvain MARTEL, membre
David RUDKO, membre externe

DEDICATION

For my grandparents.

ACKNOWLEDGEMENTS

Wisdom, goes the Confucian aphorism, *may be learned by three methods: by reflection, which is noblest; by imitation, which is easiest; and by experience, which is the bitterest.*

While the letters "PhD" hardly pass as bona fides of wisdom, each of The Three Methods nevertheless played a role in acquiring the lesser wisdoms of knowledge and competence demanded by this doctorate. Indeed, the scientific cycle of *expériences* (sometimes bitter failures) and subsequent reflection formed the engine that, griding away, eventually produced positive results. However, as the easiest method, imitation was at least as important.

During the PhD, I was privileged to work with a great group of scientists and engineers whose talents I tried to imitate. It is neither as flattery nor with any exaggeration to say this work would not have materialised were it not for their instruction, support and, in many cases, direct involvement. As eminent MR scientist Klaas Pruessmann said about his work with Johanna Vannesjo when I had the pleasure of interviewing them for *MRM Highlights*, "As is probably evident, no single person could ever think of doing all this alone."

An emboldened **Thank you** is owed...

To my supervisor Prof. Julien Cohen-Adad, first and foremost, for his hand in literally every aspect of this project. Recalling our first real experiment (shimming a shampoo bottle), we were hoping to come away with some dazzling results for our first ISMRM submission but, after many hours, midnight passed and my attempts at demonstrating improved shimming had only deteriorated it, along with my morale. Feeling defeated, I was ready quit, but Julien insisted we persevere. We soon spotted the problem in my code (a missing minus sign, of course) and, lo and behold, upon the correction, my shim program *actually* worked! The abstract was drafted and submitted the next day.

Few things are as rewarding as realizing one's own ability to comprehend and practically solve a challenging problem. Thus, while an additional appendix would be necessary to exhaustively give thanks and sing Julien's praises, I will instead rely on this emblematic anecdote as supporting evidence of the quality for which I feel the greatest indebtedness: Julien's unfailing resolve to get me—often despite myself—to see things through. For the all the opportunities over the years, and for all the support that enabled them to be so rewarding, I am deeply grateful.

To Prof. Nikola Stikov for his intellectual contributions to this work, for his initiative creating and coordinating *MRM Highlights* (every interview I conducted was a delight and I never failed to learn something), for his refreshingly candid critiques of academic publishing, and for the enriching opportunity to assist in teaching the class on emerging biomedical technologies. Nikola is a model teacher who every university lecturer would do well to imitate.

To collaborators at the A.A. Martinos Center: Prof. Larry Wald, Prof. Jason P. Stockmann, Nicholas Arango and Thomas Witzel for their intellectual and material contributions (especially the shim driver boards used in Chapter 6). Special thanks are owed to Jason for serving as a mentor throughout this project, generously sharing his time and his expertise. Whether in the lab in Charlestown or at an ISMRM meeting, even a casual observer could not fail to see that Jason is universally appreciated as a colleague and admired as model scientist.

To André Cyr and Carollyn Hurst at UNF, where all our experiments took place. For their diligent assistance carrying out experiments, and for their patient guidance as instructors in all the operational aspects of MRI, this work and I, personally, benefited greatly.

To collaborators at Resonance Research Inc.—Piotr Starewicz, Kai-Ming Lo, Donald Jette, Karl Metzemaekers. The shim system at the centre of this work was a product of their artful design and skilled manufacturing work.

To labmates:

Especially, to master RF and electronics engineers Nibardo Lopez-Rios and Alexandru Foias for their practically countless contributions (especially regarding the design and construction of the AC/DC hardware discussed Chapter 6). Also, to masters students and former interns at the lab who also contributed directly to these studies: Grégoire, Aurélien, Angel, Axel, Alexandre, Gaspard.

To everyone else at the lab for all the stimulating discussions over the years: Atef, Agah, Aldo, Ariane, Augustin, Benjamin, Charley, Cyril, Darya, Dominique, Eva, Gabriel, Harris, Ilana, Lucas, Mathieu, Melanie, Nick, Nicolas, Olivier, Sara, Simon, Stephanie, Tanguy, Tommy, Tung, Uzay, William... I learned a great deal from working with everyone and hope the exchange was mutual!

To Daniel Papp special thanks are owed for his many important interventions in drafting this dissertation: for his lucid editing, and for his kindness and good sense to talk me off the proverbial cliff in a moment of dissertation despair.

To all the administrative staff at Polytechnique Montréal and particularly to Amal Bennani for all their work behind the scenes.

To the additional committee members, Prof. Sylvain Martel and Prof. David Rudko, for their time and thoughtful evaluations of the dissertation. And to Prof. David Ménard for his helpful role as DESS representative during the defence.

To Prof. Alan Wilman, Prof. Rob Barry, Prof. Rick Hoge, Prof. Hongfu Sun, and to Paul Weavers, who each offered thoughtful advice.

To my partner Sine, to my family, and to my friends for their love and encouragement.

To my dear friend Jeremy Nischuk (1980-2020), who several times came through on short notice to volunteer for scans, I am deeply grateful for your support, your art, your friendship. Your presence is sorely missed.

Finally, to all the volunteers who, in the interest of science, kindly agreed to lay still in a narrow tube for an hour while we tested our coils.

RÉSUMÉ

Plus de 85,000 de canadiens sont victimes des pathologies de la moelle épinière dont les effets peuvent impliquer des difficultés motrices, sensorielles, et fonctionnelles. Le développement de biomarqueurs quantitatifs pourrait permettre les médecins de mieux prédire les résultats de traitements médicaux pour les pathologies de la moelle épinière afin de mieux les adapter aux patients individuels. À cet effet, l'imagerie par résonance magnétique (IRM) pourrait servir grâce à sa capacité unique à générer plusieurs contrastes d'images qui, en fonction des paramètres d'acquisition, peuvent être adaptés afin de refléter diverses propriétés tissulaires et processus physiologiques.

La moelle épinière présente un défi pour les techniques l'IRM avancées. Au sein de son environnent anatomique, la susceptibilité magnétique est très hétérogène, ce qui conduit à des variations importantes du champ magnétique (B_0) dans la moelle épinière elle-même. Ceux-ci entraînent fréquemment une variété d'artefacts d'image tels que la perte de signal et la distorsion géométrique. De plus, en raison de sa proximité aux poumons, la moelle épinière est soumise à des variations temporelles du champ B_0 liées à la respiration du patient, ce qui peut entraîner encore plus d'artefacts (par exemple, des problèmes de flou et d'incohérence de signal). De fait, plusieurs des méthodes d'IRM qui ont été développées pour le cerveau (par exemple, l'IRM fonctionnelle, l'IRM de diffusion, et l'imagerie spectroscopique) ne fonctionnent pas aussi bien au niveau de la moelle épinière.

L'élimination de la variation de champ magnétique statique (généralement connue sous le nom de « shimming ») est généralement effectuée à l'aide de réseaux de grandes bobines inductives intégrées dans le scanner IRM. Bien qu'utile, la correction conventionnelle reste insuffisante pour la moelle épinière.

Pour répondre aux défis de l'inhomogénéité du champ B_0, ce projet comprend le développement de nouveaux appareils (des matrices de shims locaux) dédiés à la moelle épinière et de nouvelles stratégies d'optimisation (une correction prospective qui combat les effets de la respiration en temps-réel). En conséquence, des améliorations aux images écho-gradient (GRE) et écho-planaires (EPI) sont démontrées.

ABSTRACT

Over 85,000 Canadians suffer from pathologies of the spinal cord—a condition that often entails motor, sensory, or functional losses. The development of quantitative imaging biomarkers could provide physicians with a better means of predicting treatment outcomes, for instance, to avoid unnecessary surgeries. To this purpose, magnetic resonance imaging (MRI) could prove useful given its ability to produce a variety of image contrasts which, by adjusting the acquisition parameters, can be tailored to reflect a range of tissue properties and physiologic functions.

The spinal cord presents a challenge to advanced MRI techniques. The magnetic susceptibility of its anatomical surroundings is highly heterogeneous, which leads to significant magnetic field (B_0) variation in the spinal cord itself. This frequently results in a variety of image artifacts, such as signal loss and geometric distortion. Moreover, the proximity of the spinal cord to the lungs produces significant temporal field variation during respiration which can result in additional problems such as blurred images and inconsistent signal measurements. As a result, many of the advanced MRI techniques developed for the brain (e.g., functional fMRI, diffusion, and spectroscopic imaging) remain impractical for the spinal cord.

Eliminating static magnetic field variation (generally known as *shimming*) is commonly performed using arrays of large inductive coils integrated into the MRI scanner. While useful, conventional static shimming nevertheless remains inadequate for the spinal cord.

To address the challenges of B_0 field inhomogeneity, this work aims to develop new approaches to shimming to meet the particular the demands of MRI of the spinal cord. Through the use of new dedicated hardware (local shim arrays) and tailored optimization strategies (e.g. real-time/prospective shimming to combat the effects of respiration), improvements to gradient-echo (GRE) and echo-planar images (EPI) are demonstrated.

TABLE OF CONTENTS

LIST OF FIGURES

LIST OF SYMBOLS AND ABBREVIATIONS

AC	Alternating current
B_0	Longitudinal magnetic field strength
DC	Direct current
FID	Free induction decay
FOV	Field of view
EPI	Echo-planar imaging
GRE	Gradient-recalled echo
MC	Multi-coil
MR	Magnetic resonance
MRI	Magnetic resonance imaging
NMR	Nuclear magnetic resonance
RF	Radio frequency
RIRO	Respiration-induced resonance offset
ROI	Region of interest
Rx	Receiver (RF)
SH	Spherical harmonics
SNR	Signal-to-noise ratio
T	Tesla (unit)
T_1	Longitudinal spin-lattice relaxation time
T_2	Transverse spin-spin relaxation time
T_2^*	Effective transverse relaxation time
Tx	Transmitter (RF)
VOI	Volume of interest
Voxel	Volume-element

CHAPTER 1 INTRODUCTION

1.1 Project motivation

Disorders of the spinal cord are a common cause of pain and functional disability (e.g. mobility loss). An estimated 85,000 Canadians are afflicted by some form of spinal cord pathology due either to injury, degeneration with age, or disease.(1)

As a noninvasive means to examine the internal structures of the body (and one which avoids the use of ionizing radiation) magnetic resonance imaging (MRI) is routinely used in clinical medicine to help diagnose spinal cord pathologies. In a survey of 26 clinical MRI units across Canada, the spine was found to be the second-most frequently targeted anatomic region, accounting for roughly one-fifth of all MRI exams.(2)

However, this survey also found that nearly a third of MRI scans targeting the spine were *inappropriate* i.e., with requisitions in violation of official radiological guidelines.(2) For comparison, among requisitioned brain scans, merely 2-3% were considered inappropriate. Such a designation not only incorporates concerns of MRI scan cost-effectiveness but also, and more seriously, concerns of exposing the patient to undue risk (i.e. despite the generally accepted safety of the MRI scan itself). For common conditions such as generic lower back pain and degenerative cervical myelopathy, standard structural MR images are largely nonspecific (abnormalities apparent in the images do not necessarily correlate with clinical condition) and the poor interpretability of these images risks leading to overdiagnosis, and unnecessary tests and treatments (e.g. drug prescriptions and surgeries).(3) Still, absent a better alternative, patients and physicians often want the MRI scan (4) and, thus, inappropriate scanning persists despite the established guidelines.

To address this problem a meaningful alternative to conventional MRI is needed. Fortunately, as a uniquely flexible imaging modality, MRI permits a variety of image contrasts beyond the standard arsenal of T_1-, T_2-, and proton-density weighted images; several semi-quantitative methods have been proposed as alternatives, such as diffusion-tensor and magnetization transfer imaging.(5–7) However promising, these advanced techniques remain challenging in the context

of the spinal cord due to image artifacts associated with magnetic field inhomogeneity, the elimination of which is the subject of this dissertation.

1.2 Background (MRI physics)

The bulk of the typical MRI scanner consists of a superconducting electromagnet designed to produce a strong uniform magnetic field $B_0\hat{\mathbf{z}}$ (i.e. along the longitudinal axis of the bore). To illustrate the significance of B_0-homogeneity the following sections briefly review the steps conventionally involved in imaging the body by magnetic resonance (MR).

1.2.1 Nuclear magnetic dipoles

The ability of MRI to noninvasively image the interior of the body owes to its abundant water content and, more specifically, to the intrinsic properties of the protons that make up each of two hydrogen nuclei of the H_2O molecule. Due to its magnetic dipole moment ($\sim 10^{-26}\ \mathrm{J \cdot T^{-1}}$), the proton acts rather like a tiny magnet (a *nuclear magnetic dipole*): as a magnetic source, its field can be detected at a distance (e.g. with sensors positioned outside the body); and, as a magnetic subject, the nuclear dipole will respond to an applied magnetic field (e.g. the B_0 field of the MRI scanner).

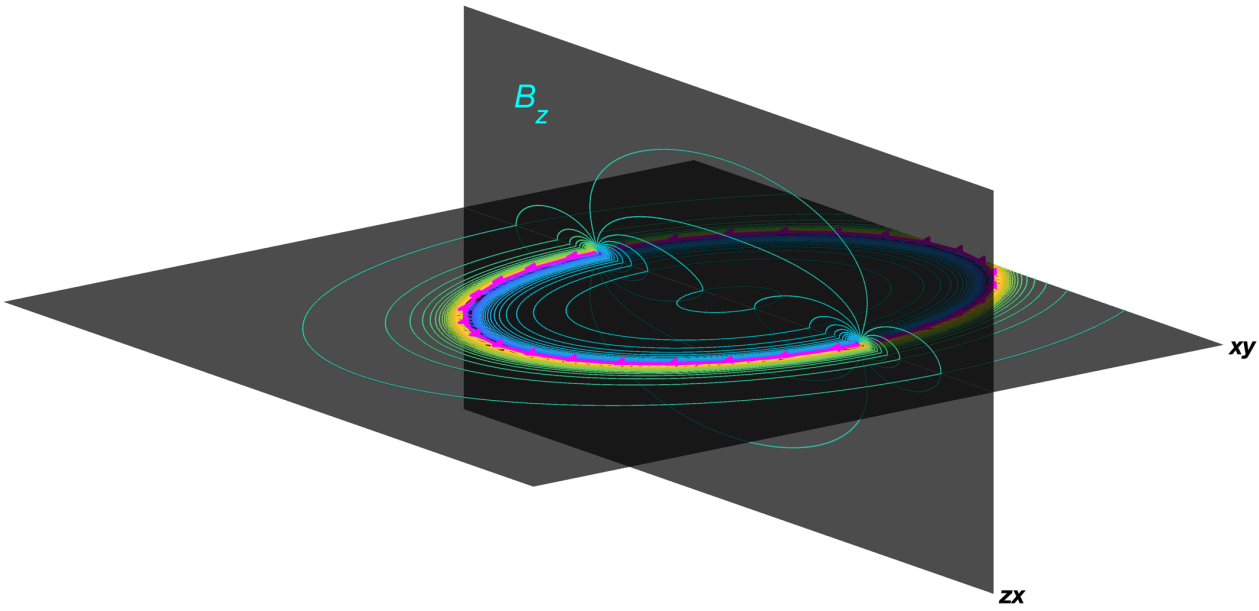

Figure 1.1: B_z magnetic field lines of a loop of current (magenta arrows) circulating in the *xy*-plane.

1.2.2 Larmor precession

Ordinarily, a magnetic dipole initially at rest would be expected to settle into alignment with a constant external field (e.g. the consistent manner in which a compass-needle points north); however, due to the intrinsic *spin angular momentum* of the proton, the nuclear magnetic dipoles behave differently. Instead of falling into a fixed orientation, the nuclear magnetic dipoles exhibit a gyroscopic motion: unless disrupted by other interactions, the dipoles will precess around $B_0\hat{\mathbf{z}}$ at a constant rate—the Larmor frequency:

$$\omega_0 = \gamma B_0. \qquad [1.1]$$

The proportionality constant relating ω_0 to B_0 is the proton gyromagnetic ratio $\gamma \approx 2.675 \cdot 10^8 \text{ rad} \cdot \text{s}^{-1} \cdot \text{T}^{-1}$ (the ratio between the magnetic moment and the spin angular momentum).

Thus, the precessing nuclear dipoles are sources of time-varying magnetic fields that will ultimately be detected as voltages induced in receiver (Rx) coils tuned to the Larmor frequency. Under normal circumstances, however, the dipoles tend to orient more-or-less randomly such that their fields, when observed at a distance, tend to cancel out. To enable their detection, a sufficient number of spins must first be brought into phase—a task that requires some preparation.

1.2.3 Nuclear magnetization

The preliminary step is to induce a *nuclear magnetization* in the body of the subject, i.e. to bring about a net alignment of the proton spins whereupon the magnetic fields of some spins—individually minuscule, and erstwhile mutually canceling—partially add up. Magnetization is accomplished passively as the subject enters the strong B_0 field permeating the bore of the MRI scanner. Denoting the proton density as $\rho(\mathbf{r})$, with position-vector $\mathbf{r} = x\hat{\mathbf{x}} + y\hat{\mathbf{y}} + z\hat{\mathbf{z}}$, the longitudinal component of the nuclear magnetization at thermal equilibrium is

$$M_0(\mathbf{r}) \approx \frac{\rho(\mathbf{r})\gamma^2\hbar^2}{4kT} B_0 \qquad [1.2]$$

The product of the temperature T and the Boltzmann constant k in the denominator suggests that thermal energy stymies the formation of M_0 and, since the other terms in the numerator are given,

the only option to increase M_0 for a living subject is to increase B_0 (which, for superconducting clinical scanners is commonly between 1.5-3.0 T).

1.2.4 Excitation

While the nuclear magnetization amounts to a slight shift in the static magnetic field, detecting this change directly would be difficult as it tends to be smaller than the achievable stability of the applied field used to generate it (for operative superconducting systems, B_0 is *always on*). To probe the magnetization, it is necessary to torque it away from the main field and into the transverse plane; as its constituent spins continue to precess around B_0, the transverse magnetization is thus observed to rotate around the z-axis at the Larmor frequency for a time as the system gradually returns to its initial equilibrium. The process of torquing M_0 into the transverse plane is dubbed *excitation* and it is accomplished by applying a brief RF pulse (a time-varying magnetic field, termed B_1) along a transverse axis, with the central frequency of the pulse matched to the Larmor frequency. The degree by which the nuclear magnetization is rotated is the *flip-angle*:

$$\alpha = \gamma \int_0^{\tau} B_1(t)\, dt \qquad [1.3]$$

1.2.4.1 Spatially selective excitation

To simplify the imaging process, excitation is typically restricted to a specific region of interest (either a "slice" or, less commonly, a "slab"). As illustrated in Figure 1.2, this is achieved by applying a linear magnetic field gradient G_z along the slice/slab dimension (say, the z axis, for axial imaging) for the duration of the RF pulse so as to distribute the local resonant frequency monotonically along z: $\omega(z) = \omega_0 + \gamma z G_z$. The central frequency of the B_1 pulse is chosen to coincide with the Larmor frequency at the targeted slice position z_0. For the received signal to be significant, the slice must be of a certain thickness to include enough spins; hence, the applied RF pulse spans a range of frequencies around a central frequency corresponding to the slice centre.

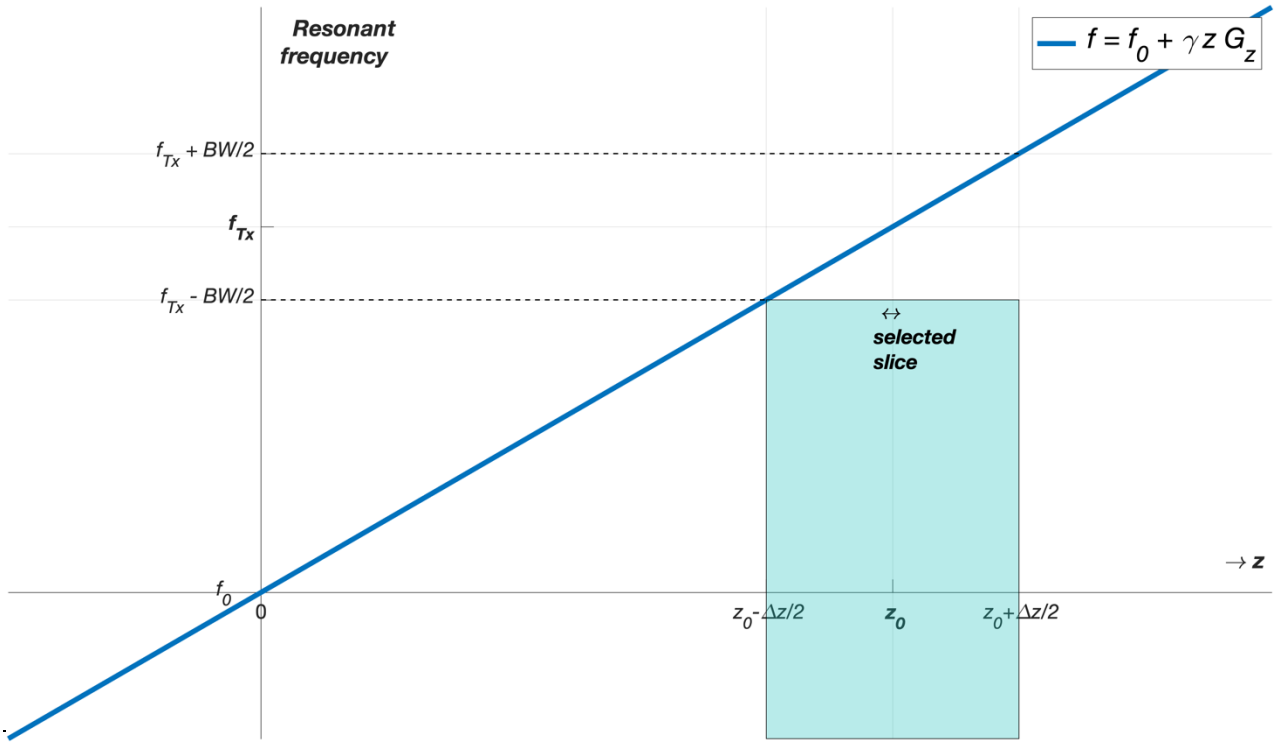

Figure 1.2: Ideal axial slice selection as a function of gradient strength G_z, RF excitation bandwidth BW and central frequency f_{Tx}.

1.2.5 Refocusing gradients

During the application of the (e.g. axial) slice-selection gradient, spins precess faster or slower depending on their distance along the excitation axis from the slice-centre (e.g. $\gamma G_z(z - z_0)$). This dephases spins within the excited slice which, if left uncorrected, leads to signal cancellation. This gradient-induced phase dispersion is readily refocused/rewound following excitation by applying a second gradient lobe with opposite polarity and with half the moment of the original.

1.2.6 Relaxation

As excitation ends, the system gradually returns to thermodynamic equilibrium, with **M** realigning along z: its regrowth is known as longitudinal relaxation and it follows an exponential curve, characterized by the so-called T_1 "spin-lattice" time-constant (how long it takes for the longitudinal magnetization to return to 63 % ($\approx 1 - 1/e$) of its initial value).

By recording the signal post-excitation one finds that the transverse signal decays faster than the longitudinal relaxation recovers. The gradual loss of transverse phase coherence is understood in terms of two processes:

First, the random motion of spins in the vicinity of other spins introduces small fluctuations to the local field, causing them to precess slightly faster or slower, however the moment takes them. Hence, the effective resonant frequency, rather than assuming a single value, tends to follow a Lorentzian distribution centred at γB_0. Dephasing due to this intrinsic coupling is dubbed spin-spin relaxation. Like its longitudinal counterpart, it exhibits exponential decay, characterized by the local T_2 constant (the time it takes for the transverse magnetization to decay by 37% ($\approx 1/\mathrm{e}$) from its initial maximum post-excitation). As the underlying process is stochastic, this dephasing is said to be *irreversible.*

Second, static fields that appear approximately constant over the diffusion length of a spin but which vary macroscopically across the sample lead to relative dephasing between spins in different positions. Insofar as the field variation remains essentially constant over time, this dephasing is *reversible* as spins can be brought back into phase, either by applying a 180° RF refocusing pulse, or, in certain cases, by applying an appropriate gradient pulse. Dephasing due to static field inhomogeneity ΔB_0 is dubbed T_2' and it is approximately equal to $(\gamma \Delta B_0)^{-1}$. As irreversible dephasing is ever-present, transverse dephasing is often summarized by the *effective* transverse relaxation time:

$$T_2^* \approx \left(\frac{1}{T_2} + \gamma \Delta B_0\right)^{-1} \qquad [1.4]$$

1.2.7 Signal model

Following excitation, the transverse magnetization can be understood as a distribution of magnetic oscillators: a collection of rotating magnets, each with a particular amplitude in proportion to local the transverse magnetization $M_{xy}(\mathbf{r})$ and a particular phase governed by the local Larmor frequency $\phi(\mathbf{r}, t) = \omega(\mathbf{r})t$. As a source of time-varying magnetic flux, the rotating magnetization can be detected via Faraday induction, i.e. as a time-varying voltage $s_r(t)$ induced in an RF receiver (Rx) coil. Omitting the weighting factors of relaxation and coil-sensitivity,

$$s_r(t) = \iiint M_{xy}(x,y,z)e^{-i\phi(x,y,z,t)}dxdydz \qquad [1.5]$$

In general, when the oscillations are in-phase, the detected signal is maximal; as the transverse magnetization drifts out of phase, local fields begin to cancel out and the recorded signal drops off.

1.2.8 Spatial encoding

The guiding principle behind MR imaging is that by superposing an appropriate magnetic field onto the main polarizing magnetic field, the Larmor frequency can be made to correspond to—and, therefore, *encode*—spatial position. Most often, localization is achieved by means of three independent *gradient coils*, each one generating an adjustable field $\mathbf{G_{i=x,y,z}}$ with a longitudinal component $G_i\hat{\mathbf{z}}$ that varies monotonically along a particular Cartesian axis, as illustrated in Figure 1.3. Under the action of the linear gradients, spin position $\mathbf{r}$ is mapped to precessional frequency ω via

$$\omega(\mathbf{r}) = \omega_o + \gamma\,\mathbf{r}\cdot(\mathbf{G_x} + \mathbf{G_y} + \mathbf{G_z}) \qquad [1.6]$$

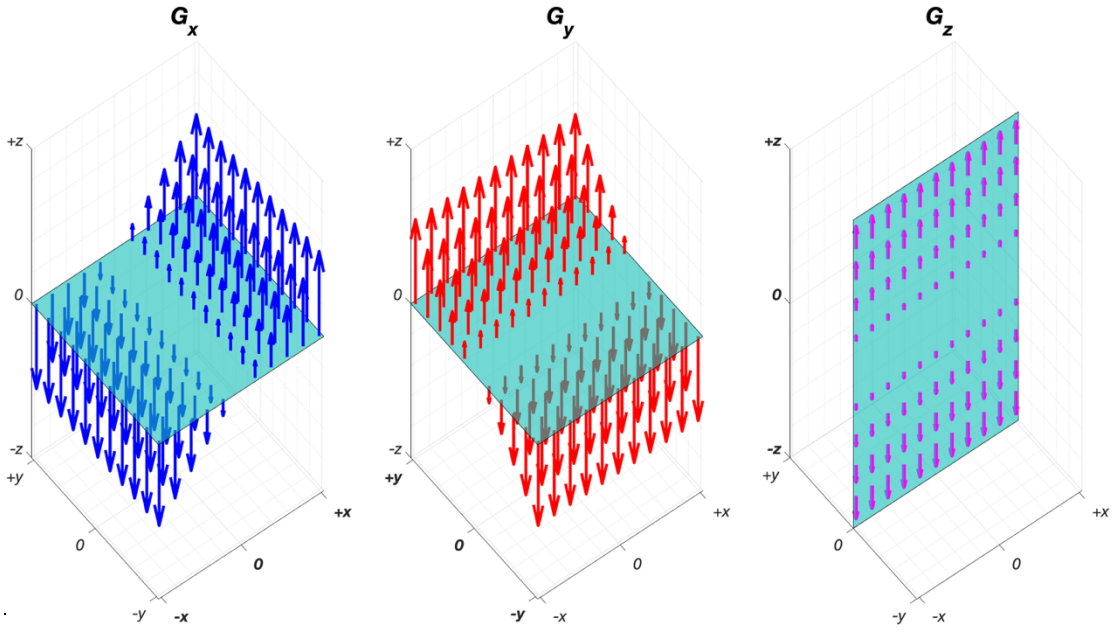

Figure 1.3: Gradient fields $\mathbf{G_x}$, $\mathbf{G_y}$, and $\mathbf{G_z}$. Each serves to vary the z-component of the static magnetic field in a precisely linear (monotonic) fashion along their respective axes. Arrow-

lengths indicate the relative field strengths (and, by extension, the resonance offsets) introduced by the gradient fields at different positions in the depicted slice planes.

Frequency encoding is the process of recording (a.k.a. "reading out") the signal in the presence of an applied encoding gradient. Relative magnitudes of the *x*-, *y*- and *z*-gradients determine the encoding axis along which Larmor frequencies are distributed, while spins along any orthogonal axis continue to precess at the same rate. To encode multiple spatial dimensions, the frequency encoding axis can be rotated between successive read-outs by adjusting the relative gradient strengths (a technique called radial imaging); more commonly, however, a single, fixed axis is selected for frequency encoding and the remaining imaging dimensions are, instead, *phase encoded*.

Phase encoding uses short gradient pulses to impart phase variation across the sample prior to frequency encoding and measurement. Once the gradient is removed, spins immediately return to the original Larmor frequency, however, the phase dispersion that accumulated during the pulse window will persist.

By definition, frequency f relates to the instantaneous rate of phase change as $2\pi f = d\phi/dt$, thus, frequency encoding can be understood as a form of phase encoding (the fact that the former occurs specifically during read-out is, in practice, the distinguishing factor). Figure 1.4 illustrates spatial encoding as a process of induced dephasing.

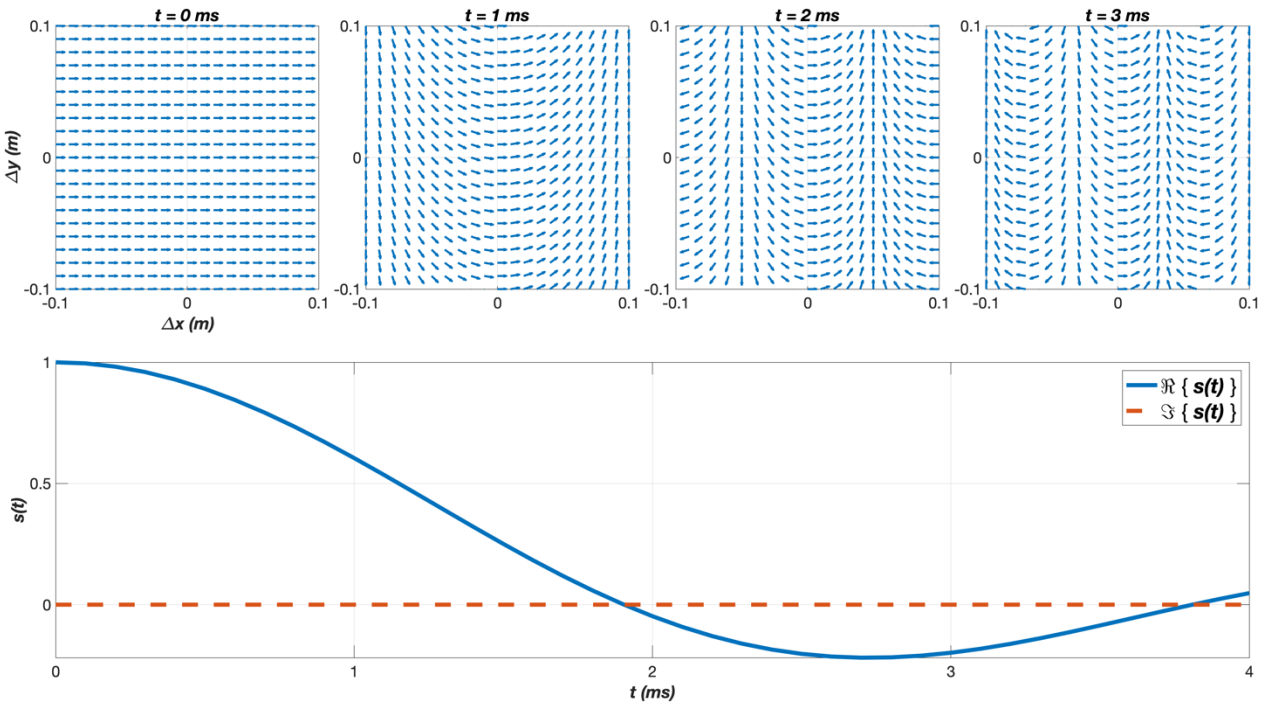

Figure 1.4: The principle of spatial encoding: by applying a symmetric linear magnetic field gradient G_x across the x-axis, the local transverse magnetization (in-phase everywhere at $t = 0$) rotates around z at a rate $\omega(x, y) = \omega_0 + \gamma x G_x$, resulting in relative dephasing across the encoding dimension as indicated by the arrow orientations. The bottom panel illustrates the corresponding signal *s(t)* induced in a receive coil: the more spins are in phase, the greater the flux passing through the coil.

1.2.9 k-space

The key to conventional (Cartesian) imaging is that by applying linear gradients to the transverse magnetization, relative dephasing comes to encode spatial position; as the imparted phase varies sinusoidally along each encoding axis, the encoding process can therefore be understood in terms of projections of the spin distribution onto the standard Fourier basis, i.e. sines and cosines of various spatial frequencies.

The *k-space formalism* provides a useful way of expressing the amount of gradient-induced dephasing applied (and thus, the effective spatial frequency of the projection) along each axis:

$$k_i(t) = \frac{\gamma}{2\pi} \int_0^t G_i(t')dt' \qquad [1.7]$$

The instantaneous phase of the signal during read-out (Eq. [1.5]) can then be expressed in terms of the local position in *k*-space $\phi(x, y, \mathrm{z}, t) = \mathbf{k} \cdot \mathbf{r}$ and the signal can be conveniently understood as a Fourier transform of the apparent transverse magnetization $\boldsymbol{M_{xy}}$ (i.e. the relaxation-weighted spin density). As the received voltage is generally digitized and stored as a numeric array, reconstructing an image of $\boldsymbol{M_{xy}}$ becomes a simple matter of performing a series of inverse fast-Fourier transforms along each array/encoding dimension.

Sampling requirements to obtain a particular image while avoiding aliasing are readily summarised as parameters of *k*-space: Along each of the encoded axes, the field of view is the inverse of the corresponding sampling interval $FOV_i = 1/\Delta k_i$, and voxel size δ_i is inversely proportional to the largest point recorded in k-space $\delta_i \approx 1/2k_{i-max}$.

As transverse phase coherence among the spins governs the net magnetic field, it limits the flux available to the receiver coils; therefore, measurements made in the outer portions of *k*-space—while necessary for higher resolution—generally see much less signal than those made in the central portion of *k*-space where more spins remain in-phase. With spectral energy narrowly concentrated around the centre of k-space, ensuring that the region is captured during read-out is especially important. Along the frequency-encoding axis, $k_{fe} = 0$ is often sampled by preceding the read-out gradient with a dephasing lobe of opposite polarity: when the dephasing moment is half that of the subsequent rephasing pulse, the sequence amounts to sweeping across the k_{fe} axis from one side to another. As spins are momentarily brought back in phase, a *gradient echo* is produced. The time between excitation and the echo formation is the *echo time TE.*

1.2.10 Pulse sequences

How the raw MRI data is acquired (i.e. how *k*-space is filled) is commonly described in terms of a *pulse sequence*. The latter typically consists of blocks of partially repeating subroutines, e.g. *Excitation → refocusing + phase encoding → frequency encoding + signal read-out.* The duration of the loop is defined by the interval between successive RF excitations: this is termed the *repetition time* and denoted by *TR*. Virtually every pulse sequence in use today incorporates additional modules (e.g. suppression pulses for fat and/or stimulated echoes, flow compensation and/or diffusion encoding gradients, etc.). As the variety of pulse sequences are myriad, a

comprehensive review is beyond the scope of this work. For the purpose of our discussion, descriptions of the two sequences given below will suffice.

GRE-FLASH (Gradient-Recalled Fast Low-Angle SHot (8)) follows the basic sequence-block outlined above, issuing one phase-encoding step each excitation. Low flip angles (~15º) are employed to permit short *TR* as the transverse magnetization quickly reaches a steady state. In a multi-echo GRE acquisition (such as the dual-echo variant depicted below in Figure 1.5), multiple echoes are formed either by using monopolar or bipolar read-out gradients. While monopolar read-outs (as depicted in the figure) requires longer periods between echoes for refocusing (thereby increasing minimum *TE*s), measurements tend to be more consistent across echoes than in the bipolar case.

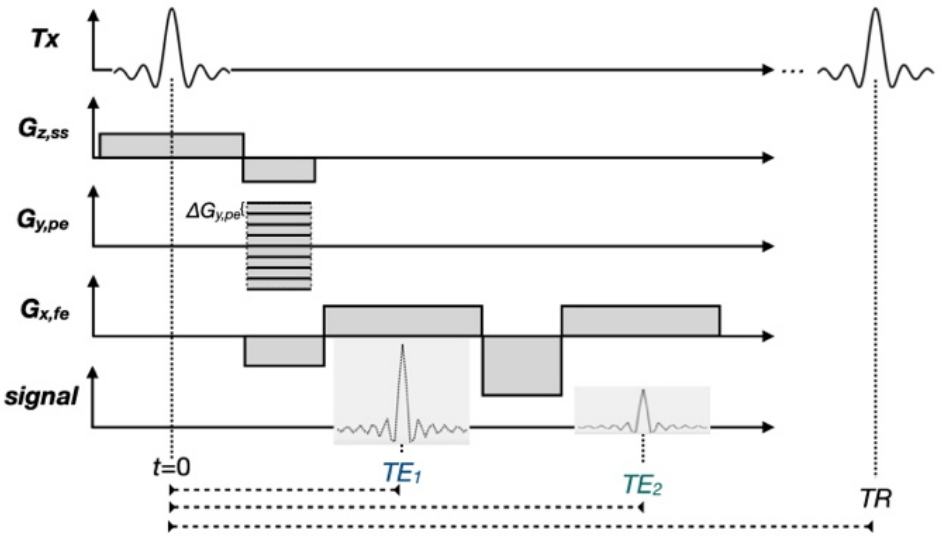

Figure 1.5: Dual-echo GRE pulse sequence diagram. Following each excitation (every *TR*) a single phase encoding step is performed and echoes are acquired at TE_1 and TE_2 via gradient refocusing.

2D-EPI (Echo-Planar Imaging) is a popular sequence where, in the "single-shot" variant, all the encoding stages are iterated through for a given slice between successive excitations. As the time to acquire a slice is typically on the order of 100 ms, volumes encompassing entire tissues can be covered in a matter of seconds. Due to its speed, the sequence serves as the workhorse to most functional and diffusion MRI studies. Figure 1.6 depicts a basic GRE-EPI sequence used in BOLD fMRI for its T_2^* weighting.

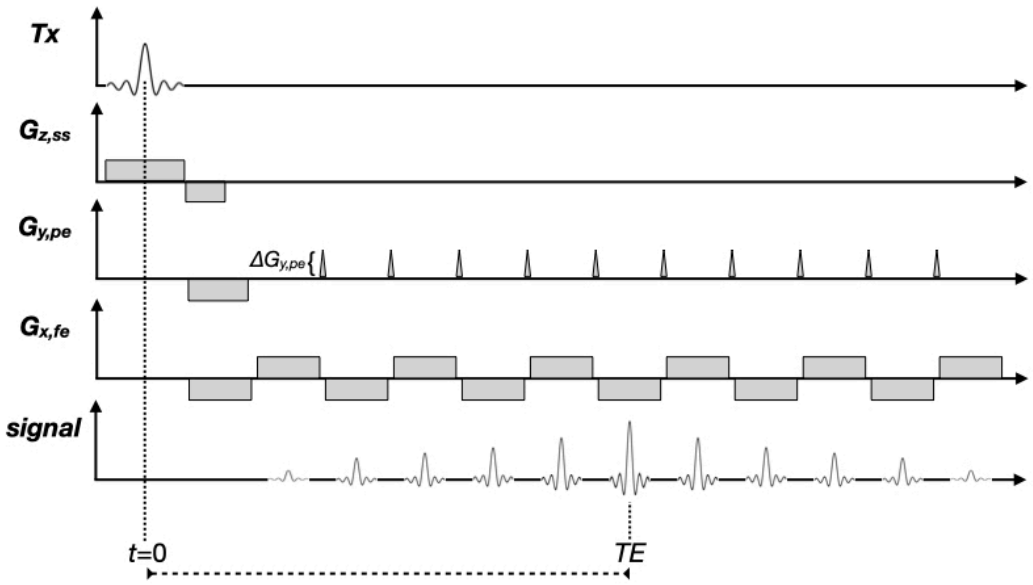

Figure 1.6: Single-shot GRE-EPI pulse sequence diagram. Initial gradient moments applied along the *x* and *y* axes place the starting measurements at the outer corner of *k-space* ($k_{x\text{-}min}$, $k_{y\text{-}min}$); the acquisition proceeds along a zig-zag trajectory in *k-space* by employing a bipolar read-out gradient and iterative phase-encoding "blips" to step between lines. *TE* denotes the central echo acquired at the *k*-origin.

1.3 The problem

Given the above description of MRI, the significance of controlling static field variation is readily apparent: the procedure generally presupposes that B_0 is initially uniform and that its later variation during a scan is strictly and deliberately induced (for instance, while gradient fields are applied for spatial encoding). In practice, however, this assumption is regularly violated: the closest B_0 ever comes to being a uniform constant is typically while the scanner sits empty as field deviations inevitably arise the moment a subject enters the bore.

1.3.1 Magnetic susceptibility

The extent to which a body will tend to alter an applied magnetic field is commonly described by its *magnetic susceptibility* χ.

In the human body, tissue susceptibilities tend to fall within $\pm 20\%$ of the susceptibility of water at body-temperature $\chi_{H2O@37^\circ} \approx -9.6 \cdot 10^{-6}$ and are, therefore, considered diamagnetic ($\chi < 0$).

(9) The observed variation depends mainly on the distribution of certain paramagnetic ($0 < \chi < 1$) molecules and ions (e.g. O_2, Fe^{3+}, Fe^{2+}) which generally appear in low concentrations throughout the body.

Most often, the maximum susceptibility encountered within the imaging volume is that of air, which, being roughly 20% O_2, is slightly paramagnetic ($\chi_{air} \approx 0.36 \cdot 10^{-6}$). While these small susceptibilities produce maximum field shifts on the order of several *ppm*, these seemingly small field differences lead to troublesome spatial variation in local resonant frequencies.

For conditions encountered in MRI, the field distortions are approximately dipolar in form, i.e. $\Delta B(\mathbf{r})$ can be modeled from a distribution of magnetic dipoles, the field of each scaled by the local magnetic susceptibility $\chi(\mathbf{r}')$:

$$\Delta B(\mathbf{r}) \approx B_0\, \chi(\mathbf{r}') * \left\{ \frac{3cos^2\theta - 1}{|\mathbf{r} - \mathbf{r}'|^3} \right\} \qquad [1.8]$$

This expresses a 3D convolution ($*$) between the susceptibility distribution $\chi(\mathbf{r}')$ and, in curly brackets, the field of a unit-dipole placed at the origin and oriented along z; θ is the polar angle between the observation point $\mathbf{r}$ and the positive z-axis. The expression, valid for isotropic $\chi \ll 1$, describes the change in magnetic field observed at the nucleus due to susceptibility variation at a distance (i.e. it includes the so-called Lorentzian-sphere correction to account for the discontinuous nature of the magnetization).(10,11)

1.3.2 B_0 inhomogeneity in the spinal cord

In terms of susceptibility, the spinal cord can be considered simply as an extension of the brain; to the extent that it suffers from greater ΔB_0 this is due to the susceptibility of its surroundings: in particular, nearby air-tissue interfaces (12) and the surrounding spine (13). Moreover, time-varying field fluctuations arise in certain regions of the cord, for instance, due to sporadic events such as swallowing (14), and due to periodic respiration-related motion (14,15).

1.3.3 Susceptibility-related artifacts

Errors produced by B_0-field variation generally depend on the imaging sequence and the adopted parameters. The following are among the most commonly encountered ΔB_0-induced artifacts (9):

- Signal loss in GRE acquisitions due to intravoxel T_2^* dephasing (as ΔB_0 across the voxel dimensions leads to local dephasing)
- Geometric distortion along the phase-encoding axis in EPI (as ΔB_0 causes the effective encoding-trajectory to deviate from the expected *k*-space coordinates) (16)
- Ghosting and blurring due to phase (i.e. field) inconsistencies between successive excitations (17)
- Chemical shift artifacts due to inefficient fat saturation (18)
- Warped slice profiles and in-plane intensity artifacts in cases where significant resonance offsets are present during excitation and this is not accommodated by the RF Tx pulse (19)

1.4 Common solutions

The following sections provide a brief overview of standard techniques used to combat ΔB_0-induced artifacts. Note, however, that small-scale changes in tissue susceptibility can produce T_2^*-contrast that is, in fact, useful for a number of applications (e.g. in BOLD-fMRI and susceptibility-weighted imaging); hence, fully eliminating these effects is not always desirable.

1.4.1 Reducing echo-times

By reducing the echo-time TE, spins are given less time to dephase, thereby reducing T_2^* effects. To achieve a particular resolution in the frequency-encoding (readout) dimension δ_{RO}, however, a certain amount of dephasing needs to be applied to the spin-distribution (i.e. a certain amount of time τ for a given gradient strength G_{RO}). While τ can be reduced by using a stronger read-out gradient, this can only be done up to a point, beyond which the greater transient field will produce undesirable physiologic effects in conductive tissue (e.g. peripheral nerve stimulation). While techniques such as partial-Fourier can help to further reduce TE, a practical minimum TE nevertheless exists for a given resolution.

1.4.2 Reducing voxel sizes

For T_2^*-weighted sequences, the greater the spread of frequencies within a given voxel, the greater the dephasing and, consequently, the lower the voxel intensity. Hence, by increasing the resolution, intravoxel dephasing is necessarily reduced. However, insofar as the overall signal level depends on the number of contributing spins, reducing voxel dimensions only helps to recover SNR up to a point. For 2D-imaging, the largest gains are typically achieved by reducing the slice-thickness since voxel dimensions tend to be largest along this dimension.

1.4.3 RF refocusing pulses and spin echoes

While gradient-refocusing undoes dephasing caused by the applied gradients, dephasing from any other static field inhomogeneity (T_2') is left uncorrected. The latter can be addressed by applying RF refocusing pulses to the transverse magnetization instead of refocusing gradients. The refocused magnetization is then termed a "spin echo" rather than a "gradient echo". While spin echo sequences predominated for the early years of MR, they are not always appropriate: As the additional RF pulse deposits more heat in tissue every *TR* cycle, and since the effect scales inversely with wavelength, spin echo sequences become less practical at ultra-high field (e.g. $\geq 7\,T$). Moreover, as spin echoes fully refocus static-field dephasing, they cannot produce the useful T_2^* contrast exploited by BOLD fMRI or susceptibility-imaging.

1.4.4 Reduced FOV and parallel imaging

Error generally accumulates while filling the k-space. While traditional acquisitions are generally more forgiving, EPI is prone to distortion due to the extended read-out. One way to mitigate this issue is to cover k-space faster (18), for instance, by skipping every other line along the phase-encoding direction. By violating the Nyquist-Shannon sampling condition, this normally results in aliasing artifacts, but these can be avoided or overcome using various strategies. One approach is to confine the excitation to the imaging region of interest by using 2D selective RF pulses or saturation bands (18), or by using nonlinear encoding gradients (20). The more commonly used approach is parallel imaging (21), where the properties of parallel Rx arrays are used either to estimate the missing k-space lines (as in the GRAPPA technique (22)) or to unfold the aliased images (as in the SENSE technique (23)).

1.4.5 Post-processing methods

Since spatial encoding is based on controlled modulation of the local Larmor frequencies, changes to the latter, when not accounted for, can lead to geometric distortion, i.e. magnetization appearing in the image at $\mathbf{r}'$ is displaced from its true location $\mathbf{r}$ by some distance $\Delta\mathbf{r} = \mathbf{r} - \mathbf{r}'$. Along the frequency-encoding axis, the applied gradients are typically much stronger than ΔB_0 such that distortion along this axis is often insignificant. In EPI, however, distortion along the phase-encoding axis is often considerable. Various correction strategies exist (24), e.g. registration to undistorted images (if available). Alternatively, common *unwarping* techniques begin by mapping the distortion field (the operation leading to $\Delta\mathbf{r}$) and then apply its inverse to the distorted images. This can either involve measuring ΔB_0 itself, or, by acquiring "blip-up" and "blip-down" EPI (i.e. reversing the phase-encoding gradient to produce images distorted in opposite directions).(16)

1.4.6 Shimming

Another approach to the mitigation of ΔB_0-induced artifacts is to fix the problem at its source by minimizing ΔB_0 directly. This is generally known as *shimming* and it is regularly done in conjunction with the acquisition and image processing strategies discussed in the preceding section.

Passive shimming can be achieved using magnetically permeable material (e.g. fixing steel plates strategically around the bore during construction and installation of new MRI scanners). Or, by using material with magnetic susceptibility matched to that of tissue, certain external air-tissue can be effectively removed, e.g. as demonstrated by Lee (12), who used pyrolytic foam to surround the neck.

Active shimming corrects field deviations by optimizing the currents I applied to a set of inductive coils (electromagnets known as *shims*). The central equation is the law of Biot-Savart:

$$\mathbf{B}(\mathbf{r}) = \frac{\mu_0 I}{4\pi} \int \frac{d\mathbf{l} \times (\mathbf{r} - \mathbf{r}')}{|\mathbf{r} - \mathbf{r}'|^3} \qquad [1.9]$$

where μ_0 is the vacuum permeability, $d\mathbf{l}$ denotes the infinitesimal wire segment located at $\mathbf{r}'$ and the integration takes place over the full current path.

Implicit to Biot-Savart [1.9] and the dipole-convolution of [1.8] is the *principle of superposition* for static magnetic fields (i.e. each current element $Id\mathbf{l}$ contributes a small change $d\mathbf{B}$ to the total field). For a set of n discrete field-sources, their individual fields simply sum to produce the total field: $\mathbf{B} = \mathbf{B_1} + \mathbf{B_2} + \ldots + \mathbf{B_n}$. Thus, the problem of shimming is generally a matter of finding the optimal currents to apply to a set of coils to produce a total longitudinal shim field $\sum_1^n B_{nz}$ that best minimizes the longitudinal field variation ΔB_0 over a specific region of interest.

Conventional shims (which will be reviewed in section 2.1) are designed to produce fields that correspond to the terms of a spherical harmonic expansion. As each term requires a dedicated coil, space constraints and other practical limitations typically limit the available terms on most commercial whole-body scanners to lower orders (e.g. the 1st and 2nd order terms illustrated in Figure 1.7), with the 0th order term (a global B_0 offset) substituted by adjustments to the Tx carrier frequency. These shims were originally introduced to MRI to produce global corrections spanning the entire imaging volume of the empty scanner (i.e. to correct ΔB_0 owing to external sources such as manufacturing imperfections). As such, the correction afforded by conventional shim coils may be described as *generic* and *nonlocal*, notwithstanding the current adjustments typically made once a subject has been positioned in the bore (thereby altering ΔB_0) and once the imaging region has been selected.

Evidently, to inform proper adjustment of the shims, ΔB_0 must first be measured. A description follows in the next section.

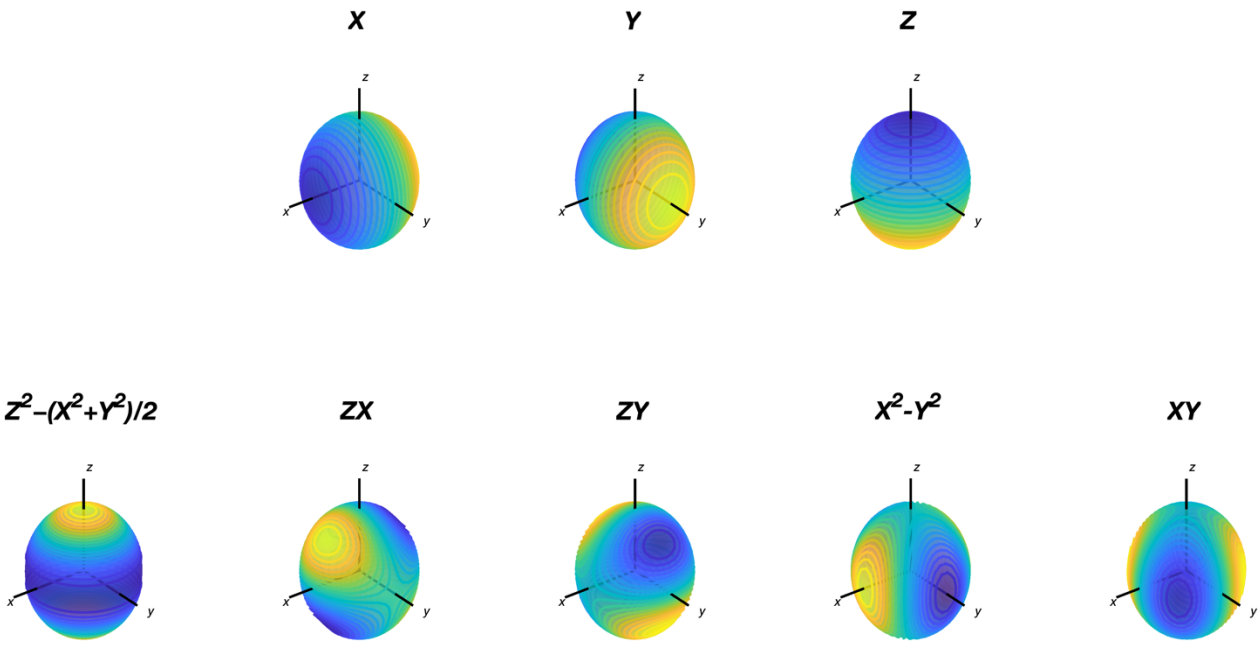

Figure 1.7: Normalized ΔB_0 profiles of the spherical harmonic field terms commonly used in clinical scanners. Offsetting the imaging gradients with a constant current generates the 1st order terms (top row); 2nd order terms (bottom row) are each generated by dedicated shim coils positioned outside the gradient shield. Isocontours are drawn around the spherical surfaces to help visualize the 3D field geometry (i.e. these are not wire patterns).

1.4.7 Field mapping

Some form of rapid ΔB_0 measurement generally precedes image acquisition to guide the shim update. While various MRI techniques will work to provide information on ΔB_0, GRE phase imaging is perhaps the most common as it permits spatially resolved B_0 *field maps* which can be made relatively robust to artifact.

As the magnetization is itself real rather than complex valued, the inverse fast-Fourier transform of the acquired data would, under ideal circumstances, yield a real image. In practice, the presence of ΔB_0, Tx variation in B_1^+, Rx sensitivity variation B_1^-, Rx noise, and other factors lead to a non-negligible phase component φ. Therefore, standard images are formed by taking the absolute value of the reconstruction (i.e. the magnitude) and the phase is generally discarded. However, by saving the phase images (typically an option available on the MRI console) it

becomes possible to produce a field map. The example provided in Figure 1.8 serves to illustrate the process reviewed below.

For an arbitrary voxel, the phase will generally possess a constant offset φ_0 owing to B_1 factors, as well as random noise ε:

$$\varphi(\Delta B_{0,} TE) = \varphi_0 + \gamma \Delta B_0 TE + \varepsilon \qquad [1.10]$$

In practice, each individual channel of an Rx array will possess a specific phase offset. Throughout this work we will assume the individual images have already been combined, however, it is worth noting that this can present a challenge, particularly at fields above 3 T as RF wavelengths shorten (for details on solutions, see Robinson et al. (25–27)).

One can eliminate φ_0 to solve for ΔB_0 (albeit, retaining a contribution from noise) by measuring the phase at different echo times. These may be acquired either using a multi-echo GRE sequence (e.g. Figure 1.5) or by using at least two distinct *TE* in a pair of otherwise identical single-echo acquisitions. The former has the advantages of being faster and of avoiding possible changes to the variables between measurements while the latter has the advantages of greater flexibility in the choices of *TE* (e.g. lower bandwidth read-outs can be used for higher SNR, ΔTE can be made arbitrarily small, and potential gradient refocusing errors encountered with multi-echo GRE are avoided).

Since a measured phase angle of φ is indistinguishable from $\varphi \pm n2\pi$ (for $n \in \mathbb{Z}$), the measurements are only defined between $[-\pi, \pi)$ and ambiguities called phase wraps occur whenever the phase accumulated at TE exceeds this range. These often manifest as false spatial discontinuities in the phase images which need to be resolved by passing the images to a dedicated unwrapping program, e.g. (28–30). As phase accumulates with *TE* and as phase unwrapping tends to be more reliable when wraps are not overly dense, it is often better to calculate the phase differences between *TE*s using complex division (as illustrated in Figure 1.8) and to unwrap these differences images rather than attempt to unwrap the original phase images themselves. This way, φ_0 is immediately eliminated (along with its contribution to wrapping) and wrap-density will scale with ΔTE rather than TE (which is typically much longer). From the unwrapped phase-difference images, ΔB_0 can be calculated by rescaling according to the above Eq. [1.10]; however, since the actual field variation is typically very small (~μT), field maps are

conventionally scaled and quoted either in *ppm* (i.e. as $\Delta B_0/B_0$) or in Hz (i.e. as $\gamma \Delta B_0$) depending on the context.

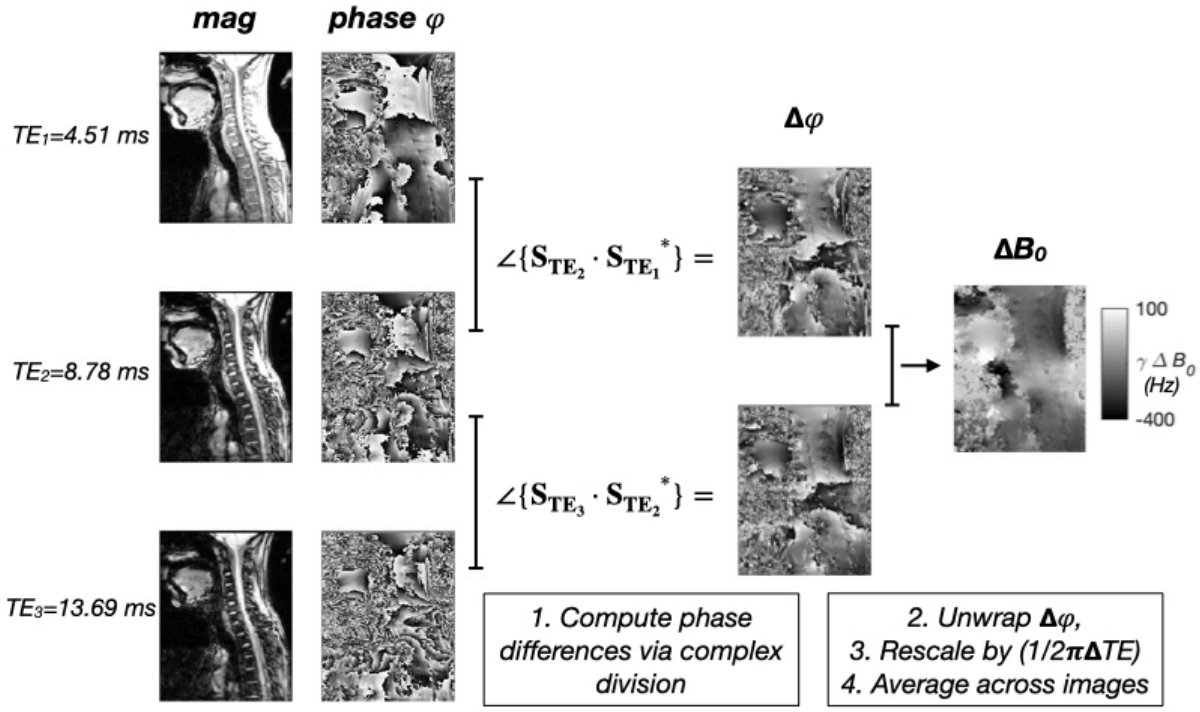

Figure 1.8: Processing pipeline to produce a ΔB_0 field map from multi-echo GRE phase images. $\mathbf{S_{TE}}$ denotes the complex image formed by the magnitude and phase at the given *TE* and $\mathbf{S_{TE}}^*$ denotes the complex conjugate. As phase accumulates with *TE* and as phase unwrapping tends to be more reliable when wraps are not overly dense, it is often better to calculate the phase differences between *TE*s using complex division and to unwrap these differences images rather than attempt to unwrap the phase images themselves.

1.5 Project aims and hypotheses

Using local arrays of active shim coils, customized for the spinal cord, our aim will be to minimize static magnetic field variation—the deviations from B_0 which are introduced the moment a subject enters the scanner and which, in general, vary over the course of the scan (e.g. due to physiologic motion).

1.6 Hypotheses

In any MRI facility where human subjects are regularly scanned, one typically finds a range of anatomy-specific RF coils. Oddly, this standard customization has yet to extend to B_0 shim coils which have long-remained *one-size-fits-all*: despite the specific problems associated with ΔB_0 in the spinal cord, conventional shimming relies on the same generic set of shims which are positioned far from the anatomical region of interest and which are typically only adjusted once, at the outset of each image acquisition.

As ΔB_0 distortions arise locally in space ($\propto 1/R^3$) and change locally across time, we hypothesize that *shimming* too—in terms of coil placement and in terms of the temporal optimization of currents—should likewise be done *locally*.

CHAPTER 2 LITERATURE REVIEW

2.1 Conventional shimming

The following briefly reviews the technological developments in the early days of NMR that led, relatively quickly, to a de facto consensus regarding the design of shim coils.

2.1.1 Active shimming and NMR spectroscopy

By the early 1950s, several research groups (31–34) had discovered that the apparent resonant frequency of a given spin could change according to its chemical environment—a phenomenon dubbed *chemical shift*. To unambiguously resolve the effect (as distinct peaks in the recorded spectra) it was important that the main magnetic field be highly stable and homogenous. It was in this context that "current shimming"—better known today as *active* shimming—was first introduced by Arnold.(35) Using a set of nine, planar shim coils, Arnold achieved an unprecedented spectral resolution in a sample of pure ethyl alcohol; in so doing, new information relating to hyperfine structure was discovered in the measured spectra.

2.1.2 Free induction decay

To determine the optimal set of shim currents for a given experiment, one first requires a means of assessing the field homogeneity across the sample. To this end, Arnold recommended a pulsed NMR technique that had recently been introduced by Hahn.(36) By recording the T_2^*-weighted signal following a nonselective excitation, the observed transient, known as the *free induction decay* (FID), would serve "as an indicator of field homogeneity. In general, the longer the transient signals persist, the more homogeneous the field in the region of the sample."(35) As each measurement took only a few seconds, an operator could quickly gauge the impact of an adjustment to the shims by comparing against the measured tails of successive FID measurements. In principle, the operator might eventually settle on the optimal configuration; in practice, however, it was later noted (37) that finding the best-possible currents for Arnold's original array design could be challenging. Simply stated, field patterns of the various shim coils were insufficiently distinct such that an adjustment to one coil could entail several re-adjustments to the other coils.

2.1.3 Linear gradients ("bucking" coils)

Conveniently, what would become the first set of "orthogonal" shim coils (i.e. coils that largely avoided the above problem) had already been introduced to the NMR experiment. In experiments by the Purcell group (38,39), pairs of planar coils positioned symmetrically about the NMR sample were used in two ways: configured as Helmholtz coils (with equal, parallel currents), these "sweep coils" were used to modulate B_0 uniformly across a sample; alternatively, when configured as "bucking coils" (with equal but opposite currents), the coils produced linear field gradients that were used to study diffusion. The latter configuration was readily repurposed to act as linear shim coils, it remained only to rearrange three of them along the principal axes and to supply them with constant DC to produce steady fields suitable for shimming. The utility of this coil configuration for spectroscopy is illustrated in Figure 2.1 which is adapted from the original patent submitted by Nelson at Varian Associates.(40)

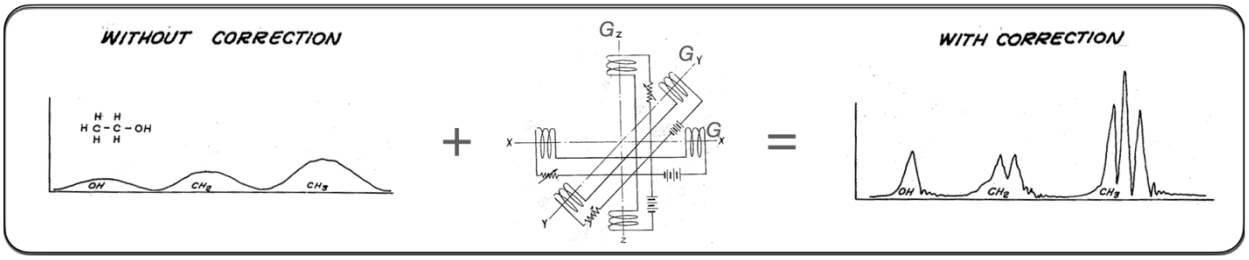

Figure 2.1: Proton NMR spectral resolution vs. field inhomogeneity for ethyl alcohol. In this example, adapted from (40), the broadened/blurred spectral peaks observed without the 1st order shim correction (left) are sharpened after shimming with the orthogonal G_x, G_y and G_z shim coils (centre), thereby revealing new peaks (right).

With independently adjustable linear fields along each of the three Cartesian axes, and given sufficient power, any linear field gradient along an arbitrary dimension over the sample volume could be corrected with the proper combination of currents; moreover, the optimal currents could be determined, one coil at a time, following the simple algorithm proposed by Arnold.

2.1.4 Spherical harmonics

Once it was established that certain coil geometries were more conducive to the FID-based shim optimization, the pertinent question became how the correction could be generalized to cover more complicated (higher-order) forms of field variation. While working in parallel at competing

companies, industry scientists Jaynes and Golay (41–43) arrived at essentially the same conclusion—informed, as it was, by a rather well-known result of classical physics. Namely, in a current-free region of constant magnetic susceptibility, the static magnetic field **B** will always satisfy the Laplace equation ($\nabla^2\mathbf{B} = \mathbf{0}$); a fundamental property of any such *harmonic function* is that it can be completely described by a convergent power series. When Laplace's equation is solved in spherical coordinates, the power series representation naturally assumes the form of an expansion in *spherical harmonics*:

$$B_z(r,\phi,\theta) = \sum_{l=1}^{\infty}\sum_{m=-l}^{l} r^l P_l^m(cos\theta)(A_{lm}cos\phi + B_{lm}sin\phi) \qquad [2.1]$$

Here, the position vector $\boldsymbol{r}$ pointing to Cartesian coordinates (x,y,z) is instead described in standard spherical coordinates as (r,ϕ,θ)—respectively, the radial distance, azimuth, and polar angle. $P_l^m(cos\theta)$ are the associated Legendre polynomials—a family of orthogonal functions. Following (44–46), l will be referred to as the "order" and m as the "degree" (note that an alternate convention is also in use where the two names are swapped, e.g. (47)). A_{lm} and B_{lm} are scalar coefficients determined by the specific value of the field $B_z(r,\phi,\theta)$.

While the series involves an infinite number of terms, in practice, fields can often be adequately approximated using just a few, lower order, terms. The field expansion was convenient insofar as the orthogonality of terms facilitated the FID-based shim optimization. Moreover, the first four terms of the expansion could be produced by coils that were already part of the experimental apparatus. Naturally, researchers sought to design additional shim coils that would be capable of generating higher order/degree spherical harmonic terms.

Both Jaynes (41) and Golay (42) had initially designed coils that wrapped around cubic or spherical formers, however, these early designs made it difficult to access the NMR sample and the probe that needed to be placed inside. With his second prototype, based on planar shim coils, Golay was able to resolve the accessibility issue.(37,42) Later adapted to cylindrical bores, the "Golay saddle-coil" served an early generation of whole-body MRI scanners, both as a transverse gradient-coil and 1st-order shim.(44,48)

In their classic study, Roméo and Hoult (44) described how Golay's designs could be adapted for MRI; likewise treated were spherical harmonic-based designs for passive (high-permeability steel) and active (discrete current arcs) shims. Notably, it was in the specific context of scanner

installation and occasional maintenance that the authors saw their techniques and shim designs being applied. This is attested to by the fact that a significant portion of their study was devoted to "the art" of magnetic field profiling: At the time, this involved using a rig to reposition a small NMR sample at numerous prescribed locations about isocentre in order to measure the local resonance frequency and, hence, the field. For accurate and precise measurements, the process would be time-consuming; moreover, it essentially precluded the possibility of mapping the field with a subject in the scanner.

Thus, spherical harmonic shims of 2nd order and above were originally incorporated into MRI scanners for the purpose of correcting B_0 deviations that were essentially fixed and subject-independent. Subject-based shimming with higher-order terms was more ambitious but it would soon become practical pending advances in coil design (notably, active shielding (49) and low-inductance "fingerprint" coils (50,51)) which, in turn, allowed GRE-sequences to become useful.(8)

2.2 Unconventional shimming

This section will review some shimming strategies that go beyond the traditional, static volume-based approach.

2.2.1 Z-shimming

Due in part to idiosyncrasies of early gradient systems, 2D imaging with non-oblique slices (encoding along the principal anatomical axes) predominated which, for brain imaging, often meant axial acquisitions. As in-plane voxel sizes are commonly smaller than the slice thickness, intravoxel dephasing in any GRE experiment would be predominantly through-slice. As a result, the linear z-shim gained a special importance near large susceptibility interfaces (e.g. above the nasal cavity, sphenoid sinus, and auditory canals). The z-shimming technique (52,53) consists of reacquiring the same slice multiple times, each time employing different slice-refocusing gradients. Insofar as $\Delta B_0/\Delta z$ varies across a slice, so too will the optimal z-shim, such that by reducing through-slice dephasing in one location, the field gradient elsewhere might be inadvertently increased. The resulting magnitude image of a given slice, which is produced through a weighted-combination (e.g. sum-of-squares) of the various measurements, should generally exhibit improved SNR compared to any one measurement; however, insofar as

improvements come at the expense of the longer scan times needed for multiple measurements, the technique has not been widely adopted.

2.2.2 Real-time shimming

The effects of subject head motion began to attract interest alongside the rise to prominence of functional MRI. As the GRE-EPI sequence used by most BOLD-based functional studies is highly susceptible to ΔB_0, even small head rotations could induce field changes, thereby producing image distortion and signal-loss artifacts that varied in form and intensity across the course of a scan. To compensate for head rotations, Ward et al. (54) introduced *real-time shimming* where, using integrated navigator echoes every 20 ms to track head motion, shim current updates to the linear gradients were issued as compensating blips within an EPI sequence. Later, van Gelderen et al. (17) extended real-time shimming by incorporating the 2nd-order shims and linking real-time updates to subject respiration. During respiration, the lungs expand and air flows in, thereby altering the effective susceptibility distribution. Raj (55) had first considered these effects in the brain by using a spherical-lung model—a phantom where the concentration of oxygen was varied between 0-100%. The model was chosen as it has a well-known analytical solution: outside a uniformly magnetized sphere, ΔB_0 assumes a form equivalent to that of a z-aligned dipole positioned at the centre of the sphere; furthermore, using a small susceptibility approximation, $\Delta B_0 \propto [O_2]$. Despite its simplicity, Van der Moortele (56) later confirmed that a spherical-lung model was largely sufficient to explain changes in ΔB_0 and EPI voxel displacements observed in the brain during respiration. As higher-order field variations drop off rapidly away from sources (e.g. the lungs), static fields invariably appear dipolar when considered far enough away (e.g. the brain). Informed by the apparently simple dynamics of respiration-induced ΔB_0 in the brain, van Gelderen et al. (17) subsequently demonstrated that the effects could be partially corrected via real-time shimming. Like Ward, an initial "training" series was first performed whereby EPI-based field maps in the brain were acquired every second during two minutes of normal breathing and shims were independently optimized to each time-point, thus creating a look-up table of currents for each point in the respiratory cycle. Real-time shimming was then applied to a multi-echo GRE scan of the brain at 7T, reducing blurring and ghosting artifacts.

2.2.3 Dynamic (slice-wise) shimming

Dynamic shimming (57,58) is, like z-shimming, a technique for 2D imaging, but rather than reacquiring slices with different slice-refocusing gradients, slice-specific shim currents are determined ahead of time (e.g. via field mapping); the currents are then applied immediately prior to the excitation of each slice and sustained for the duration of its encoding and read-out. The technique works according to the general principle that the smaller the target region (e.g. a thin slice rather than a volume), the less room there is for field variation to manifest and, therefore, the easier it is to shim.

Using spherical harmonic terms up to 2^{nd} order, Finsterbusch et al. (59) demonstrated that static shim corrections targeting the brain and cervical spinal cord simultaneously necessarily came at the expense of one or the other (a default shim optimization on a scanner is likely to favour whichever region is responsible for more signal). For axial acquisitions, dynamic shimming avoids this problem. Given the narrowness of the spinal cord in cross-section, dynamic shimming can be particularly effective for reducing geometric distortion and signal dropout in axial GRE-EPI of the spinal cord.(59–61)

Despite a quarter-century having passed since its initial demonstration (58)**,** dynamic shimming remains something of an exotic technique due, in part, to the fact that it has largely been limited to 0^{th}-1^{st} order corrections, i.e. updating the *Tx* frequency and linear gradients only; shim coils responsible for generating higher-order terms are ordinarily unshielded, and therefore, prone to various forms of coupling for which elaborate correction schemes are required in order to be of any benefit.(62)

The following sections will describe local coil designs which serve to avoid some of the coupling issues associated with high-inductance coils.

2.3 Local "Multi-coil" shim arrays

In a series of studies (63–65) centred around several different shim-array prototypes, Juchem et al. presented a number of substantive challenges to the long-dominant spherical harmonic design philosophy. For instance, using a shim comprised of 64 simple loop-coils arrayed on a cylindrical former, the authors demonstrated that the uniformity of the magnetic field in the mouse brain could be considerably improved relative to 2^{nd}-order spherical harmonics owing to the local nature of the coils and the greater degree of freedom afforded by the increased channel-count.

Later, the same group went on to show that such a coil design could be used, not just for shimming, but for spatial encoding as well: With the high channel-count, even linear gradient fields can be reproduced reasonably well using the so-called "multi-coil" shim and, owing to the reduced inductance of the much smaller coil elements, there is less demand for high-voltage amplifiers, thereby facilitating rapid slewing of the coils. By locating coils closer to tissue, shim efficiency (i.e. field-shift per ampere over the target region) is generally improved. In principle, by using small-diameter coils and positioning them away from conductive structures (the cryostat), induced eddy-currents could be minimized (provided that coupling between elements of the array is low).

Encouraged by the reports of Juchem et al., researchers at Siemens Healthineers (66) successfully demonstrated that a rudimentary local shim coil, when appropriately positioned within an Rx-coil former around the nape of the neck, could greatly improve fat suppression when imaging the cervical spinal cord. This prototype has since been developed into a commercial product available on the Magnetom Vida system.(67)

2.3.1 Integrated "AC/DC" shim arrays

Stockmann et al. (68) and Truong et al. (69) independently demonstrated that one could address a critical limitation of the previous multi-coil designs which relied on separate RF coils for imaging. In prior designs, shim and RF coils competed for space as each performs more efficiently (via Biot-Savart [1.9]) when placed near the target anatomy. To solve the "real-estate" problem, Stockmann and Truong designed hybrid coils that allowed RF and B_0 shim currents to circulate through the same coil elements. In Stockmann et al. (68) this was achieved by retro-fitting a 32-channel Rx array with inductive chokes to bridge the DC shim current into the Rx loops and across the tuning capacitors while blocking induced RF from feeding back to the shim amplifiers. Thus, with the simple circuit modification illustrated in Figure 2.2, standard Rx coils can be transformed into integrated "AC/DC" coils.

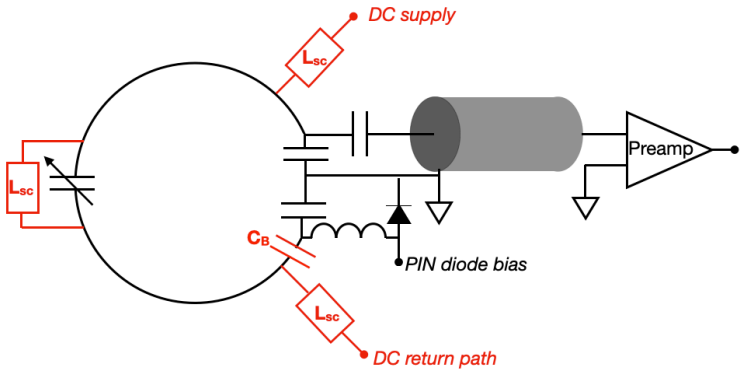

Figure 2.2 Rudimentary circuit diagram for an integrated Rx/ΔB_0 "AC/DC" surface coil. Components in black form the conventional Rx resonant coil with active detuning. Additional components in red enable the loop to function as a local, single-turn shim coil: inductors (L_{SC}) create a DC current path while presenting a high impedance to RF and the blocking capacitor (C_B) prevents DC from reaching the preamp and detuning circuits.

2.4 Summary

The standard approach to shimming in MRI was inherited from the early days of NMR spectroscopy when the optimization of shim currents had to be done manually based on crude measurements of the FID. By using shim coils that generated mutually orthogonal fields (spherical harmonics), an operator could, by trial-and-error, independently optimize the currents passed to each coil while avoiding false optima. But as modern computers and field mapping techniques have supplanted the old approach to shim optimization, the condition that shims produce mutually orthogonal fields is no longer a practical necessity. Moreover, compared with the typical chemical sample to be analyzed by NMR, the human body is highly heterogeneous (e.g. imaging volumes usually encompass various susceptibility interfaces) and, as such, ΔB_0 cannot be eliminated by spherical harmonic terms alone. Dynamic approaches to shim optimization (i.e. slice-wise and real-time shimming) as well as local, non-orthogonal coil designs (e.g. multi-coil and "AC/DC" arrays) offer promising alternatives to conventional shimming.

CHAPTER 3 METHODOLOGY

The general thrust of this project has been toward increasingly *local* shimming of the spinal cord—first, in terms of the spatial position of the shim elements relative to the spinal cord; second, in terms of time, by synchronizing shim corrections to the respiratory cycle. The next three chapters form the body of this work. The following provides a brief account of how this project developed and the connections between the various studies.

The studies are presented here in chronological order, with each building upon the techniques and concepts introduced in those preceding it. Nevertheless, as the work has been reported in a series of individual publications, each chapter can be read independently.

Chapter 4 (Article 1, (70)) introduces a unique 24-channel, local shim array that was custom-built by Resonance Research Inc. (RRI) specifically for the thoracic spinal cord. The study compares the static shim performance of the new design against conventional (1^{st}-2^{nd} order) shimming through a series of experiments and numerical simulations. A unique, custom-built imaging phantom featuring a near-complete section of an excised human vertebral column served as the imaging subject in several of the described experiments.

Chapter 5 (Article 2, (71)) extends the work of the preceding study by reintroducing the problem of in vivo B_0 shimming as one which possesses a natural time-dependence due to patient breathing. The chapter briefly reviews the problems posed to MRI of the spinal cord by respiration and describes the principles behind real-time shimming. The study proposes a simple real-time correction technique based on pairs of field maps acquired during apnea and the correction is demonstrated in a group of healthy volunteers. The specific ability of the 24-channel array to correct for respiration-induced field deviations in the thoracic spinal cord is compared against a simulated basis set of 0^{th}-5^{th} order spherical harmonic fields.

Notably, the ex vivo phantom described in section 4.2.3 was further developed to include a pneumatic system capable of generating respiration-like temporal field variation. The project is described in detail in a dedicated article (72). However, after considerable experimentation with the 24-channel system, the project changed course, leading us to put aside the RRI shim, along with the phantom we had built especially for it.

Chapter 6 discusses the main shortcomings of the technologies and techniques of the two preceding chapters and presents preliminary results with alternative strategies, notably, using two AC/DC arrays. In addition, it proposes a refined technique for real-time shimming.

CHAPTER 4 ARTICLE 1: A 24-CHANNEL SHIM ARRAY FOR THE HUMAN SPINAL CORD: DESIGN, EVALUATION AND APPLICATION

Journal - Magnetic Resonance in Medicine

Ryan Topfer[1], Piotr Starewicz[2], Kai-Ming Lo[2], Karl Metzemaekers[2], Donald Jette[2], Hoby P. Hetherington[3], Nikola Stikov[1,4], Julien Cohen-Adad[1,5]

[1]Institute of Biomedical Engineering, Polytechnique Montreal, Montreal, QC, Canada

[2]Resonance Research Inc., Billerica, MA, United States

[3]Department of Radiology, University of Pittsburgh, Pittsburgh, PA, United States

[4]Montreal Heart Institute, Université de Montréal, Montreal, QC, Canada

[5]Functional Neuroimaging Unit, CRIUGM, Université de Montréal, Montreal, QC, Canada

ABSTRACT

Purpose: A novel multi-channel shim array is introduced to improve magnetic resonance imaging and spectroscopic studies of the human spinal cord.

Methods: 24-channel shim and 8-channel transceiver arrays were designed to insert into the patient bed-table so as to lie in close proximity to the subject's spine. The reference field patterns of each of the shim channels (Hz/A) were determined empirically via gradient echo field mapping and subsequently used to demonstrate shim performance at 3 T using an ex vivo phantom, which incorporated a fixed human spine. The shim was further demonstrated on 5 healthy volunteers.

Results: Application of the shim to the ex vivo phantom reduced the standard deviation of the field over the spinal volume of interest (123.4 cm^3) from an original 51.3 Hz down to 32.5 Hz, amounting to an improvement in field homogeneity of 36.6 %. In vivo, the spine shim resulted in an average improvement in field homogeneity of 63.8 ± 15.4 %.

Conclusion: The localized spine shim offers a promising new means of correcting magnetic field distortion in the spinal cord.

4.1 Introduction

Pathologies of the spinal cord, such as those due to trauma, degenerative processes (e.g. spondylosis) and cancers, are a primary cause for functional disability (e.g. paralysis) and chronic pain. Though MRI already plays a role in the evaluation of spinal cord pathology, it continues to be hampered by image artifacts owing to magnetic field inhomogeneity, underscored in a recent review as "the greatest challenge for acquiring MR images in the spinal cord." (5)

Correcting for subject-specific field inhomogeneity is typically performed at the outset of every scan by passing currents through a set of conducting coils – a process known as "shimming". Conventionally, each shim coil is designed such that, when driven by an applied current, the longitudinal (z) component of the resulting magnetic field uniquely conforms to a spherical harmonic within a predefined volume around the isocentre.(44) Any given field distortion is then decomposed into spherical harmonics, with the shim currents ideally set to cancel as many terms in the series as there are coils. However, in practice, shim amplifiers are of finite power, the efficiency of the generated field (achievable μT/A) decreases with increasing degree of the spherical harmonic, and steep field gradients, such as those observed near air-tissue interfaces, cannot be fully corrected simply by using lower-order spherical harmonic coils.(73)

Recently, these limitations have inspired a departure from the spherical harmonic paradigm: new non-orthogonal multi-coil shim arrays have been proposed as a promising alternative to spherical harmonic coils.(64,68,74) In particular, foregoing the requirement of strict orthogonality affords greater flexibility in terms of coil geometry and array layout: for example, enabling the design of shims that locate the coils in closer proximity to the specific tissues targeted in imaging, thereby retaining a portion of the high spatial-frequency components of the shim fields which tend to decay with distance from the coils.(66) Such designs have lent themselves to better counteracting the steep field gradients due to the frontal sinuses and ear canals – air-tissue interfaces responsible for image artifacts routinely observed around the frontal and temporal lobes.(68,75–77)

Near the spinal cord, however, is the body's most extensive internal air-tissue interface: the lungs, with its associated field distortion varying in time along with respiration. A number of additional local susceptibility inclusions such as vertebral bones, soft tissues, and the oxygen of

the nearby airways further conspire to make imaging of the spinal cord particularly artifact-prone.(11,15) Commonly performed using a set of shims based on spherical harmonics up to 2nd-order, conventional static shimming cannot adequately counteract the complex field distortions observed in the spinal cord, even at clinical field strength (1.5 to 3 T).(15,59,60)

This work introduces a novel 24-channel shim array specifically designed to address this challenge by positioning the non-orthogonal shim coils within the patient bed-table, in close proximity to the subject's spinal cord. The hardware is described and its performance assessed at 3 T through a realistic ex vivo phantom experiment as well as in vivo.(78,79)

4.2 Methods

4.2.1 Hardware

The shim array consists of 24 independently driven, rectangular-planar electrical coils (147×106 mm^2). Coil elements (each 0.8 mm thick) were fabricated using a double-sided flex circuit and each coil features ten turns of a 7 mm wide copper trace. The coils are laterally offset from each other for increased degrees of freedom. The coils are stacked over 7 layers (total thickness about 6 mm) and cooling layers run above and below the upper and lower layers of coils. The shims are potted in epoxy and the total dimensions of the array are 57.5×25.6×1.3 cm^3.

Atop the shim structure is a custom-built transceiver phased array consisting of eight (80×90 mm^2) flat, rectangular surface coils arranged in 2 columns along the axis of the spine for a total coverage of 19×35 cm^2. To avoid interaction with the shim, as well as to avoid the need to tune and match the array inside the scanner, the RF array was shielded by a sheet of double-sided flex circuit (a 18 μm thick solid copper layer on each side) placed 3 cm away from the loops. A potential drawback to the shield is a loss of transmit and receive performance. Therefore, to assess RF performance in the presence of the shield, the unloaded and loaded quality factors Q_U and Q_L were measured, respectively, with and without a body phantom (conductivity=0.6 S/m, permittivity=55) placed roughly 1.5 cm above the loops. As the ratio Q_U/Q_L was found to be 3.6 (=270/75) – above the commonly accepted threshold for 3 T of Q_U/Q_L=3 (80) – the presence of the shield apparently did not overly compromise RF performance and was therefore considered acceptable.

Adjacent RF coils were decoupled inductively using transformer decoupling to a level of -18 dB or better. Eight home-built T/R switches (1 kW, -40 dB isolation) with built-in preamplifiers (WanTcom, MN, USA) connect the coils to preamplifiers during reception and to the RF power amplifier during transmission. A home-built 8-way high power splitter was incorporated to supply RF power to all 8 channels during transmission. The entire system – shim and RF arrays (Figure 4.1), with cover and thin cushion atop them – inserts into the MRI patient-table so as to lie in close proximity to the subject's spine.

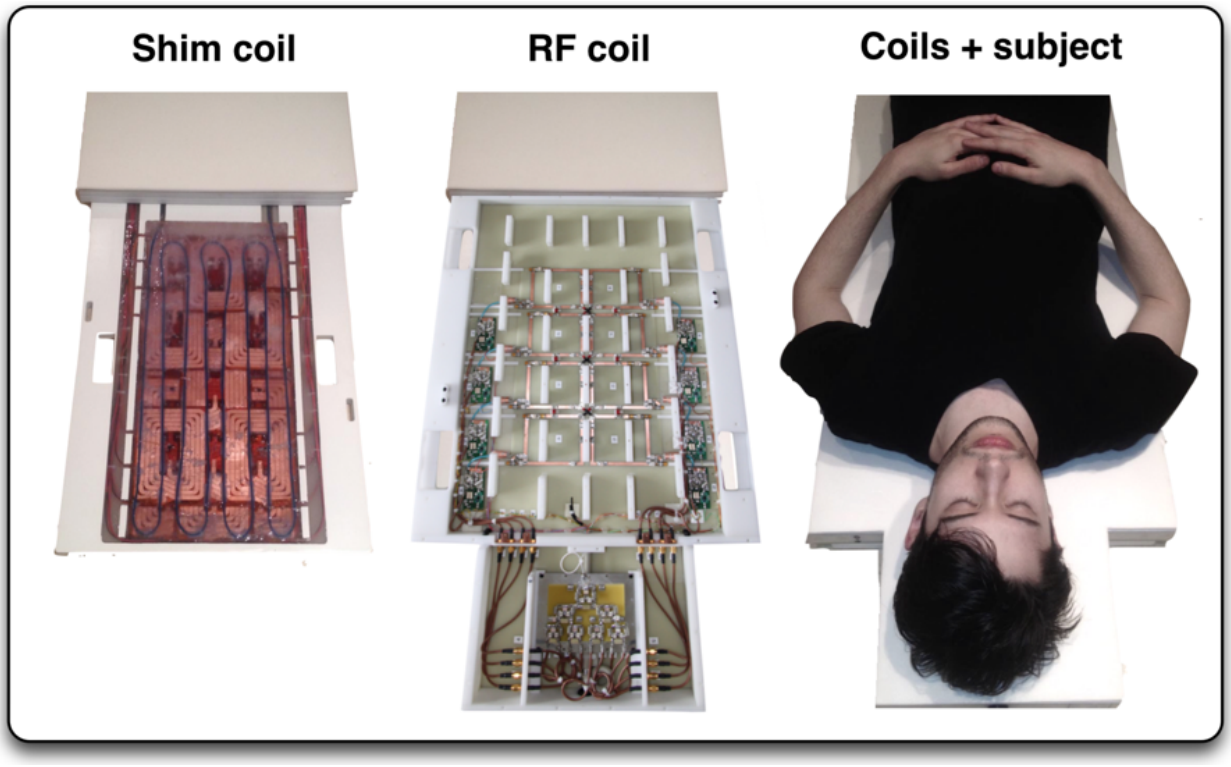

Figure 4.1: Shim and RF transceiver coils. The 24-channel shim coil (left), with 8-channel transceiver atop it (centre), inserts into the patient bed-table, in close proximity to the subject's spine.

Positioned away from the scanner, in the equipment room, is the multi-channel shim power supply (MXD-32 series, Resonance Research Inc., Billerica, MA). The 24 channels, each with its own 16-bit DAC and each capable of outputting +/- 5 A of current, are divided across 4 amplifier banks – themselves limited to +/- 10 A summed across their channels (i.e. combined positive and negative), with a maximum absolute output of 20 A. Also housed in the equipment room, a

chiller (ThermoFlex2500 series, Thermo Fisher Scientific, Asheville, NC) circulates water through the cooling layers.

The system is designed to the specifications of the 3 T Magnetom Tim Trio scanner (Siemens Healthcare, Erlangen, Germany). All experiments took place at the Functional Neuroimaging Unit (CRIUGM, Université de Montréal, Montreal, QC, Canada). Shim control and data processing were performed from the control room, on a MacBook Pro portable computer (Apple Inc., Cupertino, CA) equipped with 8 GB RAM and a 2.5 GHz Intel Core i5 processor (Intel, Santa Clara, CA). The system overview is illustrated in Figure 4.2.

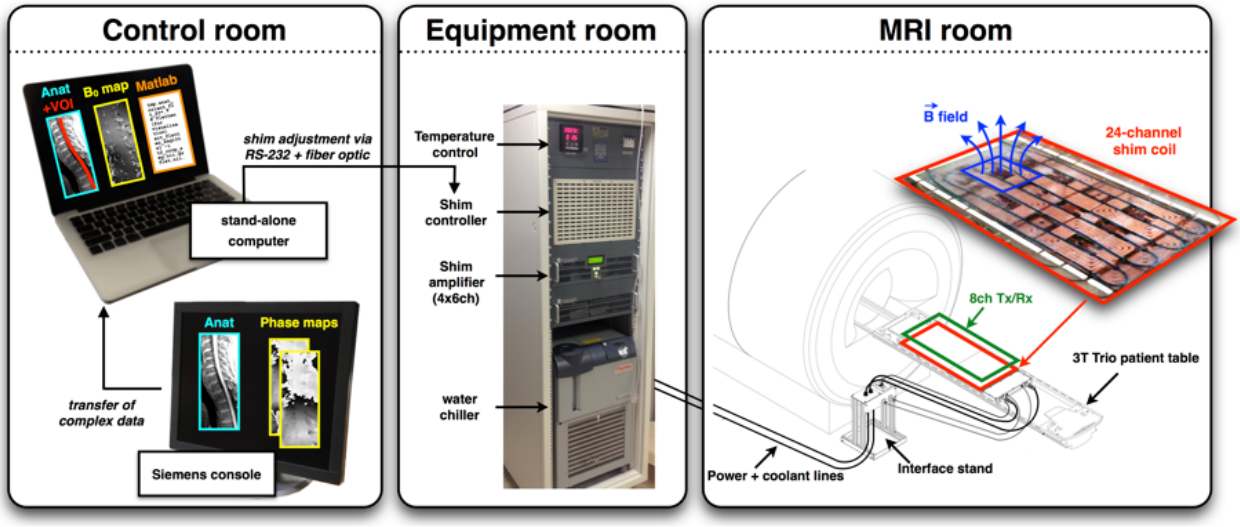

Figure 4.2: System overview. Data are processed on a stand-alone computer, with optimized shim currents then passed to the shim controller housed in the equipment room. Shims are powered independently of the scanner by a dedicated amplifier (MXD-32, Resonance Research Inc., Billerica, MA, USA.)

4.2.2 Shim calibration

Reference maps of the longitudinal fields produced by each shim coil per unit current were determined empirically via gradient echo (GRE) field mapping and are shown in Figure 4.3.(78,81) Using a plastic container nearly filled with water as a phantom (rectangular dimensions: 34×16×44 cm^3), GRE scans were performed with the following parameters: TE=[4.92, 7.38] ms, TR=300 ms; flip angle 56°; spatial resolution=6.81×6.81 mm^2 in-plane, with

26 coronal slices of thickness 5.0 mm, and 5.5 mm between slices, for an effective FOV=354×143×490 mm^3. The phantom was scanned in 2 states per shim channel: once with the coil current set to 0.5 A, and again with the direction of the applied current flipped to –0.5 A. Currents were zeroed in the remaining 23 channels. In addition, a scan was performed with all channels set to 0 A, giving a total of 49 independent scans.

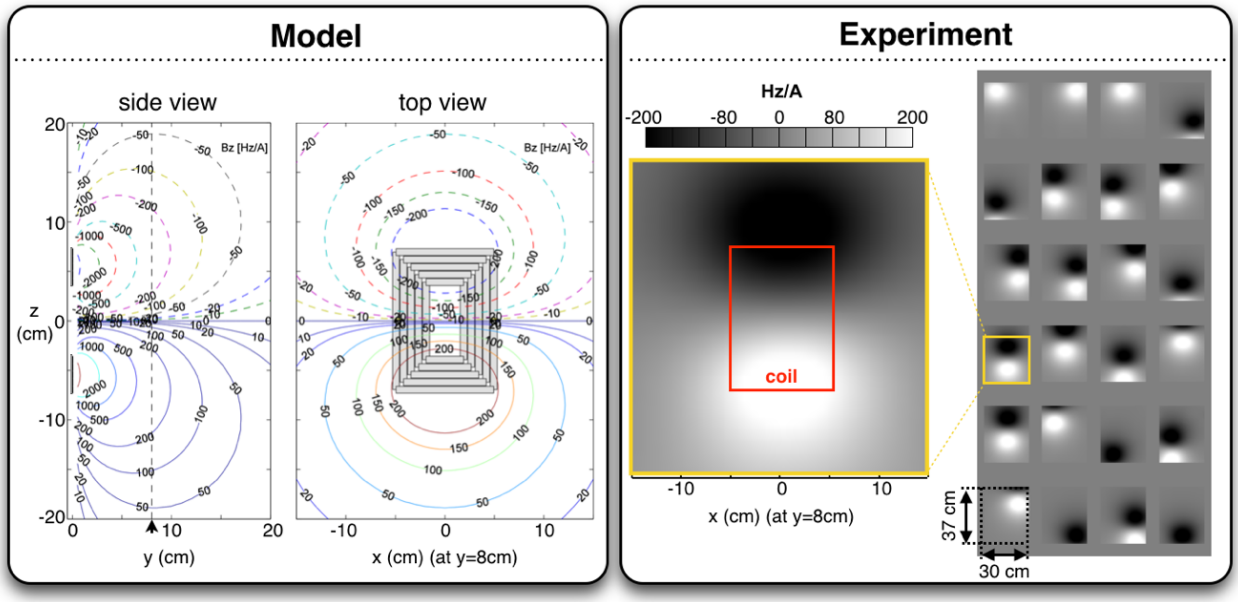

Figure 4.3: Shim reference maps. The left panel (Model) exhibits contour plots of the simulated longitudinal field shift Bz produced by a single shim coil (units of Hz/A). The sagittal cross-section (yz) is centred at x = 0 cm and the dashed line (arrows at y = 8 cm) indicates the position the adjacent coronal cross-section (xz) which features a top view of the coil (grey rectangles). The right panel (Experiment) exhibits coronal slices of the empirically determined shim reference maps for each of the 24 channels. The depicted slice is 4 cm above the surface of the patient bed-table (about 8 cm from the shim coils themselves). The zoomed inset is scaled to the coronal contour plot. The red box over the zoomed coronal inset indicates the approximate location of the underlying coil.

To obtain field maps, phase images for each echo were unwrapped (30) on a slice-by-slice basis using a rectangular mask (30.0×12.1×36.8 cm^3) in order to avoid incorporating regions with poor

signal. Differences between the unwrapped phase images of the two echoes were divided by the echo time difference and scaled to Hz to obtain 49 field maps. To further reduce the effects of noise and distortion, field maps were linearly interpolated along z to yield an isotropic voxel spacing and then low-pass filtered using a normalized spherical kernel (radius = 2 voxels), thereby extracting the smooth harmonic field owing to background susceptibility sources and to the shim itself.(82,83) Least-squares regressions of current to field were performed for each of the 24 channels using the 2 active and 1 inactive filtered field maps, thereby producing the final shim reference maps (Figure 4.3).

4.2.3 Ex vivo shimming

To examine the capacity of the shim to correct field distortions in the spinal cord in the absence of potentially confounding factors such as respiration, CSF pulsation and patient motion, a model was constructed using an ex vivo human spine. The phantom consists of a custom-made polycarbonate box (rectangular dimensions: 38×24×45 cm^3) in which the formalin-fixed spine, which is nearly complete in length (spanning the largest dimension of the box), is placed – secured at each end by means of a plastic clamp glued to the base of the box. The box is filled with a preservation fluid consisting of 73.5% water, 24.5% glycerol, and 2.0% phenol. To add a susceptibility source crudely analogous to the air-tissue interfaces of the lungs, two air-filled 1 L polyethylene bottles were placed roughly 10 cm to the left and right of the spine, and roughly 5 cm anterior to it. Two polycarbonate arches attached to the top of the box prevented the bottles from floating.

Standard 2^{nd}-order shimming was first performed using the Siemens shimming routine. Then, for field mapping, a multi-echo gradient-echo sequence was acquired with parameters: TE=[4.92, 7.38, 11.13, 14.88] ms, TR=200 ms; flip angle 50°; spatial resolution=2.2×2.2 mm^2 in-plane, with 8 sagittal slices of thickness 3.0 mm, for an effective FOV=24×176×282 mm^3. A threshold of 1 percent of the maximum intensity of the corresponding magnitude image was used to create masks for 3d phase unwrapping. (28) Phase differences between the first two echoes were normalized by the echo time difference and scaled to Hz to obtain the field maps.

To restrict the shim optimization to the spinal cord region, high-resolution T2-weighted anatomical images were also acquired and passed to the sct_propseg segmentation tool of the

Spinal Cord Toolbox (84,85), with the segmented volume then dilated by 5 voxels, thereby automatically defining the shim volume of interest (VOI). These anatomical images were obtained with parameters: TE/TR =4.92 ms/30 ms; flip angle 10°; isotropic voxel size 1.3 mm^3; FOV=47×220×220 mm^3. Spinal cord VOIs as well as the shim reference maps were interpolated to the coordinates of the field maps prior to shim optimization. Optimization was rapidly performed using the fmincon function of the MATLAB optimization toolbox (version 2015a, The MathWorks, Natick, MA) minimizing the sum of the shim fields and the measured field map over the VOI while accounting for non-linear amplifier constraints.(68) Optimal shim currents were set and the field map was reacquired.

Furthermore, to examine the effect of the elongated VOI, a virtual "dynamic" shim was simulated post-hoc whereby the shim field was optimized over the axial cross-sections of the VOI on an individual basis (i.e. slicewise).

4.2.4 In vivo shimming

Five healthy subjects (mean age ± standard deviation: 33 ± 11 y) were scanned using the same protocol used in the ex vivo experiment. This was first approved by the Comité mixte d'éthique de la recherche du Regroupement Neuroimagerie/Québec, and informed consent was obtained prior to scanning.

Acquisitions and shim experiments targeted the thoracic portion of the spinal cord. To account for the dynamic effects of respiration on the magnetic field, subjects were asked to inspire and maintain apnea during field map acquisition, about 10 s.

As optimization of the standard (2^{nd} order spherical harmonic) shims was restricted by the scanner console to boxed (rectangular) regions (which were manually adapted to fit as closely to the spinal VOIs as possible), to examine the effect of the shim system apart from the effect of the adopted shim VOI, an additional virtual shim was performed over the specific spinal VOIs using spherical harmonic fields up to 2^{nd} order.(86) It is important to note, however, that these virtual spherical harmonic shim fields were strictly ideal – without spatial imperfections and without constraints on feed current.

4.3 Results

Application of the spine shim to the ex vivo phantom reduced the standard deviation of the field over the spinal VOI (123.4 cm^3) from an original 51.3 Hz down to 32.5 Hz, constituting an improvement in field homogeneity of 36.6 % (Figure 4.4 and Figure 4.5). Notably, the residual field post-spine shim in the VOI possessed a mean of -10.5 Hz rather than the predicted mean of zero, suggesting a possible bias in the shim reference maps. Smaller-scale periodic variations in the field nevertheless persisted subsequent to the application of the spine shim owing to the susceptibility alternation of vertebral disks and vertebral bones. This is most clearly illustrated in Figure 4.5 (c), which plots the median field value of each axial slice within the VOI: application of the spine shim successfully removed the large-amplitude trend observed in the field (linearly increasing toward more superior slices); however, in counteracting the smaller-scale periodic field variations, only the simulated slicewise shim appeared effective (projecting a 44.8% overall improvement in field homogeneity).

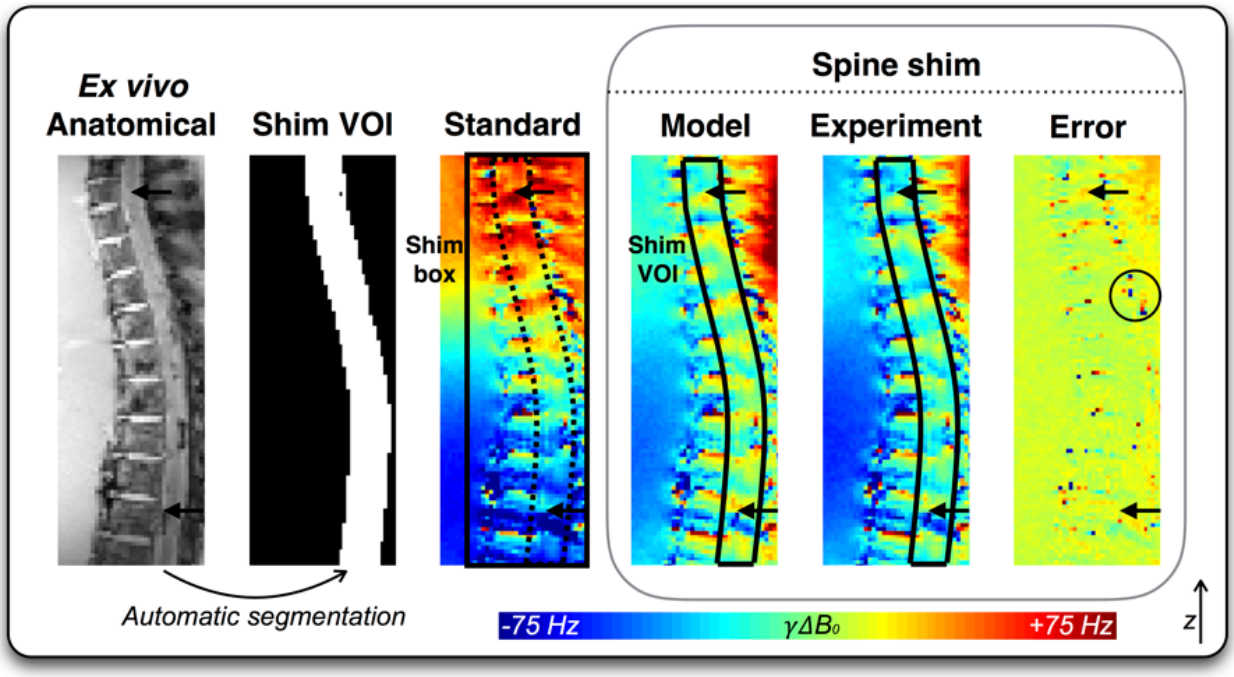

Figure 4.4: Results from ex vivo phantom shim. Using the anatomical magnitude images, the spinal cord was automatically segmented to define the shim VOI targeted in optimizing the spine shim. The four right-most images pertain to the original field map (Standard), the residual field predicted by the spine shim optimization (Model), the re-acquired field (Experiment) obtained after spine shim activation, and the error in the the residual field (Model - Experiment). Notably, the error is not zero as expected but has a median value of 10 Hz over the VOI, suggesting a possible bias present in the shim reference maps. Arrows point to regions around the cervicothoracic junction (top) and inferior lumbar vertebrae (bottom) about which the field homogeneity, although markedly improved upon application of the spine shim, nevertheless show residual inhomogeneity owing to the small-scale field variations of the vertebral bones and, in the latter example, what is likely a deposit of hemosiderin. The black circle in the rightmost column surrounds a cluster of outliers which owe to unreliable field maps (phase) around the vertebrae.

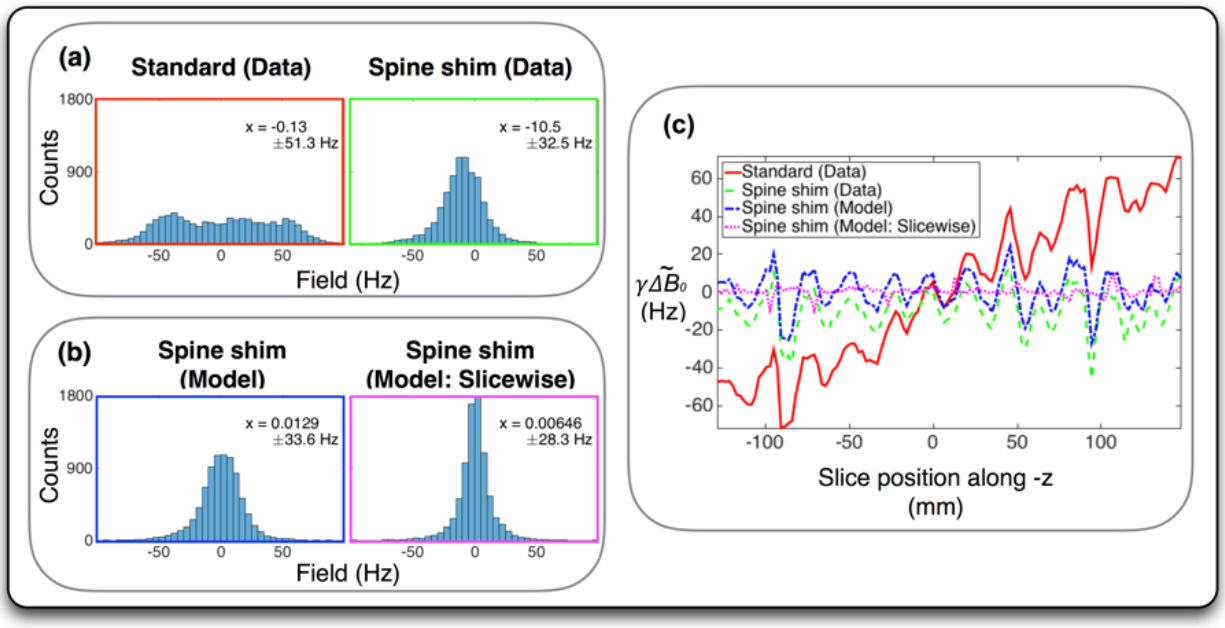

Figure 4.5: Results from ex vivo phantom shim. Left panels (a,b) contain histograms of the frequency distributions across the spinal VOI. Top panel (a): histograms for the measured data, using the standard shims of the scanner (red), and once the spine shim was optimized across the VOI (green). Bottom panel (b): the predicted distributions for the spine shim when optimized for the entire VOI (blue) and when optimization was performed over each of the axial slices of the VOI individually (pink). The line graph in (c) plots the median field value within each axial slice of the VOI for each of the four scenarios. In practice, the spine shim reduced field inhomogeneity by 36.6 % and eliminated the overall linear trend (positively increasing with z) from the field of the standard shim. This result was despite the apparent presence of a bias in the shim reference maps, leading to the mean of the spine shim-optimized field data being offset from zero, as per the model. Only the simulated slicewise-optimized shim appeared capable of addressing the small periodic field variations owing to vertebral bone-to-disk susceptibility alternation.

Figure 4.6 highlights the results from two subjects for which a marked decrease in both field inhomogeneity as well as intensity are observed in the lower thoracic spine. For the five subjects, the spine shim reduced the standard deviations of the field over the spinal shim VOIs (55.9 ± 6.5 cm^3) from 85.8 ± 22.4 Hz to 29.1 ± 9.1 Hz (mean ± standard deviation), representing a statistically significant improvement in field homogeneity of 63.8 ± 15.4 % (significance level

p=0.01). Histograms summarizing these results are shown in Fig. 7. The virtual shim – optimizing the ideal spherical harmonic fields up to 2nd order strictly over the spinal VOIs – reduced the standard deviations of the field to 36.1 ± 13.3 Hz (an improvement of 57.1 ± 12.3 %).

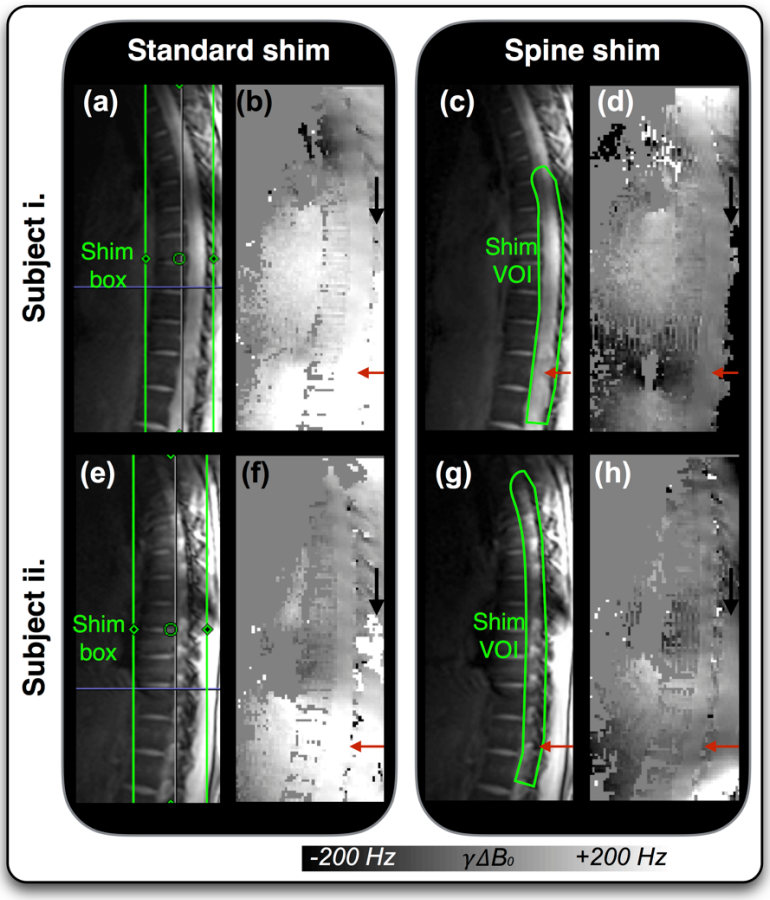

Figure 4.6: Results from in vivo shim of subjects i. and ii. (top and bottom rows, respectively). Standard shimming was performed on the scanner over the green box (a,e), with the corresponding field maps shown in the second column (b,f). Using an anatomical reference scan (not shown) the spinal cord was automatically segmented and dilated by 5 voxels in each dimension to create the Shim VOI (c,g) targeted in optimizing the spine shim. Field maps acquired post-spine shim optimization are shown in the rightmost column (d,h), with red horizontal arrows pointing to the marked improvement in both field intensity and homogeneity in the inferior thoracic cord. Black vertical arrows indicate artificial field discontinuities posterior to the spinal cord brought about by errors in data processing (phase unwrapping).

Processing times for the in vivo and ex vivo data sets, though modest, were dominated by the interpolation of the 24 shim reference maps to the grid spacing of the subject's field maps (2 min, 40 s ± 5 s) and, to a lesser extent, by the spinal cord segmentation (~30 s). Processing times for field mapping (unwrapping) as well as for the nonlinear solver (shim optimization) were each about 1 s.

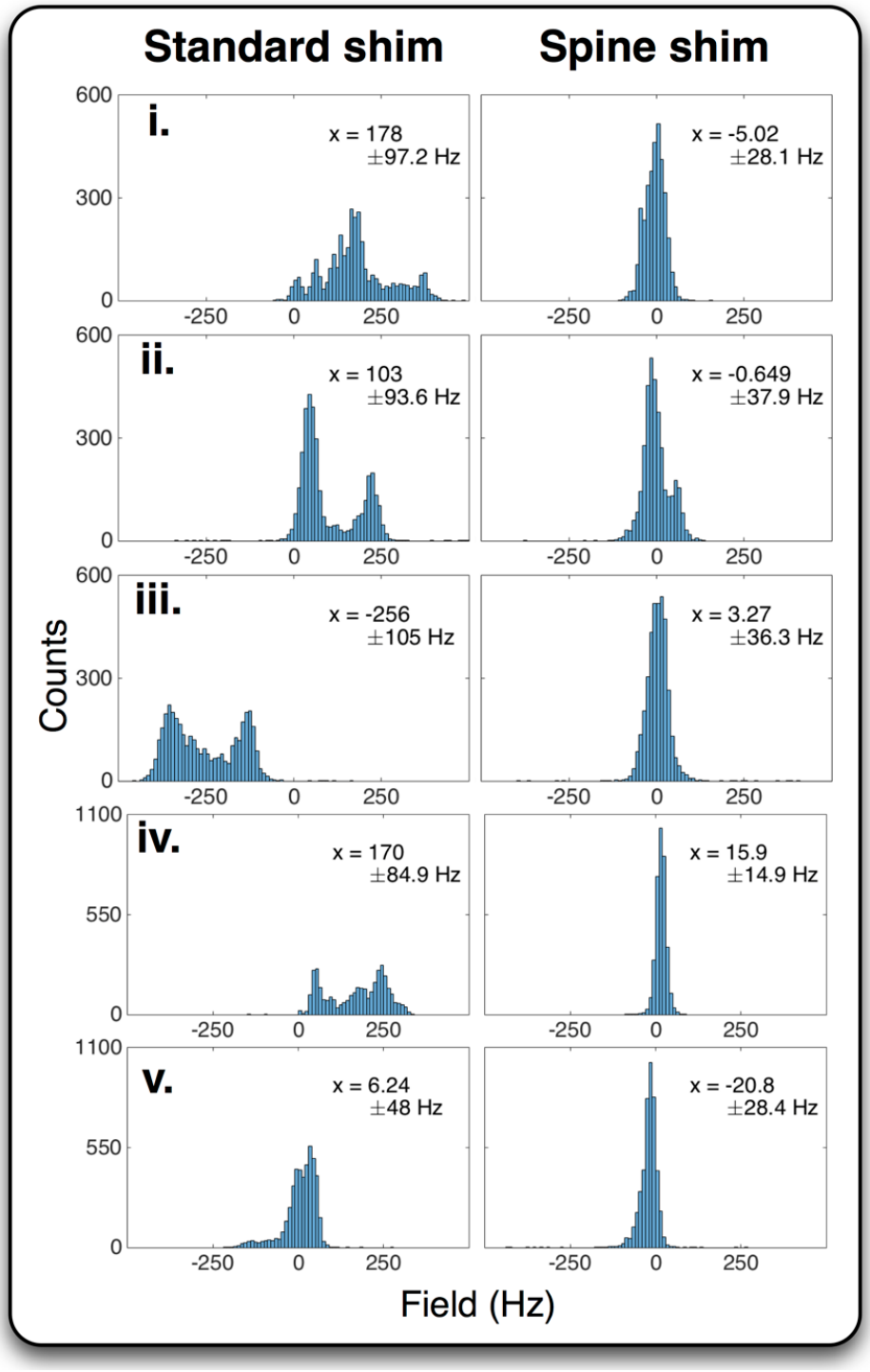

Figure 4.7: Histograms of field data for in vivo subjects i. through v. Application of the 24-channel spine shim reduced the standard deviations of the field over the spinal shim VOIs (55.9 ± 6.5 cm^3) from x = 85.8 ± 22.4 Hz to x = 29.1 ± 9.1 Hz, representing an improvement in field homogeneity of 63.8 ± 15.4 %.

4.4 Discussion

This study introduced a novel 24-channel shim array specially designed for imaging the human spinal cord. Though application of the shim array improved the magnetic field uniformity in each of the examined cases, a careful interpretation of the results requires some qualification as to the ways in which these improvements were relative.

All shim experiments using the 24-channel spine shim began by first correcting the field using the standard shims available on the scanner. Naturally, as the spine shim integrates with the pre-existing system, the two sets of shims were used simultaneously to arrive at the best overall result; no general comparison was made to the effect of which system might generally be most effective or most efficient (such comparisons were made for alternative multi-coil shim designs in (65,68)). Thus, the improvement in field homogeneity achieved by the spine shim in the ex vivo case (36.6 % reduction in the standard deviation of the field across the VOI) was an improvement made relative to the field first optimised using the standard shim.

The situation for the in vivo experiments, however, was somewhat different, owing to the fact that the field could not be kept perfectly static. As the initial optimization of the standard shims did not itself involve a breath hold, the fields of the in vivo subjects would have changed somewhat subsequent to the initial shim, once the subjects were asked to hold their breath for the GRE field map acquisitions. Respiration is known to induce considerable magnetic field fluctuations around much of the spinal cord at 3.0 T: Verma and Cohen-Adad (15) having reported, for instance, an average off-resonant shift of −50 Hz between inspired and expired conditions around the level of T8, with even larger shifts being typical of the inferior cervical spine. This may explain the large displacements from zero of the mean fields over the VOI which were observed for four of the five subjects prior to application of the spine shim (Figure 4.7). Indeed, such displacements were not observed when ideal spherical harmonic fields were used to simulate the shim over the spinal VOI specifically.

Furthermore, this same work (15), as well as a recent work at 7 T (87), which involved breath-hold experiments analogous to the one performed here, demonstrated that the breath-holds performed by subjects in the scanner, and their associated magnetic fields, are not perfectly reproducible. The implication for the current work being that the variable degrees to which the in

vivo spine shim optimizations were successful necessarily depended on the reproducibility of the apneas on which the optimizations were based. This underlines the importance of including several subjects in the experimental protocol. Despite this complication, application of the spine shim resulted in a statistically significant improvement in the homogeneity of the field over the spinal cord at the 1% significance level. Though the improvement from the spine shim was not statistically significant when compared to the virtual shim using ideal spherical harmonics (suggesting that much of the gains in field homogeneity may have owed to the VOI over which the shim optimization took place, rather than the change in shim system) it is important to note that the results of the virtual shim experiments did not depend on the reproducibility of the apneas. Indeed, the purpose of the adopted breath-hold protocol as well as the overall purpose of this work has been as an initial proof-of-concept for the novel shim array, which has been proposed to supplement, rather than supplant, the standard system shims; ultimately, real-time correction of the respiration-induced field fluctuations will be essential.(17,88,89)

The utility of further synchronizing shim updates to the scan itself via slicewise "dynamic" shimming was demonstrated through simulation (Figure 4.5), where relatively small-scale field variations in the spinal cord nevertheless remained subsequent to the volume-optimized static shim. This was to be expected, as the overall shim field, regardless of array design, will never be perfectly capable of modelling the fields of arbitrary susceptibility distributions over arbitrarily large regions of space. The degree to which a shim is successful depends largely on the complexity of the field gradients within the region and the ability of the shim array to reproduce them: by treating the steep 3d gradients as a stack of slices to be shimmed individually, whole regions can be effectively shimmed irrespective of the shims' ability to produce continuous field variation in the direction orthogonal to the slice. This makes dynamic shimming particularly well-suited to correct the static field inhomogeneity in the spinal cord that owes to the susceptibility alternation between vertebral bones and vertebral disks.(60) Alternative array designs that feature a greater number of shim coils (64,74), irregularly shaped elements (90), or that locate the coils even closer to the tissue of interest, e.g. by combining B_1 signal reception and B_0 shim functionalities into individual "AC/DC" coils (68,76), may also be of benefit in addressing the highly localized field distortions around the vertebrae.(86)

Immediate applications for the shim array include MR spectroscopy, T_2*-imaging and EPI-based studies of the spinal cord (e.g. functional and diffusion imaging). For the latter, the implication of the spine shim for reducing geometric distortion can be appreciated by examining Figure 4.6 and recalling that the displacement of a voxel in the phase encode direction in a single-shot EPI acquisition in the absence of parallel imaging (i.e. acceleration factor of 1) is the product of the inter-echo spacing, the local off-resonance shift, and the extent of the FOV in the phase encode direction.(16) Considering the small 3×3×3 voxel regions pointed to by each of the red horizontal arrows, application of the spine shim reduced from the average fields from 286 Hz to -30 Hz (Subject 1), and from 209 Hz down to -26 Hz (Subject 2). Assuming an inter-echo spacing of 0.5 ms, for example, this would imply, for the given FOV, a reduction in the respective absolute voxel displacements from 31.5 mm to 3.3 mm, and from 23.0 mm down to 2.9 mm. Considering the width of the thoracic spinal cord is generally less than a centimetre, such an improvement would be critical.

These specific calculations, however, remain theoretical ideals as the protocol introduced here – optimizing the field over the spinal cord while essentially disregarding the field elsewhere in the excited slice (particularly posterior to the spinal cord, where the shim fields are strongest (Figure 4.3)) – may prove inadequate when it comes to suppressing chemical shift artifact and geometric distortion, for which a larger shim VOI might be necessary. However, for such an approach to work, field data would have to be available across the enlarged VOI. It remains to be determined how this might best be achieved given the attendant difficulties of constructing reliable field maps based on noisy GRE data of finite spatial support. The downward pointing arrows in Figure 4.6 indicate two examples of artificial field discontinuities owing to errors in the phase unwrapping – errors which, far from being isolated or random in nature, tend to occur in blocks, with their positions a function of the underlying field homogeneity. To mitigate this issue, alternative phase unwrapping techniques and/or acquisition strategies may ultimately be required.(91,92)

4.5 Conclusion

This work introduced a novel 24-channel shim array designed to correct magnetic field distortion in the human spinal cord. Foregoing the conventional requirement that the shim fields constitute

an orthogonal basis set allowed the shim coils to be placed within the patient bed-table, in close proximity to the subject's spine. The benefits of this approach were demonstrated by the marked improvements in field homogeneity observed in an ex vivo phantom (36.6 % reduction in the standard deviation of the field), as well as in a series of in vivo experiments, for which a 63.8 ± 15.4 % reduction in the standard deviation of the field was observed over the spinal volumes of interest.

This shim system—which could be combined with respiratory bellows or field probes for real-time adjustments—offers a promising new means of enhancing EPI and spectroscopy of the spinal cord.

4.6 Acknowledgements

We thank Imanne El Maâchi, Iris Leroux, Louis Philippe De Tillieux, Grégoire Germain for their work constructing the ex vivo model, Dr. Hugues Leblond (Université du Québec à Trois-Rivières) for providing the fixed human spine, and Drs. Raphael Paquin (Siemens Healthcare Ltd.), Jason Stockmann (Athinoula A. Martinos Center for Biomedical Imaging) and Allan Martin (University of Toronto) for their helpful advice.

This work was funded by the Canada Research Chair in Quantitative Magnetic Resonance Imaging (JCA), the Canada Foundation for Innovation [32454], the Canadian Institute of Health Research [CIHR FDN-143263], the Fonds de Recherche du Québec - Santé [28826], the Fonds de Recherche du Québec - Nature et Technologies [2015-PR-182754], the Natural Sciences and Engineering Research Council of Canada [435897-2013], the Quebec BioImaging Network, and Polytechnique MEDITIS.

CHAPTER 5 ARTICLE 2: REAL-TIME CORRECTION OF RESPIRATION-INDUCED DISTORTIONS IN THE HUMAN SPINAL CORD USING A 24-CHANNEL SHIM ARRAY

Journal - Magnetic Resonance in Medicine

Ryan Topfer[1], Alexandru Foias[1], Nikola Stikov[1,2], Julien Cohen-Adad[1,3]

[1]NeuroPoly Lab, Institute of Biomedical Engineering, Polytechnique Montreal, Montreal, QC, Canada

[2]Montreal Heart Institute, Université de Montréal, Montreal, QC, Canada

[3]Functional Neuroimaging Unit, CRIUGM, Université de Montréal, Montreal, QC, Canada

ABSTRACT

Purpose: To reduce respiration-induced magnetic field distortions and the attendant image artifacts in echo-planar imaging (EPI) of the human spinal cord.

Methods: Using a custom-designed 24-channel shim array, shim updates were issued in real-time based on a concurrently monitored respiratory trace and a pair of gradient echo field maps acquired during an initial training phase. Proof-of-concept application in gradient echo EPI was conducted in 6 subjects.

Results: Over the thoracic spinal cord, real-time shimming reduced respiration-induced distortions in the EPI by 48.2 ± 12.2 % and increased mean tSNR by 15.7 ± 7.9 %.

Conclusion: Real-time shim adjustment substantially reduces spatiotemporal B0 field variation, opening the door to more robust imaging and spectroscopy experiments in the spinal cord.

5.1 Introduction

The sensitivity of MRI to magnetic susceptibility is both a blessing and a curse: While small-scale changes in the magnetic field permit useful image contrasts, such as the blood-oxygenation-level dependent (BOLD) effect used in functional MRI (fMRI), larger field distortions, particularly those due to air-tissue interfaces, can lead to artifacts such as signal loss in gradient-echo (GRE) imaging and geometric distortion in echo-planar imaging (EPI).

The proximity of the spinal cord to the air-filled lungs makes it particularly susceptible to these field effects, which generally vary in time, along with respiration.(11,15,93) Using GRE field mapping, respiration-induced resonance offsets (RIRO) upwards of 70 Hz at 3 Tesla [T] (15), and 100 Hz at 7T (93), have been reported around the C7 level of the spinal cord during breath-hold acquisitions. Over the same region, 10 mm of artificial displacement of the spinal cord in the anterior-posterior (phase-encode) dimension was observed in a representative example of single-shot EPI due to local change in the resonance offset between inspired and expired respiratory conditions.(15) In comparison, the anteroposterior diameter of the spinal cord around C7 is generally between 7-8 mm.(94) Imaging such a narrow structure requires high-resolution – increasing the length of the EPI readout and, in turn, the sensitivity to RIRO-based distortion, as illustrated in Figure 5.1.(95) As noted previously (96), the need for high resolution motivates a push to ultra-high field strengths (≥ 7T) for the advantages afforded in terms of SNR and susceptibility contrast (e.g. for BOLD-fMRI and susceptibility-weighted imaging); however, these advantages are undermined insofar as the field distortions and their adverse effects on the images, too, scale with the strength of the main field. Given the extent of these artifacts, along with the inherent subtlety of the signal changes associated with BOLD activation (typically on the order of 1%), fMRI of the spinal cord remains technically challenging. As noted recently by Cohen-Adad (97): “respiration-induced change in B0 is one of the main reasons very few people dare to venture into fMRI experiments below the cervical level.”

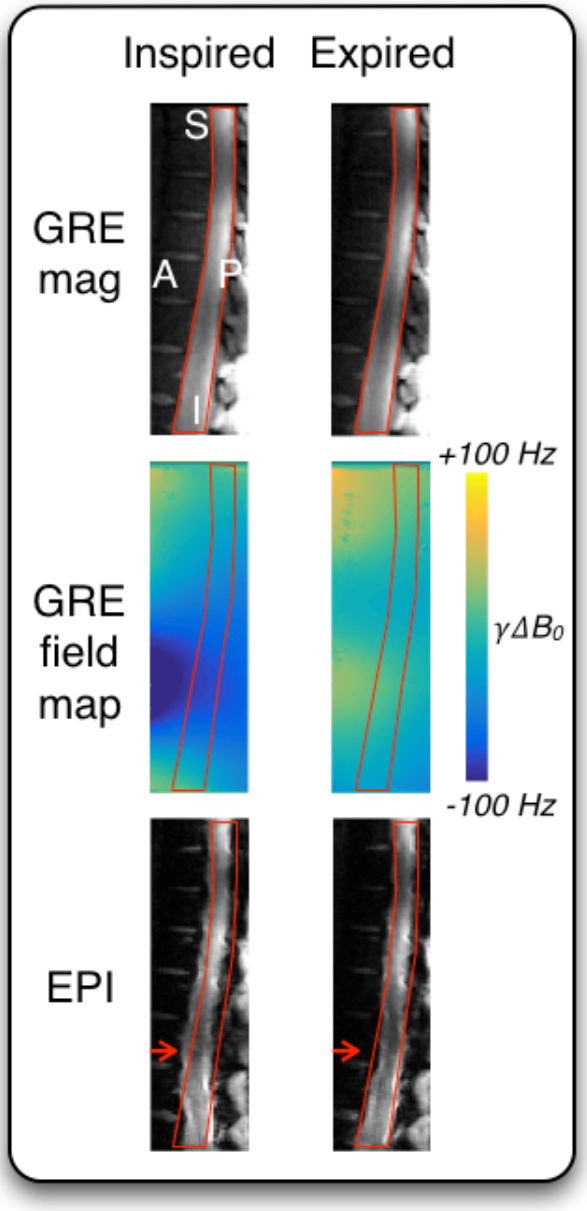

Figure 5.1: Example of respiration-induced distortion in the thoracic spine of one subject between vertebral levels T5-T12. The subject was asked to inspire naturally (left column) and hold their breath for the duration of the GRE field mapping scan (top/middle row: magnitude/field map) and to repeat the breath hold for the EPI (bottom row). The procedure was then repeated in an expired state (right column). The spinal canal was traced on the "inspired" GRE magnitude and superposed onto the other images (red contours). The top row demonstrates that no displacement of the spinal cord occurs between respiratory states on the distortion-free GRE, yet the EPI

exhibits an apparent motion along the phase-encode direction, which is purely artifactual (red arrows).

However, interest in correcting RIRO in the spinal cord extends beyond the enhancement of fMRI for neuroscientific studies and into clinical applications: A recent review (5) identified five advanced MR techniques, including fMRI, that are applied clinically in the brain but remain challenging to implement successfully over the spinal cord largely due to susceptibility effects. Among these techniques, to date, diffusion tensor imaging (DTI) has been the most studied in the context of spinal cord imaging and was thus singled out as the most mature and fit for translation into the clinic (98); and yet, like fMRI, DTI suffers from RIRO-based geometric distortion.(95) Also considered clinically promising was MR spectroscopy (99), which suffers from losses in SNR and spectral resolution in the presence of field inhomogeneities.

Both in the breast (88) and in the brain (100,101), improvements to spectroscopic measures have been demonstrated by modulating shim currents over the course of the scan to counteract the time-varying field distortions; likewise, for T_2^*-weighted imaging of the brain, real-time shimming has been shown to improve signal stability and image quality.(17,102,103) While each of these studies was performed at ultra-high field, conventional static shimming, which employs a low order (0^{th} – 2^{nd}) spherical harmonic basis, remains inadequate for spinal cord applications even at clinical field strengths (1.5 – 3T).(59,60) In a series of recent static experiments, we achieved an average improvement in field homogeneity across the spinal cord of over 60 % by using a custom-designed 24-channel shim array in combination with an automatic spinal cord segmentation.(70) As a sequel to these initial experiments, the following work proposes a simple algebraic framework and imaging protocol by which to approach the problem of real-time multi-coil shimming for correction of RIRO. Using the 24-channel shim array, real-time shimming is shown to reduce the geometric distortion and improve the temporal SNR (tSNR) of a GRE-EPI time series.

5.2 Theory

For a comprehensive overview of multi-coil shimming the reader is referred elsewhere.(65,104,105) From Biot-Savart, the longitudinal magnetic induction field at position $\boldsymbol{r}$ due to a single shim coil can be expressed as the product of the coil current i_s with a geometry term $a_s(\boldsymbol{r})$. For a network of N_s coils, the total longitudinal field within the scanner can be understood as the superposition of the shim fields with the spatially uniform applied field b_0 and the field perturbation $b_\chi(\boldsymbol{r})$ owing to susceptibility:

$$b_z(\boldsymbol{r}) = b_0 + b_\chi(\boldsymbol{r}) + \sum_{s=1}^{N_s} i_s a_s(\boldsymbol{r}) \qquad [5.1]$$

In vector form, for an acquisition consisting of N_{img} voxels, the ideal shim currents should therefore satisfy $\boldsymbol{A i_s} = -\boldsymbol{b_\chi}$, where $\boldsymbol{i_s}$ is the $[N_s \times 1]$ column vector of coil currents and $\boldsymbol{A}$ is the $[N_{img} \times N_s]$ matrix operator formed by placing the set of coil geometry terms along its columns.

In addition to the field perturbation from static sources (e.g., in the context of imaging the spinal cord, sources such as the vertebral bones and the residual air of the lungs) the field will generally evolve in time due to factors such as eddy currents, gradient heating, cardiac pulsation, patient motion, and respiration. This paper focuses on the latter—compensation of the time-varying field arising from patient respiration: $\boldsymbol{b_\chi} \rightarrow \boldsymbol{b_{\chi|t}}$. To correct for this field variation, some notion of how it develops in space and time is needed. In this regard, our point of departure is the work of van Gelderen et al. (17), in which real-time shimming was demonstrated in the brain at 7T, and which suggested a possible linear relation between the time-varying magnetic field $\boldsymbol{b_{\chi|t}}$ and the respiratory cycle as tracked by a scalar pressure reading p_t from respiratory bellows strapped to the subject's abdomen:

$$\boldsymbol{b_{\chi|t}} = \boldsymbol{c_\chi} p_t + \boldsymbol{b_{\chi|o}} \qquad [5.2]$$

It follows that the coupling coefficients $\boldsymbol{c_\chi}$ and the static field offset $\boldsymbol{b_{\chi|o}}$ might be estimated by GRE field maps acquired in as few as two distinct respiratory/field states—a sort of training procedure by which all future field perturbations can be inferred based on the associated pressure reading.

5.3 Methods

5.3.1 Hardware

Figure 5.2 exhibits the system overview for real-time shimming. The 24-channel shim array and 8-channel transceiver are inserted into the patient bed-table, close to the subject's spine. These arrays were recently described in a separate work (70), and the shim coil wire patterns in the PUMCIN format (106) have been made publicly available for download: https://osf.io/4pe6r/. To track patient respiration in real-time, an air-filled latex bladder (i.e. respiratory bellows) was strapped to the subject's abdomen and linked by a 15 m section of vinyl tubing to a pressure-sensing transducer (part number: SSCSLNN100MGAA3; Honeywell, Morris Plains, NJ) connected to a microcontroller (Arduino Uno model, Arduino LLC, Somerville, MA). The microcontroller feeds pressure measurements, sampled every 10 ms, into a stand-alone computer running MATLAB (version 2015a, The MathWorks, Natick, MA), which computes the associated shim currents and passes them to the shim driver every 250 ms. All experiments were performed on a 3 T scanner (Magnetom Prisma Fit, Siemens Healthcare, Erlangen, Germany).

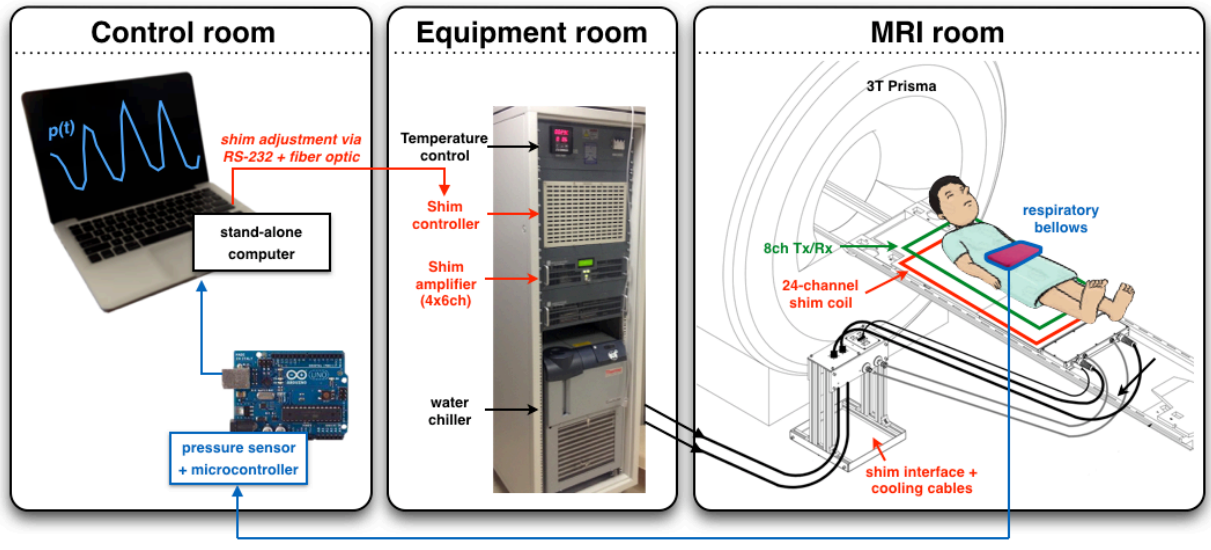

Figure 5.2: System overview, adapted from (70). To track patient respiration in real-time, a thin section of vinyl tubing connects the respiratory bellows strapped to the subject's abdomen to a pressure-sensing transducer and microcontroller. The microcontroller feeds pressure measurements into a stand-alone computer, which then issues the associated shim currents to the shim controller.

5.3.2 Real-time shim training

The following assumes the availability of a distinct pair of field maps ($\boldsymbol{b_{\chi|in}}, \boldsymbol{b_{\chi|ex}}$) and pressure readings (p_{in}, p_{ex}), corresponding to inspired and expired respiratory states, by which the real-time shim protocol can be calibrated. In vector form, Eq. [5.2] inspires

$$\boldsymbol{b_{\chi|in}} = \boldsymbol{c_\chi} p_{in} + \boldsymbol{b_{\chi|o}} \quad [5.3]$$

$$\boldsymbol{b_{\chi|ex}} = \boldsymbol{c_\chi} p_{ex} + \boldsymbol{b_{\chi|o}} \quad [5.4]$$

by which expressions for the static field offset and coupling coefficients can be readily obtained. However, the immediate aim is not to track the field evolution itself (though this may be useful for retrospective corrections (107,108)) but rather to negate it by updating the shims. Accordingly, a general expression is defined in the form of Eq. [5.2] for the time-varying shim field, where $\boldsymbol{b_{s|o}}$ is the static shim field offset for $p_t = 0$ and $\boldsymbol{c_s}$ is the vector of pressure-to-shim field coupling coefficients:

$$\boldsymbol{b_{s|t}} = \boldsymbol{c_s} p_t + \boldsymbol{b_{s|o}} \quad [5.5]$$

Ideally, the static and time-varying components of the shim field would be equal and opposite to those of the magnetic field distortion (i.e. $\boldsymbol{b_{s|o}} \rightarrow -\boldsymbol{b_{\chi|o}}$; $\boldsymbol{c_s} \rightarrow -\boldsymbol{c_\chi}$); however, due to hardware limitations this ideal is not generally attainable and amplifier constraints must be considered in the optimal shim. Defining the optimal shim fields for the inspired and expired conditions as $\boldsymbol{b_{s|in}}$ and $\boldsymbol{b_{s|ex}}$, the following expression is obtained for the optimal shim field offset $\boldsymbol{b_{s|o}}$, with $\Delta p = p_{in} - p_{ex}$:

$$\boldsymbol{b_{s|o}} = (\boldsymbol{b_{s|ex}} p_{in} - \boldsymbol{b_{s|in}} p_{ex})/\Delta p \quad [5.6]$$

Likewise, for the optimal coupling coefficients relating pressure to shim field $\boldsymbol{c_s}$:

$$\boldsymbol{c_s} = (\boldsymbol{b_{s|in}} - \boldsymbol{b_{s|ex}})/\Delta p \quad [5.7]$$

5.3.3 Shim optimization

Rather than attempt to optimize the field homogeneity over the entire field of view (FOV), the shim can be improved by constraining the optimization to a volume of interest (VOI). The simplest shim optimization consists of finding the vector of shim currents $\boldsymbol{i_s}$ that minimizes the

Euclidean norm $J_1 = \left\|\boldsymbol{MAi_s} + \boldsymbol{Mb_\chi}\right\|_2^2$, where $\boldsymbol{M}$ is the shim VOI-defining masking operator and has dimensions $[N_{voi} \times N_{img}]$, with N_{voi} being the number of voxels within the shim VOI. Entries of $\boldsymbol{M}$ corresponding to VOI voxels are equal to unity and are otherwise uniformly zero.

Given the non-orthogonality of the multi-coil shim basis, various current/field distributions can perform equally well in minimizing J_1 (i.e. the net residual field). By optimizing for the inspired and expired shim currents simultaneously, the overall conditioning of the system can be improved while enforcing some consistency between the pair of field distributions. Hence, by vertically stacking the field and current vectors, we aim to solve the combined system:

$$J_2 = \left\|\begin{bmatrix}\boldsymbol{MA} & \boldsymbol{0}\\ \boldsymbol{0} & \boldsymbol{MA}\end{bmatrix}\begin{pmatrix}\boldsymbol{i_{s|in}}\\ \boldsymbol{i_{s|ex}}\end{pmatrix} + \begin{bmatrix}\boldsymbol{M}\\ \boldsymbol{M}\end{bmatrix}\begin{pmatrix}\boldsymbol{b_{\chi|in}}\\ \boldsymbol{b_{\chi|ex}}\end{pmatrix}\right\|_2^2 + \lambda\left\|\begin{bmatrix}\boldsymbol{MA} & -\boldsymbol{MA}\end{bmatrix}\begin{pmatrix}\boldsymbol{i_{s|in}}\\ \boldsymbol{i_{s|ex}}\end{pmatrix}\right\|_2^2. \quad [5.8]$$

The horizontally concatenated matrix $[\boldsymbol{MA} \quad -\boldsymbol{MA}]$ (dimensions $[N_{voi} \times 2N_s]$) has the effect of penalizing differences in the resulting shim fields over the shim VOI between inspired and expired states: With a regularization parameter of $\lambda = 0$, the two vectors of shim currents ($\boldsymbol{i_{s|in}}$, $\boldsymbol{i_{s|ex}}$) become independent, as if J_1 were optimized separately; whereas in the limit of large λ, difference in the inspired and expired field maps (RIRO) is ignored, and the corresponding shim fields become identical.

On its own, the minimization of Eq. [5.8] does not guarantee a practical current solution. Hence, the *fmincon* function of MATLAB was used to find a constrained minimum to [5.8]: limiting the min and max current for each of the $N_s = 24$ channels to $\pm$ 1 A.(68) These optimal current distributions were used to solve for the shim field offset and coupling coefficients in Eqs. [5.6] and [5.7] via the relation $\boldsymbol{Ai_s} = \boldsymbol{b_s}$.

5.3.4 Real-time shim updates

In terms of the time-varying vector of shim currents $\boldsymbol{i_{s|t}}$, the scaling matrix $\boldsymbol{A}$, and the shim VOI operator $\boldsymbol{M}$, Eq. [5.5] can be written as

$$\boldsymbol{MAi_{s|t}} = \boldsymbol{Mc_s}p_t + \boldsymbol{Mb_{s|o}}. \quad [5.9]$$

From this, a direct expression for the optimal current for a given pressure p_t is obtained by means of the pseudo-inverse. Defining $\boldsymbol{X} = (\boldsymbol{A^T M^T MA})^{-1}\boldsymbol{A^T M^T M}$, the baseline offset current $\boldsymbol{i_{s|o}} = \boldsymbol{Xb_{s|o}}$, and $\Delta\boldsymbol{i_{s|t}} = \boldsymbol{Xc_s}p_t$, this formulation has the advantage of reducing the process of updating

the shims to the simple operations of multiplying a vector ($\boldsymbol{Xc_s}$, calculated only once) by the pressure scalar p_t and adding to the resulting product the vector of the baseline offset currents:

$$\boldsymbol{i_{s|t} = i_{s|o} + \Delta i_{s|t}} \qquad [5.10]$$

The training and update procedures are outlined in Figure 5.3.

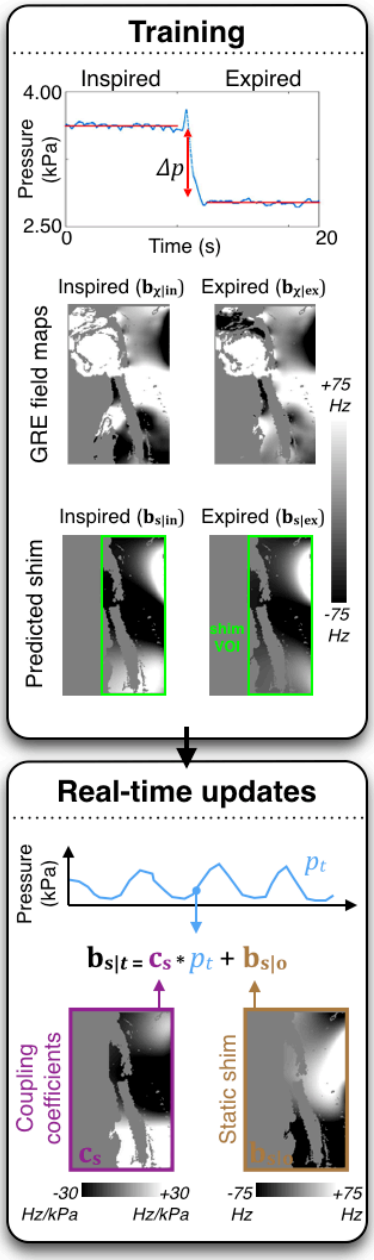

Figure 5.3: Demonstration of the real-time shimming training procedure. GRE field maps are acquired under inspired and expired conditions and the optimal shim currents for the 24-channel array are calculated, taking into account the non-linear amplifier constraints. The predicted shim

fields and their corresponding pressures yield the optimal pressure-to-shim field coupling coefficients c_s and the static shim term ($b_{s|o}$). In practice, real-time updates to shim currents are reduced to simply multiplying the scalar pressure reading p_t by a vector and adding to it a vector of pressure-independent DC offset currents.

In practice, the displacement of the lungs and the actual setting of the corrective shim current is likely to be asynchronous. In part, this can be due to (a) acoustic delay (i.e. between movement of the subject's abdomen and the ensuing change in pressure at the transducer), (b) digital I/O, (c) shim computation times, and (d) finite coil inductances and finite amplifier response (i.e. rise) time. Computation times were observed to be less than 1 ms. We assume that, for the small changes in shim current between updates, the contribution from (d) is small, and that the total delay (estimated as $\tau = 130$ ms) is dominated by (a) and (b): the acoustic delay (44 ms) and data overhead (86 ms).

To compensate for the delay, a prospective shim correction is performed (100): anticipating the pressure recording by means of a local polynomial fit.(17) To predict the respiratory trace at time t_k, a simple option is to perform a Taylor expansion around a previous measurement at time t_j where $t_k - t_j = \tau \geq l\Delta t$, Δt is the time between adjacent pressure samples, and l is the order of the expansion: Eq. [5.10] can be written as $\boldsymbol{i_{s|t_k}} = \boldsymbol{i_{s|o}} + \boldsymbol{X c_s} p_{t_k}$, which, expanded with $l = 1$, becomes

$$\boldsymbol{i_{s|t_k}} \approx \boldsymbol{i_{s|o}} + \boldsymbol{X c_s}\left(p_{t_j} + \tau \left.\frac{dp}{dt}\right|_{t_j}\right) \qquad [5.11]$$

To lessen the effect of noise within the recorded pressure on the forecasted signal (p_{t_k}), an order-1 Savitzky-Golay filter was used with a window size of 50 ms (5 samples, $\Delta t = 10$ ms) to estimate p_{t_j} and the corresponding rate of change. That is, immediately prior to each shim update, the 5 most recent pressure measurements were used to project the existing pressure trace forward in time by $\tau = 130$ ms.

5.3.5 In vivo experiments

Real-time shimming was demonstrated on 6 healthy adult volunteers from whom informed consent was obtained. The study was first approved by the Comité mixte d'éthique de la recherche du Regroupement Neuroimagerie/Québec.

As described below, the experiments involved specific breathing exercises: 10 s breath-holds (under inspired or expired conditions), or free breathing. Prior to scanning, subjects were walked through the experimental protocol and asked to maintain, to the best of their ability, a natural and consistent form for the breath-hold and free breathing exercises. Subjects were told not to grossly exaggerate the depths of the inspired/expired breath-holds relative to normal respiration, and to take measured breaths for the free breathing exercise so as to be similar in intensity to the preceding breath-holds. These instructions were again repeated over the intercom upon beginning the scan and, for the breath-holds, a countdown was devised to improve consistency, i.e. "breathe in… breathe out… breathe in… hold…" whereupon the scan commenced, with the subject freely breathing again upon its completion.

For each subject, conventional static optimization of the central frequency (f0) and scanner shims (the three offset terms of the imaging gradients, plus the five 2nd order shims) was first performed during free breathing using the standard double-echo steady state sequence (DESS). To train the real-time shim updates, GRE field maps were acquired in inspired and expired respiratory states with acquisition and phase processing parameters similar to those described in our previous work.(70) Pressure measurements were recorded during each of the field map acquisitions, with the difference in their respective median values used as Δp in Eqs. [5.6] and [5.7]. The shim VOI $\boldsymbol{M}$ was generally prescribed as the full set of GRE field map voxels for which reliable field measurements could be obtained: This was defined empirically as the intersection of regions over which the absolute field measurements $|\boldsymbol{b}_{\chi|in}|$ and $|\boldsymbol{b}_{\chi|ex}|$ were both less than 600 Hz, and where their maximum absolute difference $|\boldsymbol{b}_{\chi|in} - \boldsymbol{b}_{\chi|ex}|$ was less than 250 Hz, with the latter threshold loosely informed by previous RIRO measurements observed near the spinal cord at 3 T.(15) To assess the effect of the VOI selection, the shim VOI was further adjusted for subjects iv-vi: for subject iv, only the inferior half of the FOV along the readout was included (upon inspection of the field maps, RIRO was here observed to be greatest); and for all 3 subjects, the shim VOI was narrowed slightly along anterior-posterior dimension to avoid incorporating the highly paramagnetic lungs or the region medial to them into the shim optimization (Figure 5.4). Using the training field maps from the first subject, for which no regularization was applied in the optimization ($\lambda = 0$ in Eq. [5.8]), the L-curve method was employed to empirically select a regularization parameter of $\lambda = 0.1$ which was adopted for all the subsequent subjects.

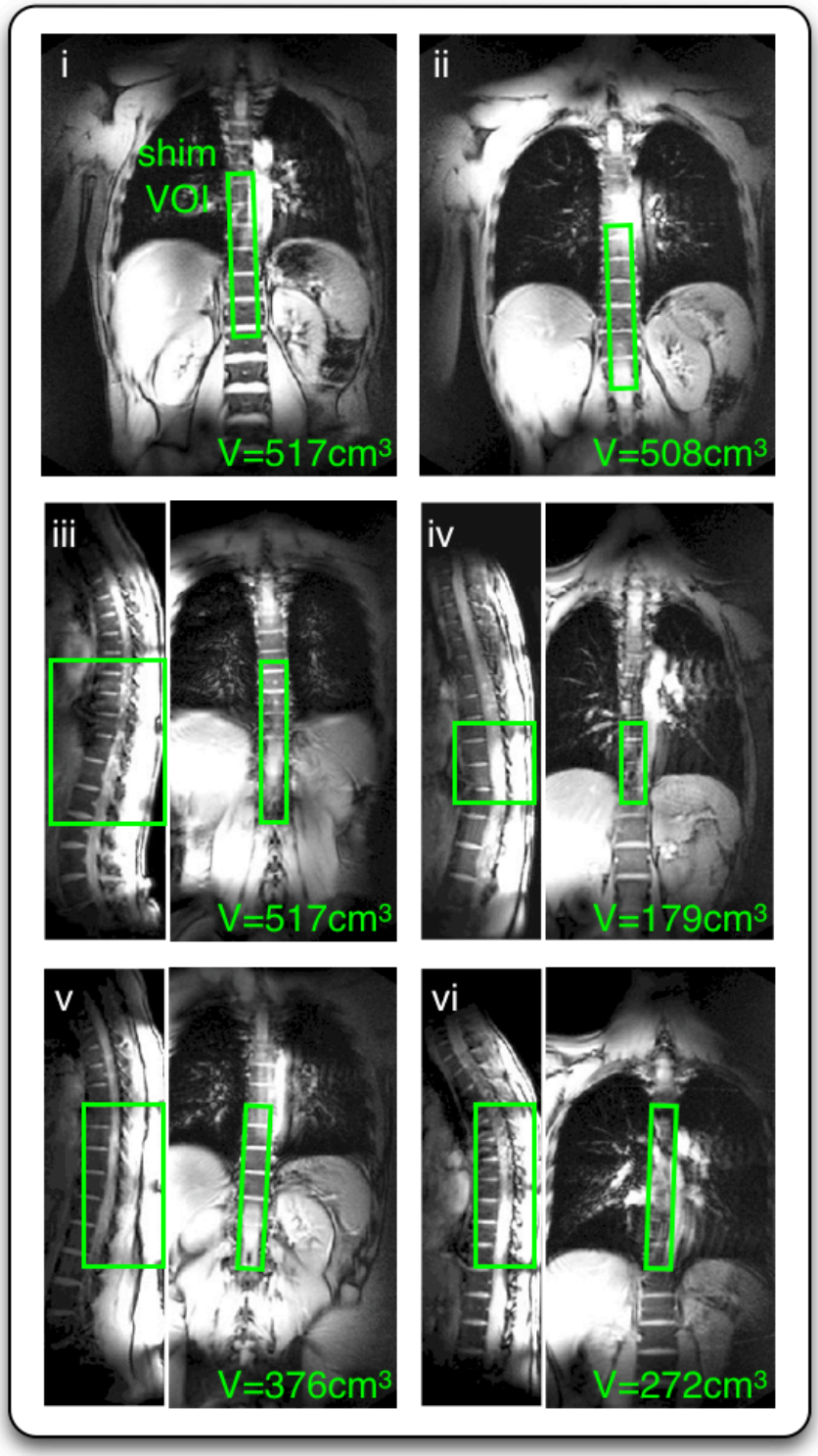

Figure 5.4: Anatomical localizer images in coronal view for subjects i-vi indicating the lower thoracic regions targeted in the shim optimization (shim VOI), with the volume indicated in the bottom right corner of each image. Sagittal views are inset on the left for subjects iii-vi.

The optimal shim field offset $\boldsymbol{b_{s|o}}$ and coupling coefficients $\boldsymbol{c_s}$ were determined via Eqs. [5.6] and [5.7]. Real-time shim updates were computed according to Eq. [5.11] and issued every 250 ms based on the respiratory trace sampled at 100 Hz.

To demonstrate the effect of real-time shimming on the field itself, GRE field maps were reacquired for the inspired and expired breath-holds with the currents of the 24-channel spine shim scaled in real-time by the respiratory trace. The effect of RIRO was further explored using a 2D single-shot GRE-EPI sequence typical of fMRI, performed with and without real-time shimming. This sequence used the following parameters: TE=16 ms, volume TR=500 ms; flip angle 50°; bandwidth=1630 Hz/pixel; R=2 acceleration factor using GRAPPA; partial Fourier=6/8; spatial resolution=1.5x1.5 mm^2 in-plane, with 3 sagittal slices of thickness 3.0 mm centred on the spinal cord, for an effective FOV=192x192x9 mm^3. EPI data were acquired for both breath-holds, and again for free breathing. For the free breathing exercise, 60 image volumes were acquired, for a total acquisition time of 30 s.

5.3.6 Analysis

The effect of real-time shimming was characterized by several measures: static field inhomogeneity was assessed via the standard deviation of the individual field maps over the full shim VOI, while RIRO was assessed via the absolute field difference between the inspired and expired breath-holds over the same region. The individual field maps and the RIRO field difference maps were further scaled to voxel displacement maps by dividing by the phase encode bandwidth of the acquired EPI (22.32 Hz/pixel) in order to provide a proxy measure of the geometric distortion affecting the EPI.

Respiration-induced differences in the EPI themselves were assessed directly via the absolute percent-difference of the inspired and expired EPI magnitude images:

$$\Delta \boldsymbol{EPI} = \boldsymbol{M_{SC}} \frac{|\boldsymbol{EPI_{in}} - \boldsymbol{EPI_{ex}}|}{(\boldsymbol{EPI_{in}} + \boldsymbol{EPI_{ex}})} \times 200\% \qquad [5.12]$$

where $\boldsymbol{M_{SC}}$ is an anatomical segmentation of the spinal canal (cord + CSF) obtained via the Spinal Cord Toolbox (85,109,110), using the distortion-free GRE magnitude images as input. Because the large shim VOI generally contained very little EPI signal anterior to the spinal cord,

and because the tissue posterior to it is of little interest to the anticipated clinical applications, the spinal canal VOI was adopted to restrict the analysis to a region where the intensity of the EPI was relatively high and relatively uniform; however, any arbitrary region within the shim VOI could suitably serve for the comparison.

Lastly, the temporal signal-to-noise ratio (tSNR) of the EPI magnitude was calculated as the average intensity of a voxel across the time series divided by its standard deviation. As with the breath-hold comparison, tSNR was calculated over the spinal canal VOI. However, as geometric distortion (both static and dynamic) tended to map signal outside the actual spinal canal, a calculation of tSNR over the actual anatomical location of the canal could speciously favor the least statically distorted acquisition. As tSNR is further governed by intra-voxel dephasing – upon which respiration and shimming will exert some effect, beyond that of mere distortion – it was judged more appropriate to tailor $\boldsymbol{M_{SC}}$ to the specific acquisition (original vs. real-time shimming) to ensure that the segmentation in each case fully encompassed the spinal canal throughout the breathing exercise. Hence, $\boldsymbol{M_{SC}}$ was adjusted along the phase encode direction according to the predicted voxel displacements: inspired and expired voxel displacement maps were averaged independently for each condition (with and without real-time shimming) and, for each slice and for each image row, voxel displacements within the spinal canal were used to adjust $\boldsymbol{M_{SC}}$ anteriorly/posteriorly.

5.3.7 In silico experiment

The theoretical capability of the 24-channel spine shim to compensate RIRO across the spinal cord was compared with that of the conventional spherical harmonic basis (0^{th} through to 5^{th} order, inclusive) via simulation. As the shim VOI adopted for the in vivo experiments was chosen heuristically with the EPI in mind, the anatomical segmentations of the thoracic spinal canal were judged more appropriate target VOIs for the comparison. This was similar to a previous virtual shim system comparison performed on a set of static inspired field maps.(70) As the current work focuses on correcting RIRO, simulated shimming was performed directly on the field difference maps ($\Delta \boldsymbol{b_{orig}} = \boldsymbol{b_{\chi|in}} - \boldsymbol{b_{\chi|ex}}$) from the original in vivo breath-holds of 4 subjects. The relative residual RIRO (RR) after shimming was compared across systems (multi-coil vs. spherical harmonic): $RR = \|\boldsymbol{M_{SC}}\Delta \boldsymbol{b_{shimmed}}\| / \|\boldsymbol{M_{SC}}\Delta \boldsymbol{b_{orig}}\|$. Both the current-limited

(1A per channel) and ideal (limitless) cases were considered for the multi-coil array, and all spherical harmonic shim optimizations were unconstrained and given by the pseudo-inverse.

5.4 Results

Figure 5.5 and Figure 5.6 exhibit the effect of real-time shimming on the magnetic field for the breath-hold field maps. Averaged across breath-hold acquisitions and across 5/6 subjects, real-time shimming reduced the field inhomogeneity over the full shim VOI (370 ± 147 cm^3) by an average of 33.0 ± 11.2 % (mean ± standard deviation). Subject 3, for which no real-time shimmed field maps were acquired, was excluded from the calculation of this set of group statistics; however, the predicted relative reduction in field inhomogeneity under real-time shimming of 33.4 ± 0.4 % was nevertheless consistent with the other subjects. Concerning RIRO specifically, real-time shimming reduced the mean absolute difference between inspired and expired fields across the shim VOI from 50.3 ± 8.0 Hz down to 20.9 ± 7.0 Hz across 5/6 subjects, constituting a relative reduction of 59.1 ± 11.1 %.

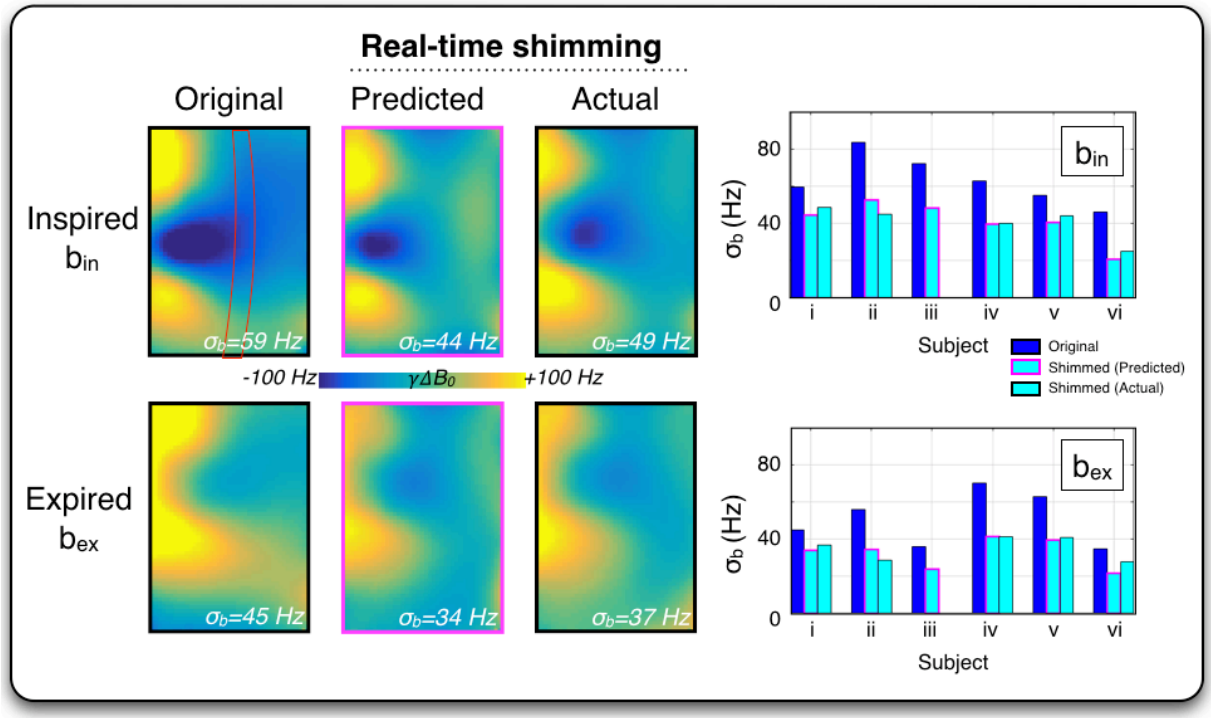

Figure 5.5: Field inhomogeneity over the full shim VOI under inspired (b_{in}, top row) and expired (b_{ex}, bottom row) breath-hold conditions: prior to application of the multi-coil shims (Original) and, using real-time multi-coil shimming (Predicted, and Actual). The field inhomogeneity is

quantified as its standard deviation (σ_b) over the shim VOI. Example field images for a single subject (i) are shown (left), with the spinal canal traced in red in the top left panel for reference. Measurements across subjects are depicted on the right. Excluding subject iii, for which no real-time shimmed field maps were acquired, real-time shimming reduced inhomogeneity across subjects an average of 33.0 ± 11.2 %.

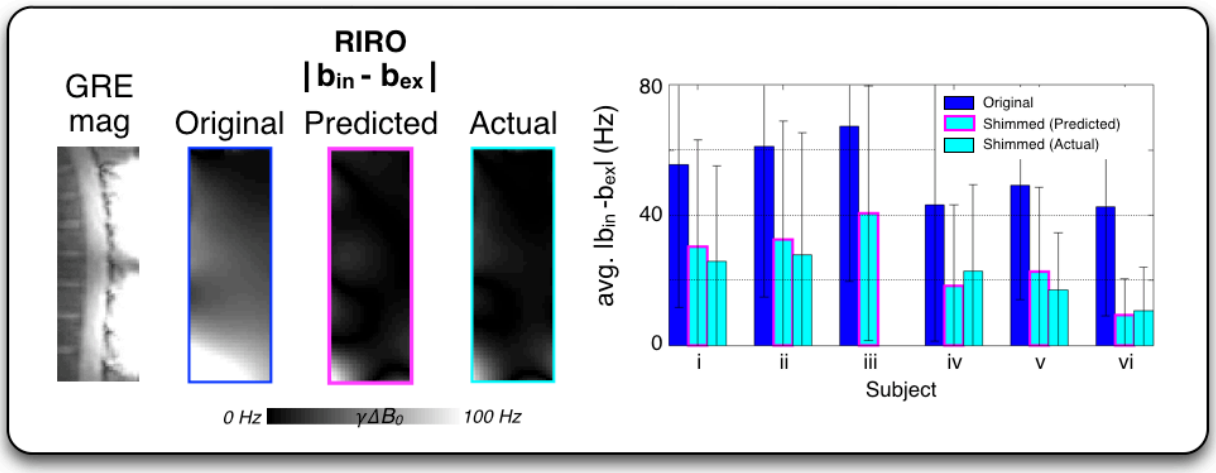

Figure 5.6. Respiration-induced resonance offset (RIRO) over the full shim VOI under breath-hold conditions: before real-time shimming (Original) and after (Predicted and Actual). Example RIRO for a single subject (vi) are depicted on the left as the absolute difference between the inspired and expired fields (|bin - bex|) with the GRE magnitude image (TE=4.92 ms) included for anatomical reference. On the right, average RIRO and its reduction under real-time shimming are plotted for each subject, with bars indicating the standard deviation over the shim VOI. Real-time shimming reduced the mean absolute difference between breath-hold fields by 59.1 ± 11.1 % across subjects (again, excluding iii).

Similar reductions to voxel displacements are observed in Figure 5.7 for a single subject and Figure 5.8 for all subjects. Averaged over the two breath-holds and across subjects (again excluding Subject 3), real-time shimming reduced the median static voxel displacement by 36.6 ± 20.8 %. The median voxel displacement due to RIRO (i.e. the inspired – expired field difference) was reduced 67.5 ± 10.8 % (average ± standard deviation of the median across subjects). Looking to the EPI themselves, and to the spinal canal VOI specifically, the average median percent-

difference between the breath-holds ($\Delta\boldsymbol{EPI}$ in Eq. [5.12])) was reduced 19.3 ± 6.9 % across subjects, from 40.0 ± 11.1 % to 20.7 ± 7.3 % (i.e. a relative reduction of 48.2 ± 12.2 %).

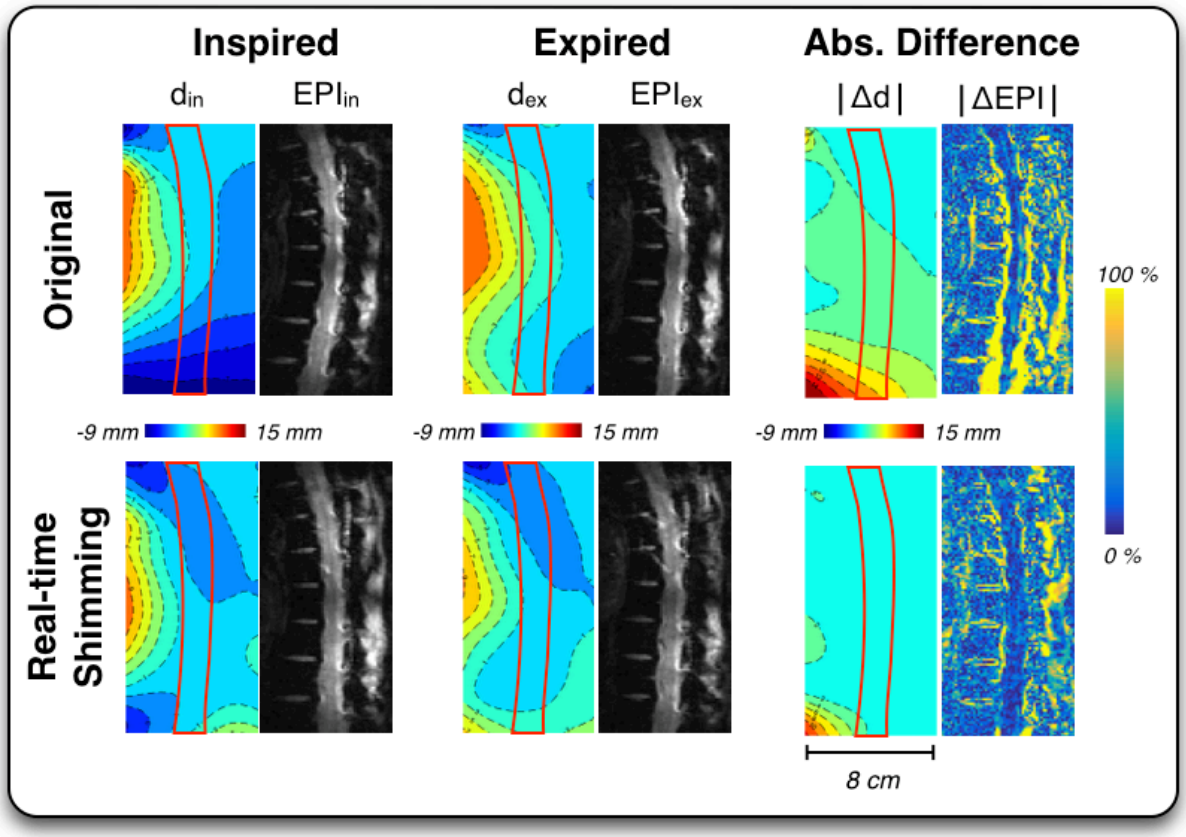

Figure 5.7: Voxel displacement contour maps and GRE-EPI under breath-hold conditions for a single subject (vi) using standard static shimming (Original, top row) and real-time multi-coil shimming (bottom row). The amount of displacement in the phase encode (AP) direction (inspired: d_{in}; expired: d_{ex}) is estimated using the GRE field maps. Difference images on the right depict the absolute displacement owing solely to respiration (|Δd|) and the normalized absolute difference (|ΔEPI|, calculated according to Eq. 12) between the inspired (EPI_{in}) and expired (EPI_{ex}) EPI. Though respiration-induced distortions within the spinal cord (traced in red) are effectively compensated, remaining field differences posterior to the cord cause some variability in the fat suppression within the region, hence the residual differences observed in the EPI even after shimming.

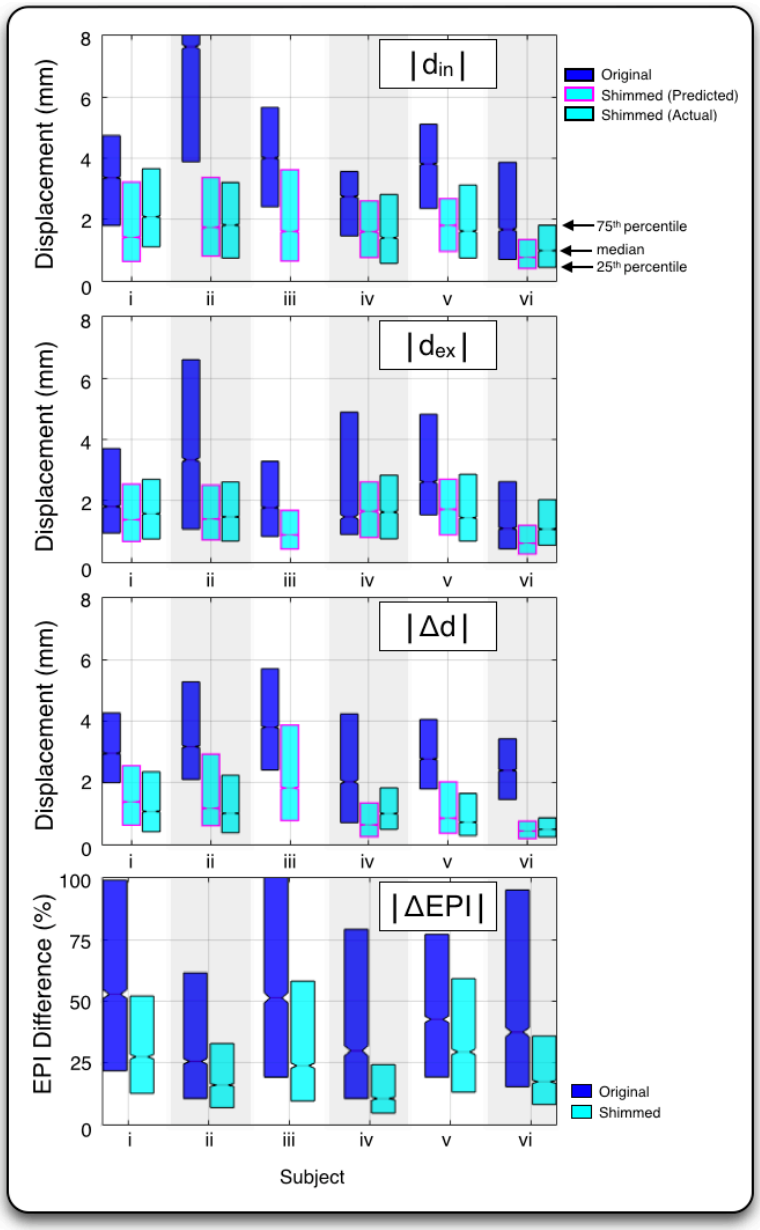

Figure 5.8: Absolute EPI voxel displacements across subjects as determined by the inspired and expired field maps ($|d_{in}|$ and $|d_{ex}|$, respectively, the 1st and 2nd rows) and their difference $|\Delta d|$ owing to RIRO (3rd row). Averaged over the two breath-holds and across subjects (excluding Subject 3), real-time shimming reduced the median static voxel displacement by 36.6 ± 20.8 %. The median voxel displacement arising from RIRO saw an average reduction across the same subjects of 67.5 ± 10.8 %. The bottom row displays the percent-difference of the breath-hold EPI over the spinal canal VOI (Eq. [12]), for which the median was reduced by 19.3 ± 6.9 % on average.

Over the distortion-adjusted spinal canal VOIs, real-time shimming improved the mean EPI tSNR across subjects ii-vi by an average 15.7 ± 7.9 %. The improvement was significant at the level of P=0.05 (paired Student's t-test). As Subject i was observed to have shifted slightly to their right (< 3 mm) between the acquisitions of the original GRE field maps and the EPI under free breathing, this subject was excluded from the calculation of group tSNR statistics. Figure 5.9 exhibits the results of two subjects and summarizes the group statistics. In terms of volume, the distortion-adjustments of the spinal canal VOIs were small: All original spinal canal VOIs were between 30.0 and 32.0 cm^3 (though only the 18 cm^3 within the shim VOI was considered for subject iv) and, upon adjustment, the difference in net volume between the original and real-time shimming cases was less than 1.0 cm^3 (except for subject iv, for which the adjusted volume was 1.1 cm^3 larger in the unshimmed case). The effect of these small adjustments was merely to shift the VOI where necessary by several mm to ensure that the distorted spinal canal was indeed contained within the selected volume.

Finally, Figure 5.10 summarizes the result of the shim system comparison. To facilitate comparison between the simulated and the actual experimental results, the system comparison only included 4/6 subjects since field maps were not reacquired for Subject iii under real-time shimming, and the small shim VOI adopted for Subject iv only spanned 3 vertebrae whereas the simulations covered the full spinal cord sections contained in the acquired FOV. In the 1A per channel current-limited case, the performance of the 24-channel multi-coil array for RIRO correction compares to that of a full 4^{th} order set of spherical harmonic coils. Without limitations on current, the multi-coil array appears to outperform even a full 5^{th} order set (36 terms) of spherical harmonic shims; however, as the maximum optimal currents in the idealized case were consistently in excess of 100 A per channel for each of the 4 subjects, the multi-coil fields are not currently realistic.

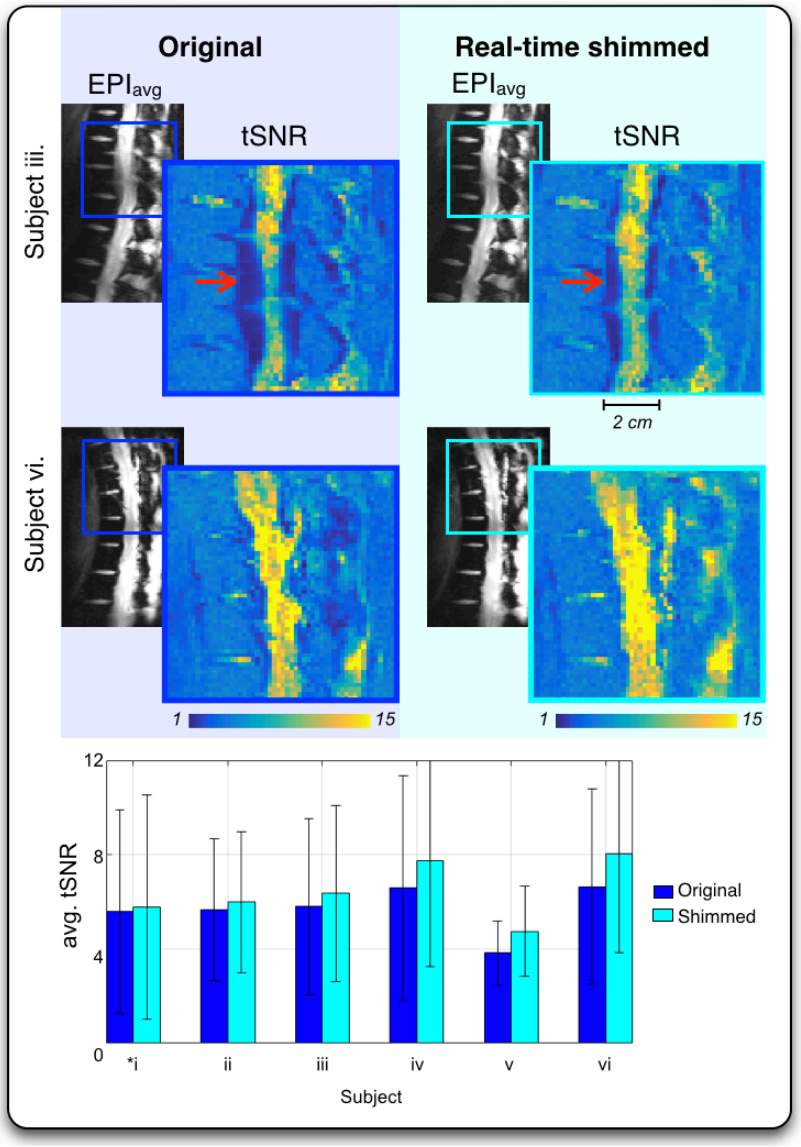

Figure 5.9: Improved EPI tSNR with real-time shimming. The upper half of the panel features the time-averaged EPI (EPI_{avg}) from the free-breathing time-series and 2.5X zoomed insets of the corresponding tSNR maps for two subjects. Red horizontal arrows point to regions of marked respiration-induced distortion which appear as focal signal nulls, the size and severity of which are reduced upon real-time shimming. The lower panel summarizes group statistics: mean tSNR across the spinal canal VOI is plotted for subjects i-vi, whereas for subject *i, who was observed to have shifted slightly during the scan, the given tSNR refers to the average calculated over the full shim VOI. Bars indicate the tSNR standard deviation over the respective VOI. Real-time shimming improved the mean EPI tSNR across subjects ii-vi an average of 15.7 ± 7.9 %.

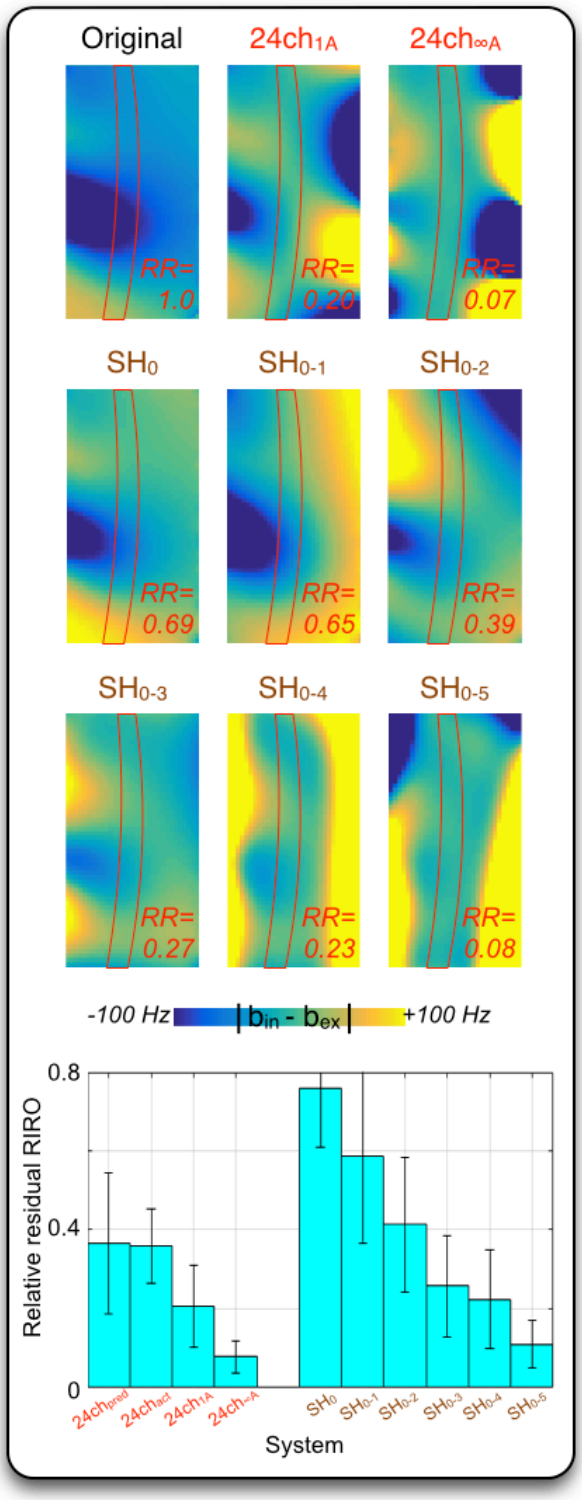

Figure 5.10: System comparison of relative residual RIRO. Simulated shimming was performed directly on the original field difference maps (b_{in} - b_{ex}) and the shimmed residual (L2 norm of the resulting field over the spinal canal VOI) is expressed as a ratio to the original residual. The top 3

rows depict the simulation results for Subject i: The top row features the original field difference (left) alongside the simulated shims using the 24-channel multi-coil array with currents limited to 1A per channel ($24ch_{1A}$, middle), and with limitless current ($24ch_{\infty A}$, right). Rows two and three feature the simulated shims using an ideal spherical harmonic basis up to 5^{th} order ($SH_{0\text{-}5}$). The lower chart features the average relative residuals across 4 subjects, with the thin bars indicating the standard deviations. The leftmost blocks ($24ch_{pred}$ and $24ch_{act}$) refer to the predicted and actual relative residual fields over the spinal canal when the 24-channel array was optimized over the full shim VOI of the actual experiments (i.e. they correspond to the difference between the two rows of Figure 5.5).

5.5 Discussion

This study presented a technique for real-time multi-coil shimming to address the problem of respiration-induced resonance offsets (RIRO) in spinal imaging. Applying this technique to single shot GRE-EPI reduced geometric distortion and increased tSNR, which should translate directly into greater statistical power for BOLD-based fMRI of the spinal cord. The following section discusses limitations to the technique – actual or anticipated – and touches on potential solutions.

An advantage to the approach introduced here and embodied in Eq. [5.10] is its simplicity, both conceptual and numerical: a baseline DC shim component addresses the static field variation (e.g. residual lung volume) and a slowly varying AC component corrects for dynamic RIRO effects; hardware constraints are accounted for at the training stage, such that no real-time optimization is required when updating the shims. Indeed, insofar as the inspired and expired fields of the training acquisitions (and the respiratory pressures to which they correspond) tend to resemble the effective extrema for a given subject, no explicit limiting of the shim currents was necessary during real-time updating. To this end, by constraining the shim currents in the initial optimizations to 1 A per channel, some headroom was nevertheless left available for the currents relative to the upper-limit set by the amplifier, which is technically capable of outputting 5 A per channel. This dialing back of currents in the optimization relative to the available limits was done both to alleviate the power demand on the amplifier as well as to alleviate the physical demand placed on the subjects by the expired breath hold: that is, a partial-exhalation would sufficiently

capture the linear variation in RIRO for shim training, while a more profound exhalation, should one occur later during real-time shimming, would not cause the amplifier to clip.

At a duration of 10 s, the breath-hold for the shim training could be challenging to maintain, even for healthy subjects and particularly under full-exhalation. Indeed, several healthy volunteers from an earlier cohort (111) (all of whom were between the ages of 20 to 40 years old) complained of discomfort specifically from having to modulate their breathing in the scanner, with one volunteer requesting to be let out halfway through the training, prematurely ending the experiment. This apparent anxiety likely stems from the mixture of claustrophobia and immobility typical of MRI scans – though potentially aggravated by the respiratory belt – combined with a hyperawareness of one's own breathing prompted by the breath-hold and measured breathing exercises. This lead us to adopt a more careful approach to coaching the subjects prior to scanning, as described earlier in Experiments. The respiratory belt created an additional problem for one subject (who was later rescanned) as large amplitude breaths caused the bellows to slip following the training scans, thereby altering the pressure-to-field relation: with the loosened belt, inhalation elicited pressures/shim currents that had previously been associated with exhalation, which, evidently, defeated the purpose. Ultimately, insofar as the aim of real-time shimming is to improve the quality of advanced MR techniques (fMRI, DTI, MRS, etc.) to make them suitable for clinical use (i.e. for characterizing spinal cord function, pathology, and response to treatment), real-time shimming must be, first and foremost, straight-forward to implement, which means paying special attention to the question of patient comfort and practicality.

This points to the advantages of alternative training techniques, for instance, using field maps acquired rapidly via EPI (17) or single-slice FLASH (93), and/or respiratory tracking techniques such as navigator echoes (54,96) or field probes (88,108,112). These alternatives avoid training scans involving breath-holds while further enabling the correction of dynamic field distortions from sources other than respiration (e.g. patient movement (54,113), eddy currents, and thermal drift (102)). For any of the given alternatives, the general algebraic framework introduced here for managing the real-time shim updates could nevertheless prove useful and could be easily extended to accommodate multiple respiratory/field sensors, with p_t becoming a row vector and $\boldsymbol{c_s}$ gaining columns to become a matrix.

Further refinement of the framework for updating the shims may be possible vis-à-vis refinement to the underlying model of RIRO. That is, the validity of the linear pressure-to-field relation of Eq. [5.2] has been taken for granted and, as speculated by van Gelderen et al., "there may be phase [i.e. field] variations induced by the respiration that are not linearly related to the measured chest position [i.e. pressure]." (17) Other studies of RIRO, using a field probe placed next to the breast (88), rapid EPI-based field mapping in the brain and brain stem (114), and rapid FLASH-based field mapping in the cervical spine (87) support the earlier speculation. By acquiring additional training scans at different points in the respiratory cycle, the linear model could likely be improved upon by considering the instantaneous respiration rate (114); for example, an alternative to Eq. [5.2] that incorporates an additional set of coupling coefficients $c_{\chi 1}$: $b_\chi(\boldsymbol{r}, t) = c_{\chi 1}(\boldsymbol{r})dp(t)/dt + c_\chi(\boldsymbol{r})p(t) + b_{\chi|o}(\boldsymbol{r})$. It is probable that some portion of the observed intersubject variability in image improvements under real-time shimming are due to underlying anatomical differences to which a more sophisticated model could be better adapted.

Evidently, the shim protocol and hardware could also be further optimized, for instance, by updating the shims more rapidly, by issuing slice-wise ("dynamic") updates (57,60,62,75,115), and by jointly optimizing the spherical harmonic shims of the scanner along with the multi-coil array. Ultimately, what constitutes an optimal approach will strongly depend on the imaging application and the region targeted: Although the 24-channel multi-coil array used here has some advantages over conventional low-order spherical harmonic shims in terms of its low coil inductances (ideal for dynamic applications) and its ability to produce relatively complex longitudinal field variations (e.g. Figure 5.10), for a sufficiently small shim VOI and an amplifier of sufficient power and bandwidth (e.g. those of the imaging gradients), the systems may be roughly equivalent for the purpose of shimming. Furthermore, given that simply repositioning the patient can have a dramatic effect both on the magnetic field and the ability of a shim system to correct it (116), there is unlikely to be a single panacea for the general case of correcting ΔB_0 across the entire spinal cord. Nevertheless, the present study has demonstrated that real-time correction of respiration-induced distortions in the spinal cord is possible to a large degree, suggesting future improvements to EPI, T2*-imaging, and spectroscopy.

5.6 Acknowledgements

We thank the team at Resonance Research Inc. for their assistance with the shim hardware and for providing the shim coil wire patterns (https://osf.io/4pe6r/); André Cyr and Carollyn Hurst (Functional Neuroimaging Unit, CRIUGM) for their assistance conducting the experiments; Jason P. Stockmann for his mentorship, along with Robert L. Barry and Marta Bianciardi (all at the A.A. Martinos Center for Biomedical Imaging) for the helpful discussions; and, finally, the reviewers for their insightful critiques.

CHAPTER 6 GENERAL DISCUSSION

In Chapter 4, a unique 24-channel multi-coil shim array was introduced and its performance for static shimming was demonstrated in a series of experiments. In Chapter 5, a technique for prospective, real-time shimming was proposed and subsequently demonstrated using the 24-channel shim. Having discussed the merits of these methodologies in the preceding chapters, the following sections will expand on their limitations and, where possible, propose solutions.

6.1 Shim experiments and hardware considerations

6.1.1 24-channel local shim array

To set the stage for the introduction of the 24-channel shim array in Chapter 4, we appealed to the statement by Stroman et al. (5) in support of the need for improved shimming: "Magnetic field inhomogeneity is the greatest challenge to MRI of the spinal cord." Naturally, the statement presumes that the gamut of other technical challenges inherent to MRI, such as RF transmit and receive performance, have already been effectively addressed. The cautionary concluding words of Stockmann and Wald (117) serve as an apposite rejoinder: "Whatever choice is made for shim hardware, careful integration with the other scanner sub-systems will be critical."

While Chapters 4 and 5 provided accounts of improved B_0 uniformity using the 24-channel shim, the improvements came at the expense of some reduced RF performance. Briefly, due to the unshielded design of the 24-channel shim, its presence in the bore would almost certainly reduce the Tx efficiency of the integrated body-coil normally used for RF excitation; rather than overload the body-coil and risk damaging it (e.g. anticipating automated Tx voltage adjustments), a decision was made erring on the side of caution: the two coil arrays were not to be used simultaneously. Hence, a custom transceiver array had to be employed instead. Unfortunately, the sensitivity of our custom transceiver was poor, partly due its inhomogeneous B_1^+ excitation profile (e.g. Figure 6.1 below). This feature also explains why the EPI tSNR levels reported in the previous study (e.g. Figure 5.9) generally remained low despite improvements afforded by real-time shimming.

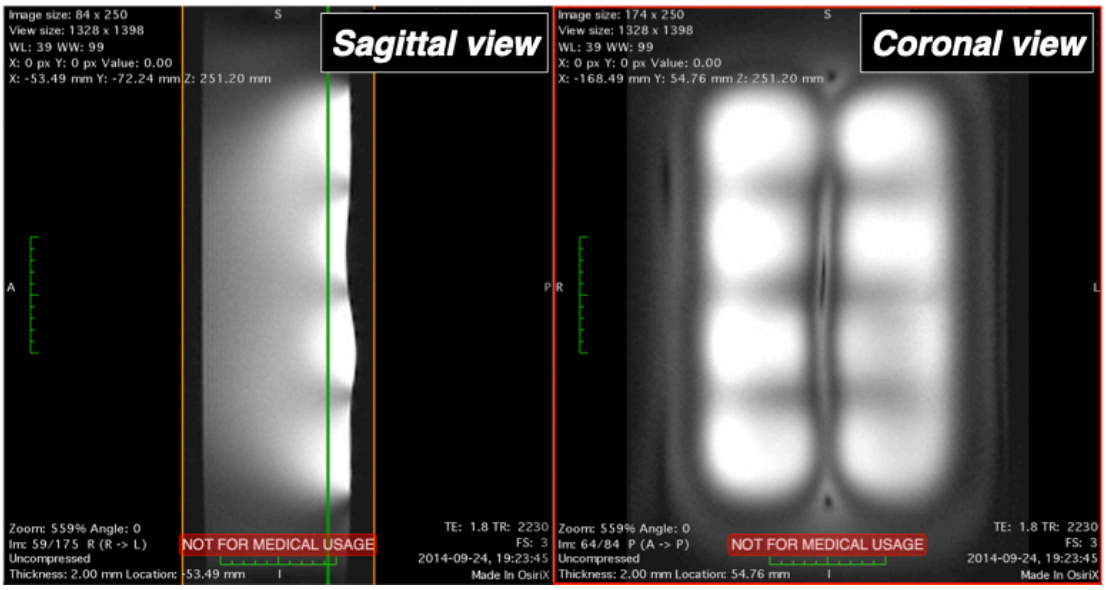

Figure 6.1: Magnitude images of rectangular water-filled box illustrating the inhomogeneous intensity artifacts resulting from the nonuniform B_1^+ profile of the custom 8-channel transceiver array. The problem is particularly evident as the darkened region in the middle of the coronal image (i.e. for a human subject, this is roughly where the spinal cord would be situated).

Whether the 24-channel shim could be made compatible with the body Tx coil, or whether the custom transceiver could be adequately improved are open questions. Nevertheless, given the present opportunity-cost associated with the use of the dedicated 24-channel shim, outright compatibility with existing MRI subsystems would be an attractive feature of any alternative shim technology.

6.1.2 An 8-channel AC/DC coil for the cervical spinal cord

A promising shim technology that could avoid the trouble of redesigning multiple MRI subsystems is the integrated "AC/DC" coil design that was introduced in section 2.3.1. Due to their low inductance, the coil arrays should be readily compatible with integrated Tx/body coils. Moreover, the modification does not compromise parallel imaging performance (68), which, as described earlier in section 1.4.4, can be just as important as shimming for reducing certain ΔB_0 artifacts (e.g. distortion in EPI (18)**)**. To this end, we built an 8-channel AC/DC array for the cervical spinal cord (Figure 6.2). Details relating to the design and construction of the coil, along with initial experiments have been presented at several annual meetings of the ISMRM (86,118,119).

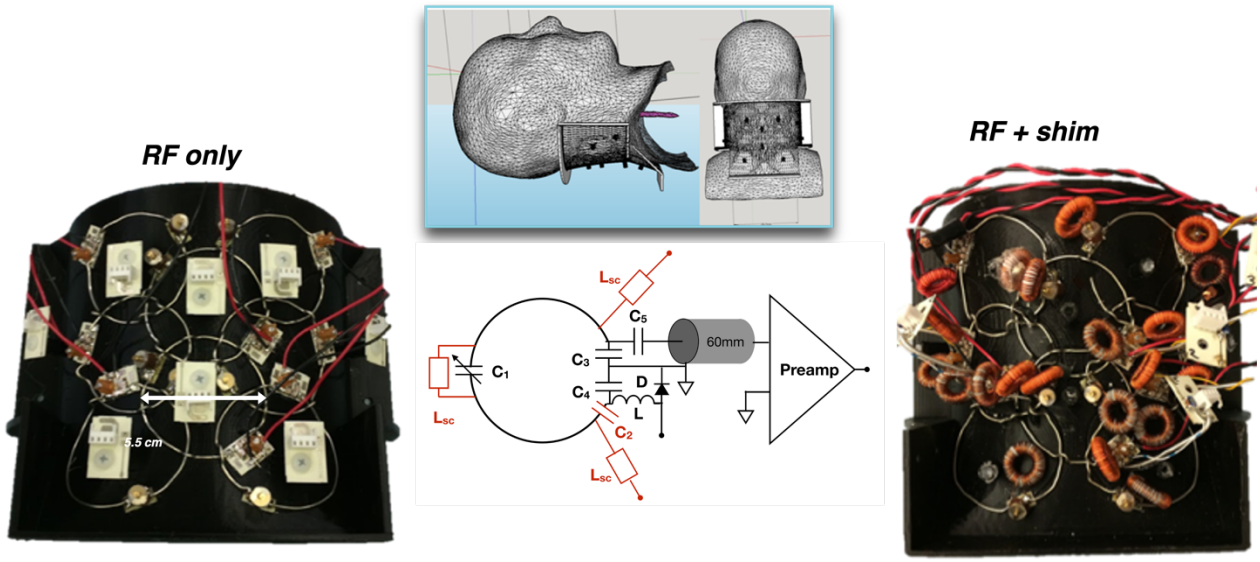

Figure 6.2: 8-channel AC/DC array for the cervical spinal cord. Photos show the coil before (left) and after (right) incorporating the toroidal chokes and twisted wire pairs that enable a DC shim current to flow along each element.

Before continuing the general discussion in the following sections, it will be useful to highlight an early experimental result obtained using the 8-channel AC/DC coil.

Recalling the model introduced in the preceding chapter (71), we will assume that the longitudinal magnetic induction $\mathbf{b}_{\chi|t}$ at any given time t decomposes, simply, into a static component $\mathbf{b}_{\chi|o}$, and a time-varying component $\mathbf{c}_{\chi}p_t$ that depends linearly on the instantaneous respiratory state of the subject,

$$\mathbf{b}_{\chi|t} = \mathbf{c}_{\chi}p_t + \mathbf{b}_{\chi|o} \qquad [6.1]$$

By acquiring two GRE field maps under inspired and expired breath-holds, while concurrently recording the respiratory trace p_t from a set of respiratory bellows, one can solve for $\mathbf{c}_{\chi}$ and $\mathbf{b}_{\chi|o}$ and, therefore, calibrate real-time shim updates.

In our first in vivo experiment, the aim was to get a basic sense for how effective the AC/DC coil might be at correcting field changes due to breathing. We followed the same dual breath-hold/dual-echo GRE protocol for a single subject, however, rather than solve for static and dynamic components separately, we simply shimmed the inspired and expired field maps independently. We also acquired EPI in both respiratory states to illustrate the relation between B_0 offset and voxel-shift in the phase encoding direction. Results are illustrated in Figure 6.3.

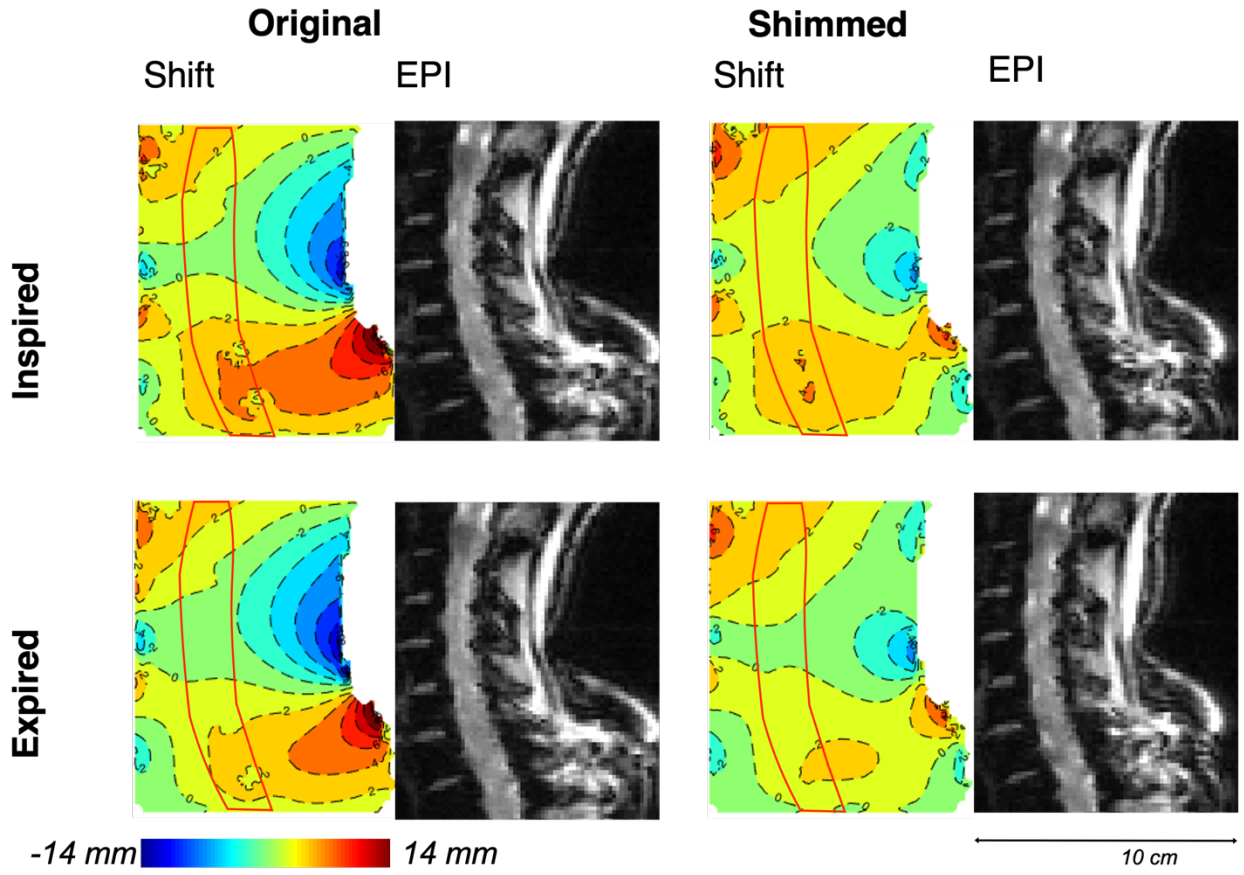

Figure 6.3: Shimming the neck using the 8-channel AC/DC coil. Sagittal EPI and GRE field maps were acquired during inspired and expired breath-holds—first with the AC/DC shim off (**Original**) and, again, with optimized currents applied to the AC/DC shim (**Shimmed**). The field maps as shown have been scaled to reflect EPI voxel-shift. The entirety of the depicted region was included in the shim optimization. The spinal canal is contoured in red in the voxel-shift maps as a visual aid.

Field uniformity and EPI fidelity were both seen to improve after shimming with the 8-channel coil. However promising, a close inspection of Figure 6.3 reveals a curious feature: the largest field shifts (and improvements upon shimming) are observed at the back of the neck rather than the region nearest the lungs. This suggests that movement (i.e. rotation of the head) between breath-holds was the predominant source of field variation rather than susceptibility differences within the thorax. Notably, the subject had been coached to remain still and to take natural (unexaggerated) breaths. Recent investigations by Power et al. (120) bear this out: indeed,

subjects tend to rotate their heads during breathing, which complicates the analysis of fMRI time-series data.

6.1.3 Real-time field mapping and shimming

While the effects of head rotation during respiration may be less significant below the neck in the noncervical sections of the spinal cord, nonetheless, the inspired-expired training protocol for real-time shimming presents at least two possible issues, irrespective of the imaging region: 1) it requires a compliant subject, capable of holding their breath for several seconds on command; 2) preliminary studies have called into question the extent to which field-shifts measured between breath-holds truly correspond to the variation exhibited during free breathing.(14)

Hence, preferable would be a shim "training" protocol that requires no special instructions beyond the normal expectation that subjects remain still and, furthermore, one that accurately captures the pattern of field variation exhibited during normal breathing.

To this end, a cue was taken from a recent work at 7T (14) which quantified the field effects of respiration within the cervical spinal cord during free-breathing by means of a time-series of rapidly acquired, single-echo sagittal FLASH images. While the single-echo acquisition only allows for estimation of relative field changes between measurements, a second echo can be readily incorporated into each measurement by which a proper field map can be created for each *TR*—a technique we may refer to as *real-time field mapping*. Hence, by concurrently recording a respiratory (e.g. bellows) signal $\boldsymbol{p_t}$ during the image acquisition, the static $\mathbf{b_{\chi|o}}$ and respiratory $\mathbf{c_\chi}$ field components can be estimated from the time-series of field maps $\mathbf{b_{\chi|t}}$ via linear regression; for instance, in a least-squares sense, by minimizing the cost function:

$$J_f = \left\| \mathbf{b_{\chi|t}} - [\mathbf{1}\ \boldsymbol{p_t}] \begin{bmatrix} \mathbf{b_{\chi|o}} \\ \mathbf{c_\chi} \end{bmatrix} \right\|_2^2 \qquad [6.2]$$

Note that spatial and temporal constraints on each component could be incorporated through regularization.

Having solved for the two field components separately, it remains to determine the optimal shim currents for the static field and for the dynamic correction at a given respiratory phase (i.e. probe reading). That is, two components are sought for each shim channel: a set of static (DC)

coefficients, and a second set, in amps-per-unit-respiratory probe, for the dynamic correction. Due to the finite power limitations of any real shim system, the two components can become interdependent, as current already directed toward one component limits the available current for the other. Hence, in the optimization, the two components should be solved simultaneously and prioritized according to their relative significance. The latter may depend on the specific imaging application (i.e. the extent to which static and dynamic ΔB_0 fields can each generate artifacts will depend on the sequence).

One option is to allocate shim power ($\propto {i_s}^2$) based on the average power of each of the field components ($\propto {\Delta B_0}^2$) as calculated from the real-time field maps during shim training. To this end, prior to the shim optimization, one can scale the respiratory field component $\mathbf{c_\chi}$ by the root-mean-square (RMS) value of the respiratory recording $\boldsymbol{p_t}$ across the time-series: scaled in this way, the respiration-induced resonance offset (RIRO) $\Delta\mathbf{b_{\chi|RIRO}} = p_{RMS}\mathbf{c_\chi}$ and the static offset $\mathbf{b_{\chi|o}}$ become comparable (e.g. both in units of Hz) and, once squared (i.e. during the least-squares optimization) each contributes to the residual in proportion to its average power. For example, one can aim to minimize a cost function resembling the following:

$$J_s = \left\| \begin{bmatrix} \boldsymbol{A} & \mathbf{0} \\ \mathbf{0} & \boldsymbol{A} \end{bmatrix} \begin{pmatrix} \boldsymbol{i_{s|o}} \\ \Delta\boldsymbol{i_{s|RIRO}} \end{pmatrix} + \begin{pmatrix} \mathbf{b_{\chi|o}} \\ \Delta\mathbf{b_{\chi|RIRO}} \end{pmatrix} \right\|_2^2 . \qquad [6.3]$$

Once again, $\boldsymbol{A}$ is the matrix operator formed by the shim profiles/reference maps and serves to transform the vector of currents into a field vector. The vector of optimal scaling coefficients $\mathbf{c_\chi}$ (used to determine the real-time current updates as $p_t\mathbf{c_\chi}$) are retrieved from the solution vector as $\mathbf{c_\chi} = \Delta\boldsymbol{i_{s|RIRO}}/p_{RMS}$. Nonlinear constraints on the maximum absolute current-per-channel $\boldsymbol{i_{max}}$ can be enforced in the optimization, e.g. using the min./exhaled and max./inhaled bellows readings recorded during training and checking that each element of the solution vector satisfies the two conditions: a) $|\boldsymbol{i_{s|o}} + p_{min}\mathbf{c_\chi}| < \boldsymbol{i_{max}}$; b) $|\boldsymbol{i_{s|o}} + p_{max}\mathbf{c_\chi}| < \boldsymbol{i_{max}}$

Figure 6.4 demonstrates the effect of real-time shimming using the 8-channel coil on multi-echo GRE acquired in vivo. Note that a constant field offset corresponding to a Tx frequency adjustment was included in the optimization (i.e. as an extra column of ones in the matrix operator $\boldsymbol{A}$ in Eq. [6.3]) but only for the static term, as dynamic Tx frequency adjustment was not a readily accessible feature. Inclusion of the extra term is critical for the single-turn AC/DC coils

as the field shift achievable from each element is small and current needs to be apportioned carefully. Otherwise, when this constant static term is neglected in the optimization, it seems much of the optimized currents tend to go toward an unnecessary static self-correction (e.g. some coils only serving to compensate the ΔB_0 effects of other coils) and little to no current ends up being prescribed for the RIRO correction. By including all available static correction terms (e.g. scanner shims) in the optimization (i.e. again by incorporating the corresponding shim profiles into additional columns of $\boldsymbol{A}$) not only should the static shim improve but, insofar as it frees up additional current, the real-time RIRO correction afforded by the AC/DC coil should also improve. Joint shim optimizations using additional terms are demonstrated in the next section.

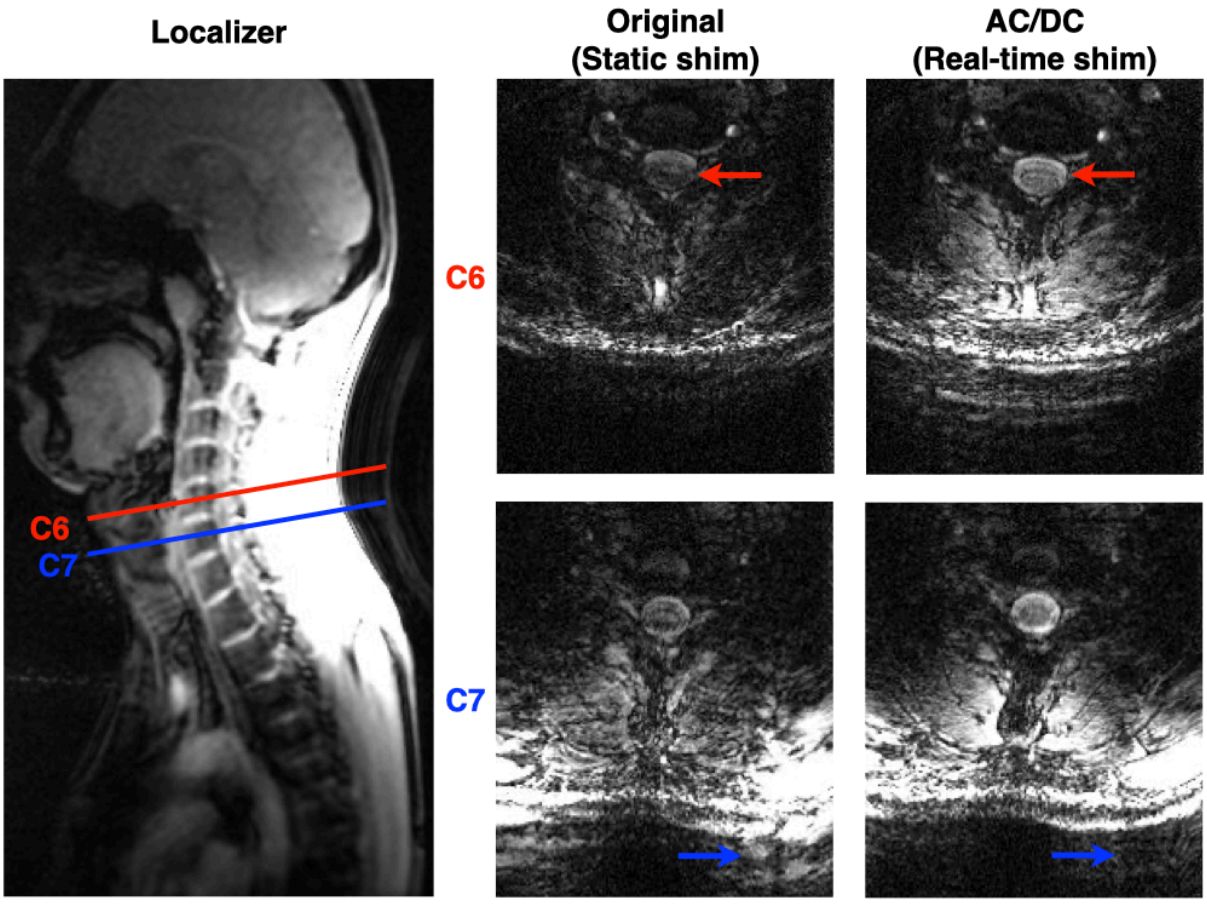

Figure 6.4 Real-time shimming axial GRE (TE=24.46 ms) of the cervical spinal cord with the 8-channel AC/DC coil. Reduced T2*-dephasing is appreciable at vertebral level C6 (red arrows) and reduced ghosting is evident at the back of the neck in the slice covering C7 (blue arrows).

6.2 A 15-channel AC/DC coil for the cervical spinal cord

Due to the narrowness of the spinal cord in cross-section, high-resolution is often desirable and this is more readily obtained at higher field strengths. To this end, Lopez-Rios et al. (121) designed a 15-channel C-spine Rx coil for 7T, which has since been adapted to include five additional Rx channels. While the coil geometry was designed specifically for B_1 receive functionality, we performed an initial experiment to assess its capability for shimming, to be described in the following.

To simulate shim performance for both static ΔB_0 and respiration-induced resonance offsets (RIRO), gradient-echo field maps of six adult subjects were acquired on a Prisma-fit system (Siemens Healthineers, Erlangen, Germany) with subjects positioned in the 3D-printed ΔB_0/Rx coil former. Using the body coil for both excitation and reception, GRE field maps were acquired over inspired and expired breath-hold conditions while a set of bellows recorded a respiratory signal. Static ΔB_0 and RIRO fields in Hz were calculated for each subject and scaled by the nominal ratio of the system field strengths (7/2.89). As illustrated in Figure 6.5, image and CAD coordinates were aligned and shim field profiles in Hz/A were computed at the image voxel positions using a MATLAB program based on the Biot-Savart law (Eq. [1.9]). Finally, shim currents (constrained to $\leq$ 2.5A absolute current per channel) were optimized for each subject, simultaneously minimizing static ΔB_0 and RIRO over an extended region encompassing the cervical and upper thoracic spinal cord. For comparison, equivalent optimizations were also performed: first, using the standard spherical harmonic basis up to 2nd order; and, again, via joint-optimization, optimizing both the standard 0th-2nd order shims and the custom 15-channel simultaneously.

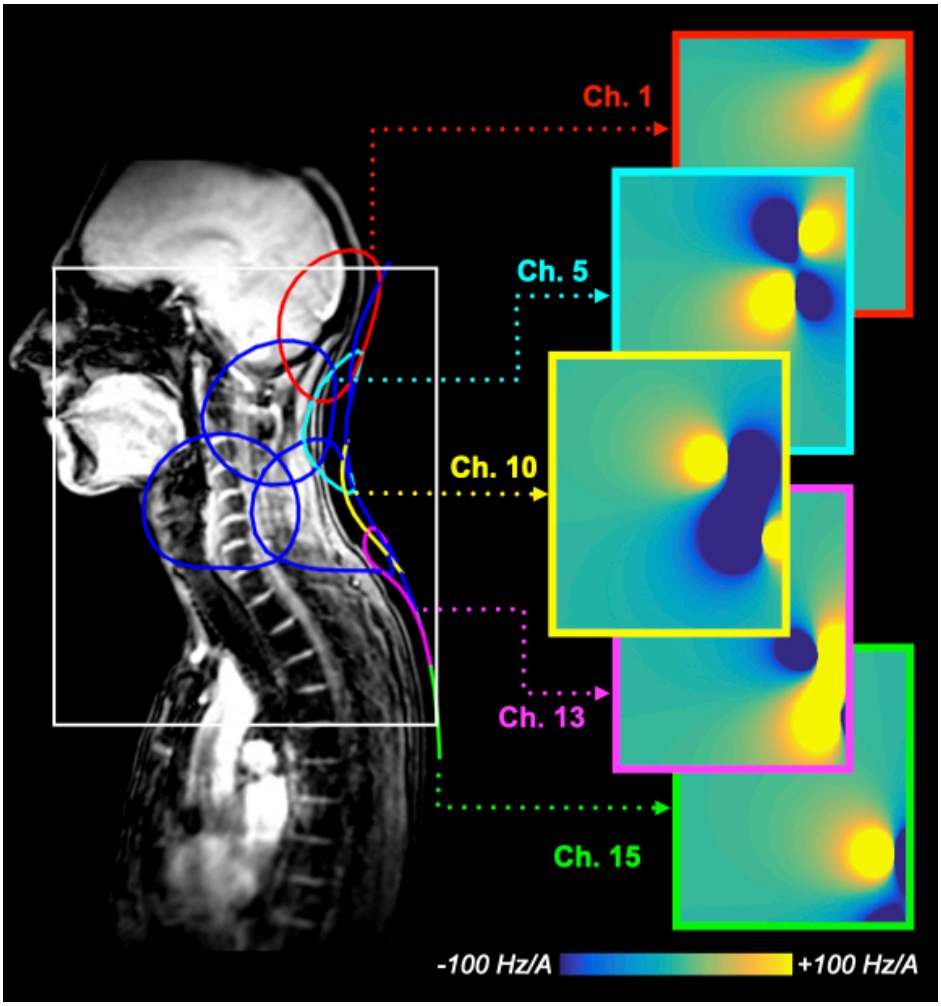

Figure 6.5 Simulated field profiles for five elements of the 15-channel AC/DC coil. Vitamin E capsules (hidden by the coil overlay in the current figure) were positioned on the posterior surface of the coil former at the centres of the medial coils (Ch. 2, Ch. 10, Ch. 15) to provide fiducial markers by which the coil geometry (exported from CST) was matched to the acquired DICOM images. Shim field profiles were then generated over the FOV (boxed region) for each in vivo participant.

The results of the shim simulations are summarized in Figure 6.6. Across the shim volume of interest (VOI) and across subjects, the 15-channel array, when combined with a global (0^{th} order) correction, reduced the mean static ΔB_0 inhomogeneity (i.e. standard deviation) from 253±23 Hz using 0^{th}-2^{nd} order spherical harmonics down to 171±14 Hz (average improvement: 32±3%). Regarding the RIRO correction, the two shim systems perform similarly: 0^{th}-2^{nd} spherical

harmonics reduced the root-mean-square (RMSE) RIRO by 29±6% versus the 27±6% reduction achieved using the 15-channel array and global offset.

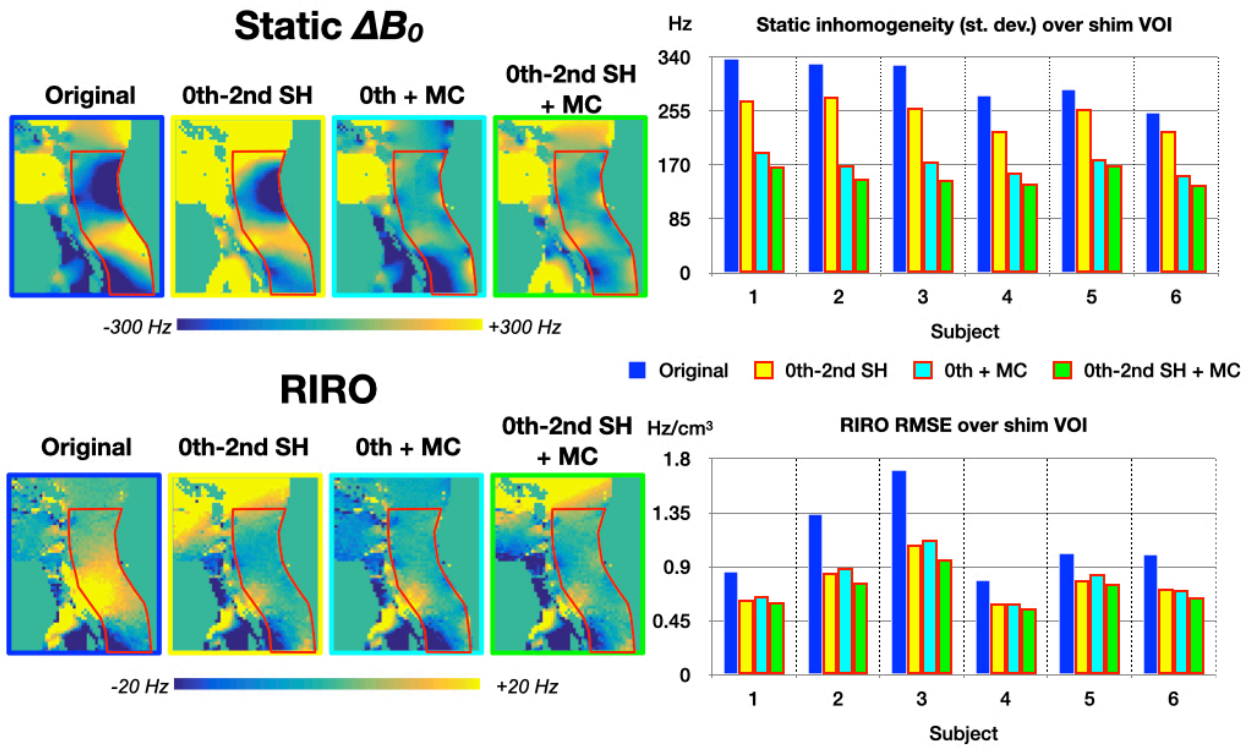

Figure 6.6 Simulation results shimming with the 15-channel AC/DC multi-coil (**MC**). Static ΔB_0 (top) and respiration-induced resonance offsets (RIRO, bottom) under 4 conditions: (i) The acquired fields scaled to 7 T (**Original**); (ii) optimized using ideal spherical harmonics up to second order (**0th-2nd SH**); (iii) optimized using the 15-channel multi-coil along with a global frequency offset (**0th + MC**); and (iv) optimized concurrently using all terms (**0th-2nd SH + MC**). Optimizations were restricted to the shim volume of interest (red outline) which was similar across subjects. The left panel exhibits the results for the same subject shown in the previous figure. The right panel summarizes results across subjects.

Two results are of note. First, for the static correction, standard shimming was outperformed by the 15-channel AC/DC array—a repurposed Rx array for which shim performance had not been considered when designing the coil arrangement. Second, the best corrections were obtained when all shims—local coils and standard spherical harmonics—were marshalled together. This

suggests that future improvements may be gained by integrating both local and global approaches to the design of shim coils.

6.3 Software: *Shimming Toolbox*

Although it has received little attention, software development was a major component of this research project. As the shim systems used were unique prototypes that had to be operated independently from the MRI scanner, a considerable amount of auxiliary software had to be developed for the equipment to be of any practical use. For instance, although a rudimentary PC program was provided by Resonance Research Inc. which enabled a user to manually set the shim currents of their 24-channel system one channel at a time, it was immediately evident that the program would be inadequate for our planned in vivo experiments: not only was the process of manually updating the channels slow and error-prone, more importantly, the program did not include any optimization functionality (i.e. neither for producing field maps, nor for target-volume selection, nor for determining the appropriate correction currents). To each of these ends, new computer programs were written even for our earliest (and most elementary (78)) shim experiments. Later, with the development of the custom AC/DC arrays, it was necessary to adapt and extend the software to be compatible with new systems.

To help the next generation of shim researchers avoid reinventing the wheel, we have recently released a version of these programs as the open-source *Shimming Toolbox* (https://shimming-toolbox.org/). Figure 6.7 highlights several functionalities of the software, which was recently presented at ISMRM (122). The hope is not only for the software to be useful in itself, but that the public release of documented and version-controlled source code will assist in the preservation and transfer of technical knowledge which, unless published in an official journal, often gets lost.

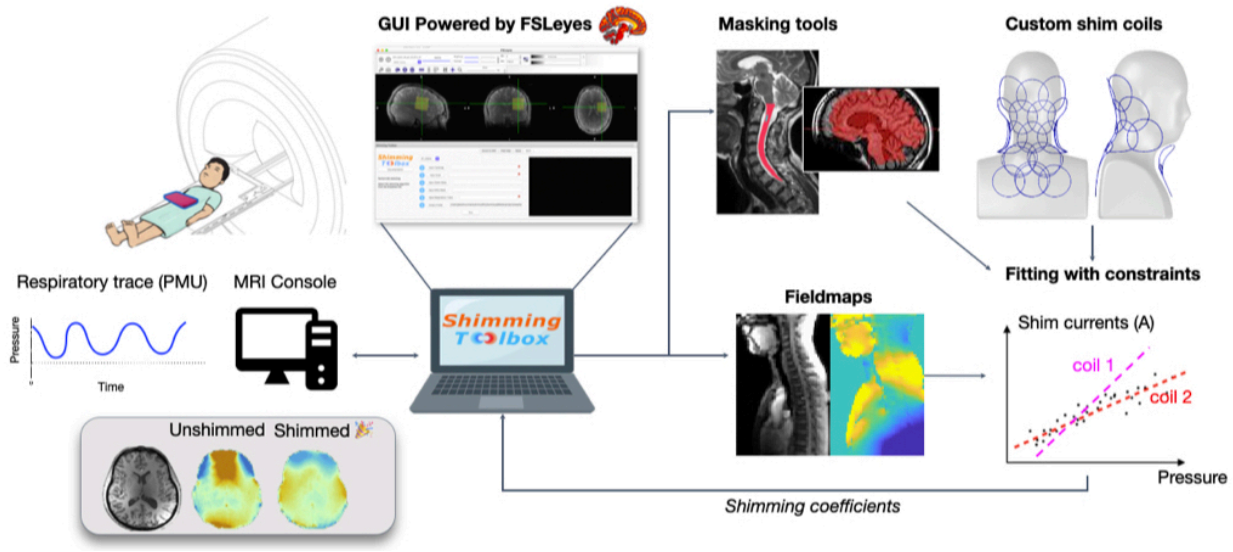

Figure 6.7 Overview of *Shimming Toolbox* functionalities, adapted from (122).

CHAPTER 7 CONCLUSION AND RECOMMENDATIONS

In this work, we sought to develop new approaches to B_0 shimming in the spinal cord. We began with the formulation, restated from Chapter 1:

> As ΔB_0 distortions arise locally in space ($\propto 1/R^3$) and change locally in time, we hypothesize that *shimming* too—in terms of coil placement and in terms of the temporal optimization of currents—should likewise be done *locally*.

Thus, our investigations developed from two basic premises:

1. Arrays of local, non-orthogonal shim coils could improve B_0 field uniformity in the spinal cord.
2. B_0 uniformity could be better maintained than with the usual static shim by synchronizing shim updates to the respiratory cycle of the subject—namely, by *real-time shimming*.

The following briefly recapitulates the main findings of our investigations.

In our first study, Chapter 4, we introduced a local 24-channel shim array for the thoracic spinal cord along with a targeted approach to shimming whereby the *Spinal Cord Toolbox* was used to automatically select the spinal cord region over which the local shims were optimized. Our main findings:

1. Local shimming considerably outperformed standard shimming on the MRI scanner; however, simulations suggested that differences in how the two shim systems were optimized (e.g. target region selection) may have been more significant than differences in shim hardware.
2. When shimming "globally" along the length of the cord, even when the optimization was confined to the spinal cord region, neither shim system could adequately address the highly localized static field deviations associated with the vertebra of the spine. For the latter, slice-wise ("dynamic") shimming is necessary.

In our second study, Chapter 5, we introduced a prospective/real-time shim correction for respiration-induced resonance offsets, and we demonstrated the correction using the 24-channel local shim array. Our main findings:

1. Field homogeneity and stability improved with real-time shimming; consequently, GRE-EPI was made more robust to the effects of breathing, exhibiting less geometric distortion and possessing better temporal SNR.
2. Simulations showed the local shim array was at least as effective at eliminating field inhomogeneities associated with respiration as an ideal set of 0^{th}-4^{th} order spherical harmonic shims.

In Chapter 6, we proposed improvements to the real-time shimming technique: we showed how the training stage for real-time shimming can be facilitated by measuring field maps during free-breathing as opposed to during extended breath-holds. We further introduced two designs of integrated "AC/DC" arrays for the neck where Rx coils double as local shim elements. Also, we extended the shim optimization to include spherical harmonic as well as local shim terms. Our main findings:

1. Despite prioritizing Rx performance in the array geometry, and each coil element consisting of a single-turn, appreciable improvements to static and real-time shim performance were achievable with both 8- and 15-channel AC/DC designs.
2. Best results were obtained when local and standard spherical harmonic shim terms were jointly optimized; however, residual fields persisted, hence, there is still room for new and improved designs!

In the final analysis, we have demonstrated that alternative approaches to shimming (coil technologies, and how shims are operated) can outperform conventional static shimming with low-order spherical harmonics. However, for the 24-channel system, this came at the cost of inferior RF/imaging performance. Future efforts to improve shimming would therefore do well to treat the problem in the larger context of imaging, shims being but one component of a complex system.

As new ideas for how to innovate MRI become more ambitious—for instance, when they involve redesigning and reintegrating multiple subsystems—collaboration among different teams of researchers will be increasingly important. In this way, open-science practices such as data-sharing and open-source software development will be especially useful.

REFERENCES

1. Noonan VK, Fingas M, Farry A, et al. Incidence and prevalence of spinal cord injury in Canada: A national perspective. Neuroepidemiology 2012;38:219–226.

2. Vanderby S, Badea A, Peña Sánchez JN, Kalra N, Babyn P. A Day in the Life of MRI: The Variety and Appropriateness of Exams Being Performed in Canada. Can Assoc Radiol J 2018;69:151–161.

3. Jacobs JC, Jarvik JG, Chou R, et al. Observational Study of the Downstream Consequences of Inappropriate MRI of the Lumbar Spine. J Gen Intern Med 2020;35:3605–3612.

4. Sharma S, Traeger AC, Reed B, et al. Clinician and patient beliefs about diagnostic imaging for low back pain: a systematic qualitative evidence synthesis. BMJ Open 2020;10:e037820.

5. Stroman PW, Wheeler-Kingshott C, Bacon M, et al. The current state-of-the-art of spinal cord imaging: methods. Neuroimage 2014;84:1070–81.

6. Martin AR, Leener B De, Cohen-adad J, et al. Monitoring for myelopathic progression with multiparametric quantitative MRI. 2018:1–17.

7. Cohen-Adad J, El Mendili MM, Lehéricy S, et al. Demyelination and degeneration in the injured human spinal cord detected with diffusion and magnetization transfer MRI. Neuroimage 2011;55:1024–1033.

8. Haase A, Frahm J, Matthaei D, Merboldt K. FLASH Imaging . Rapid NMR Imaging Using Low Flip-Angle Pulses. 1986;266:258–266.

9. Schenck JF. The role of magnetic susceptibility in magnetic resonance imaging: MRI magnetic compatibility of the first and second kinds. Med Phys 1996;23:815–850.

10. Salomir R, de Senneville BD, Moonen CT. A fast calculation method for magnetic field inhomogeneity due to an arbitrary distribution of bulk susceptibility. Concepts Magn Reson 2003;19B:26–34.

11. Marques JP, Bowtell R. Application of a Fourier-based method for rapid calculation of field inhomogeneity due to spatial variation of magnetic susceptibility. Concepts Magn Reson Part B Magn Reson Eng 2005;25B:65–78.

12. Lee G, Jordan C, Tiet P, et al. Improved frequency selective fat suppression in the posterior neck with tissue susceptibility matched pyrolytic graphite foam. J Magn Reson Imaging 2015;41:684–693.

13. Cooke FJ, Blamire AM, Manners DN, Styles P, Rajagopalan B. Quantitative proton magnetic resonance spectroscopy of the cervical spinal cord. Magn Reson Med 2004;51:1122–1128.

14. Vannesjo SJ, Miller KL, Clare S, Tracey I. Spatiotemporal characterization of breathing-induced B0 field fluctuations in the cervical spinal cord at 7T. Neuroimage 2018;167:191–202.

15. Verma T, Cohen-Adad J. Effect of respiration on the B0 field in the human spinal cord at 3T. Magn Reson Med 2014;72:1629–36.

16. Jezzard P, Balaban RS. Correction for geometric distortion in echo planar images from B0 field variations. Magn Reson Med 1995;34:65–73.

17. van Gelderen P, de Zwart JA, Starewicz P, Hinks RS, Duyn JH. Real-time shimming to compensate for respiration-induced B0 fluctuations. Magn Reson Med 2007;57:362–8.

18. Saritas E, Holdsworth S, Bammer R. Susceptibility Artifacts. In: Cohen-Adad J, Wheeler-Kingshott C, editors. Quantitative MRI of the Spinal Cord. 1st ed. Elsevier; 2014. pp. 91–104.

19. Wang J, Mao W, Qiu M, Smith MB, Constable RT. Factors influencing flip angle mapping in MRI: RF pulse shape, slice-select gradients, off-resonance excitation, and B0 inhomogeneities. Magn Reson Med 2006;56:463–468.

20. Littin S, Jia F, Layton KJ, Zaitsev M, Kroboth S, Yu H. Development and Implementation of an 84-Channel Matrix Gradient Coil. 2017;00:1–11.

21. Deshmane A, Gulani V, Griswold MA, Seiberlich N. Parallel MR imaging. J Magn Reson Imaging 2012;36:55–72.

22. Breuer F a., Blaimer M, Heidemann RM, Mueller MF, Griswold M a., Jakob PM. Controlled aliasing in parallel imaging results in higher acceleration (CAIPIRINHA) for multi-slice imaging. Magn Reson Med 2005;53:684–691.

23. Pruessmann KP, Weiger M, Scheidegger MB, Boesiger P. SENSE: sensitivity encoding for fast MRI. Magn Reson Med 1999;42:952–62.

24. Schallmo M, Weldon KB, Burton PC, Sponheim SR, Olman CA. Assessing methods for

geometric distortion compensation in 7 T gradient echo functional MRI data. Hum Brain Mapp 2021:1–41.

25. Robinson S, Jovicich J. B0 Mapping With Multi-Channel RF Coils at High Field. 2011;c:976–988.

26. Robinson S, Grabner G, Witoszynskyj S, Trattnig S. Combining phase images from multi-channel RF coils using 3D phase offset maps derived from a dual-echo scan. Magn Reson Med 2011;65:1638–48.

27. Robinson SD, Dymerska B, Bogner W, et al. Combining phase images from array coils using a short echo time reference scan (COMPOSER). Magn Reson Med 2017;77:318–327.

28. Abdul-Rahman HS, Gdeisat M a, Burton DR, Lalor MJ, Lilley F, Moore CJ. Fast and robust three-dimensional best path phase unwrapping algorithm. Appl Opt 2007;46:6623–35.

29. Witoszynskyj S, Rauscher A, Reichenbach JR, Barth M. Phase unwrapping of MR images using Phi UN--a fast and robust region growing algorithm. Med Image Anal 2009;13:257–68.

30. Jenkinson M. Fast, automated, N-dimensional phase-unwrapping algorithm. Magn Reson Med 2003;49:193–7.

31. Knight WD. Nuclear Magnetic Resonance Shift in Metals. Phys Rev 1949;76:1259–1260.

32. Dickinson WC. Dependence of the F19 nuclear resonance position on chemical compound. Phys Rev 1950;77:736–737.

33. Proctor WG, Yu FC. The Dependence of a Nuclear Magnetic Resonance Frequency upon Chemical Compound. Phys Rev 1950;77:717.

34. Arnold JT, Dharmatti SS, Packard ME. Chemical effects on nuclear induction signals from organic compounds. J Chem Phys 1951;19:507.

35. Arnold JT. Magnetic Resonances of Protons in Ethyl Alcohol. Phys Rev 1956;102:136–150.

36. Hahn EL. Nuclear induction due to free larmor precession. Phys Rev 1950;77:297–298.

37. Anderson WA. Electrical Current Shims for Correcting. Rev Sci Instrum 1961;32:241.

38. Carr HY, Purcell EM. Effects of Diffusion on Free Precession in Nuclear Magnetic Resonance Experiments. Phys Rev 1954;94:630–638.

39. Carr HY. Field Gradients in Early MRI. Phys Today 2004;57:83–83.

40. Nelson FA. US patent no. 2858504; 1958.

41. Jaynes ET. US patent no. 3566255; 1971.

42. Golay MJE. Field Homogenizing Coils for Nuclear Spin Resonance Instrumentation. Rev Sci Instr 1958;29:313–15.

43. Golay MJE. US patent no. 3515979; 1957.

44. Romeo F, Hoult DI. Magnet field profiling: Analysis and correcting coil design. Magn Reson Med 1984;1:44–65.

45. Koch KM, Rothman DL, de Graaf R a. Optimization of static magnetic field homogeneity in the human and animal brain in vivo. Prog Nucl Magn Reson Spectrosc 2009;54:69–96.

46. Juchem C, de Graaf RA. B0 magnetic field homogeneity and shimming for in vivo magnetic resonance spectroscopy. Anal Biochem 2017;529:17–29.

47. Pan JW, Lo K-M, Hetherington HP. Role of very high order and degree B0 shimming for spectroscopic imaging of the human brain at 7 tesla. Magn Reson Med 2012;68:1007–17.

48. Bottomley PA. A versatile magnetic field gradient control system for NMR imaging. J Phys E 1981;14:1081–1087.

49. Mansfield P, Chapman B. Active magnetic screening of coils for static and time-dependent magnetic field generation in NMR imaging. J Phys E 1986;19:540–545.

50. Turner R. Minimum inductance coils. J Phys E Sci Instrum 1988;21:948–952.

51. Turner R. Gradient coil design: A review of methods. Magn Reson Imaging 1993;11:903–920.

52. Glover GH. 3D z-shim method for reduction of susceptibility effects in BOLD fMRI. Magn Reson Med 1999;42:290–9.

53. Gu H, Feng H, Zhan W, et al. Single-shot interleaved z-shim EPI with optimized compensation for signal losses due to susceptibility-induced field inhomogeneity at 3 T. Neuroimage 2002;17:1358–1364.

54. Ward HA, Riederer SJ, Jack CR. Real-time autoshimming for echo planar timecourse

imaging. Magn Reson Med 2002;48:771–780.

55. Raj D, Paley DP, Anderson a W, Kennan RP, Gore JC. A model for susceptibility artefacts from respiration in functional echo-planar magnetic resonance imaging. Phys Med Biol 2000;45:3809–3820.

56. Van de Moortele P-F, Pfeuffer J, Glover GH, Ugurbil K, Hu X. Respiration-induced B0 fluctuations and their spatial distribution in the human brain at 7 Tesla. Magn Reson Med 2002;47:888–895.

57. Koch KM, McIntyre S, Nixon TW, Rothman DL, de Graaf R a. Dynamic shim updating on the human brain. J Magn Reson 2006;180:286–296.

58. Blamire AM, Rothman DL, Nixon T. Dynamic shim updating: A new approach towards optimized whole brain shimming. Magn Reson Med 1996;36:159–165.

59. Finsterbusch J, Sprenger C, Büchel C. Combined T2*-weighted measurements of the human brain and cervical spinal cord with a dynamic shim update. Neuroimage 2013;79:153–61.

60. Finsterbusch J, Eippert F, Büchel C. Single, slice-specific z-shim gradient pulses improve T2*-weighted imaging of the spinal cord. Neuroimage 2012;59:2307–15.

61. Vannesjo SJ, Shi Y, Tracey I, Miller KL, Clare S. Slice-wise first-order shimming of the human spinal cord at 7T. 2017:3–5.

62. Vannesjo SJ, Duerst Y, Vionnet L, et al. Gradient and shim pre-emphasis by inversion of a linear time-invariant system model. Magn Reson Med 2017;78:1607–1622.

63. Juchem C, Nixon TW, McIntyre S, Rothman DL, de Graaf R a. Magnetic field homogenization of the human prefrontal cortex with a set of localized electrical coils. Magn Reson Med 2010;63:171–180.

64. Juchem C, Brown PB, Nixon TW, McIntyre S, Rothman DL, De Graaf R a. Multicoil shimming of the mouse brain. Magn Reson Med 2011;66:893–900.

65. Juchem C, Green D, de Graaf R a. Multi-coil magnetic field modeling. J Magn Reson 2013;236:95–104.

66. Biber S, Wohlfarth K, Kirsch J, Schmidt A. Design of a local shim coil to improve B0 homogeneity in the cervical spine region. In: Proceedings of the 20th Annual Meeting of

ISMRM, Melbourne, Australia, 2012. Abstract 2746.

67. Siemens-Healthineers. MAGNETOM Flash MAGNETOM Vida and BioMatrix special issue. Magnetom Flash 2017.

68. Stockmann JP, Witzel T, Keil B, et al. A 32-channel combined RF and B0 shim array for 3T brain imaging. Magn Reson Med 2016;75:441–451.

69. Truong T, Darnell D, Song AW. NeuroImage Integrated RF / shim coil array for parallel reception and localized B 0 shimming in the human brain. Neuroimage 2014;103:235–240.

70. Topfer R, Starewicz P, Lo K-M, et al. A 24-channel shim array for the human spinal cord: Design, evaluation, and application. Magn Reson Med 2016;76:1604–1611.

71. Topfer R, Foias A, Stikov N, Cohen-Adad J. Real-time correction of respiration-induced distortions in the human spinal cord using a 24-channel shim array. Magn Reson Med 2018;80:935–946.

72. De Tillieux P, Topfer R, Foias A, et al. A pneumatic phantom for mimicking respiration-induced artifacts in spinal MRI. Magn Reson Med 2018;79:600–605.

73. Hillenbrand DF, Lo KM, Punchard WFB, Reese TG. Applied magnetic resonance high-order MR shimming: a simulation study of the effectiveness of competing methods, using an established susceptibility model of the human head. Appl Magn Reson 2005;29:39–64.

74. Juchem C, Nixon TW, McIntyre S, Boer VO, Rothman DL, de Graaf R a. Dynamic multi-coil shimming of the human brain at 7 T. J Magn Reson 2011;212:280–8.

75. Juchem C, Umesh Rudrapatna S, Nixon TW, de Graaf R a. Dynamic multi-coil technique (DYNAMITE) shimming for echo-planar imaging of the human brain at 7 Tesla. Neuroimage 2015;105:462–472.

76. Han H, Song AW, Truong T-K. Integrated parallel reception, excitation, and shimming (iPRES). Magn Reson Med 2013;70:241–7.

77. Hsu JJ, Glover GH. Mitigation of susceptibility-induced signal loss in neuroimaging using localized shim coils. Magn Reson Med 2005;53:243–248.

78. Topfer R, Lo K-M, Metzemaekers K, et al. A 24-channel shim array for real-time shimming of the human spinal cord: Characterization and proof-of-concept experiment. In: Proceedings of

the 23rd Annual Meeting of ISMRM, Toronto, Canada, 2015. Abstract 3083.

79. Topfer R, Germain G, Stockmann JP, et al. Very-high order shimming in the human spinal cord using a dedicated 24-channel array coil. In: Proceedings of the 24th Annual Meeting of ISMRM, Singapore, 2016. Abstract 3628.

80. Kumar A, Edelstein WA, Bottomley PA. Noise figure limits for circular loop MR coils. Magn Reson Med 2009;61:1201–1209.

81. van Zijl PCM, Sukumar S, O'Neil Johnson M, Webb P, Hurd RE. Optimized shimming for high-resolution NMR using three-dimensional image-based field mapping. J Magn Res, Ser A 1994;111:203–207.

82. Li L, Leigh JS. High-precision mapping of the magnetic field utilizing the harmonic function mean value property. J Magn Reson 2001;148:442–8.

83. Sun H, Wilman AH. Background field removal using spherical mean value filtering and Tikhonov regularization. Magn Reson Med 2014;71:1151–1157.

84. Cohen-Adad J, De Leener B, Benhamou M, et al. Spinal Cord Toolbox: an open-source framework for processing spinal cord MRI data. In: Proceedings of the 20th Annual Meeting of OHBM, Hamburg, Germany, 2014. Abstract 3633.

85. De Leener B, Kadoury S, Cohen-adad J. Robust, accurate and fast automatic segmentation of the spinal cord. Neuroimage 2014;98:528–536.

86. Germain G, Stockmann JP, Topfer R, Wald L, Stikov N, Cohen-Adad J. Optimization of geometry for combined RF/shim coil arrays for the spinal cord. In: Proceedings of the 24th Annual Meeting of ISMRM, Singapore, 2016. Abstract 1154.

87. Vannesjo SJ, Eippert F, Kong Y, Clare S, Miller KL, Tracey I. Breathing-induced B0 field fluctuations in the cervical spinal cord at 7T. In: Proceedings of the 24th Annual Meeting of ISMRM, Singapore, 2016. Abstract 49.

88. Boer VO, van de Bank BL, van Vliet G, Luijten PR, Klomp DWJ. Direct B0 field monitoring and real-time B0 field updating in the human breast at 7 Tesla. Magn Reson Med 2012;67:586–91.

89. Boer VO, Luttje MP, Luijten PR, Klomp DWJ. Requirements for static and dynamic higher

order B0 shimming of the human breast at 7 T. NMR Biomed 2014;27:625–31.

90. Zivkovic I, Mirkes C, Scheffler K. B0 shimming at 9.4T using a multicoil approach – coil design with genetic algorithm. In: Proceedings of the 24th Annual Meeting of ISMRM, Singapore, 2016. Abstract 1152.

91. Dagher J, Nael K. MAGPI: A framework for maximum likelihood MR phase imaging using multiple receive coils. Magn Reson Med 2016;75:1218–1231.

92. Robinson S, Schödl H, Trattnig S. A method for unwrapping highly wrapped multi-echo phase images at very high field: UMPIRE. Magn Reson Med 2014;72:80–92.

93. Vannesjo SJ, Miller KL, Clare S, Tracey I. Spatiotemporal characterization of breathing-induced B0 field fluctuations in the cervical spinal cord at 7T S. Neuroimage 2017.

94. Sherman JL, Nassaux PY, Citrin CM. Measurements of the normal cervical spinal cord on MR imaging. Am J Neuroradiol 1990;11:369–372.

95. Saritas EU, Cunningham CH, Lee JH, Han ET, Nishimura DG. DWI of the spinal cord with reduced FOV single-shot EPI. Magn Reson Med 2008;60:468–473.

96. Barry RL, Klassen LM, Williams JM, Menon RS. Hybrid two-dimensional navigator correction: a new technique to suppress respiratory-induced physiological noise in multi-shot echo-planar functional MRI. Neuroimage 2008;39:1142–1150.

97. Cohen-Adad J. Functional MRI of the Spinal Cord: Current Status and Future Developments. Semin Ultrasound, CT MRI 2016.

98. Martin AR, Aleksanderek I, Cohen-Adad J, et al. Translating state-of-the-art spinal cord MRI techniques to clinical use: A systematic review of clinical studies utilizing DTI, MT, MWF, MRS, and fMRI. NeuroImage Clin 2016;10:192–238.

99. Henning A, Schär M, Kollias SS, Boesiger P, Dydak U. Quantitative magnetic resonance spectroscopy in the entire human cervical spinal cord and beyond at 3T. Magn Reson Med 2008;59:1250–1258.

100. Keating B, Ernst T. Real-time dynamic frequency and shim correction for single-voxel magnetic resonance spectroscopy. Magn Reson Med 2012;68:1339–1345.

101. Wilm BJ, Duerst Y, Dietrich BE, et al. Feedback field control improves linewidths in in

vivo magnetic resonance spectroscopy. Magn Reson Med 2014;71:1657–1662.

102. Duerst Y, Wilm BJ, Dietrich BE, et al. Real-Time Feedback for Spatiotemporal Field Stabilization in MR Systems. Magn Reson Med 2015;73:884–893.

103. Duerst Y, Wilm BJ, Wyss M, et al. Utility of real-time field control in T2*-Weighted head MRI at 7T. Magn Reson Med 2016;76:430–439.

104. Juchem C, de Graaf RA. B0 magnetic field homogeneity and shimming for in vivo magnetic resonance spectroscopy. Anal Biochem 2017;529:17–29.

105. Stockmann JP, Wald LL. In Vivo B0 Field Shimming Methods for MRI at 7 T. Neuroimage.

106. Juchem C, de Graaf RA. The public multi-coil information (PUMCIN) policy. Magn Reson Med 2017;78:2042–2047.

107. Vannesjo SJ, Wilm BJ, Duerst Y, et al. Retrospective correction of physiological field fluctuations in high-field brain MRI using concurrent field monitoring. Magn Reson Med 2014;73:1833–1843.

108. Wezel J, Boer VO, van der Velden TA, et al. A comparison of navigators, snap-shot field monitoring, and probe-based field model training for correcting B0-induced artifacts in T2*-weighted images at 7 T. Magn Reson Med 2017;78:1373–1382.

109. De Leener B, Lévy S, Dupont SM, et al. SCT: Spinal Cord Toolbox, an open-source software for processing spinal cord MRI data. Neuroimage 2016;145:24–43.

110. Gros C, Leener B De, Dupont SM, et al. OptiC: Robust and Automatic Spinal Cord Localization on a Large Variety of MRI Data Using a Distance Transform Based Global Optimization. In: Proceedings of the 20th International Conference on Medical Image Computing and Computer-Assisted Intervention, Quebec City, MICCAI 2017. Vol. 10434. ; pp. 712–719.

111. Topfer R, Foias A, Stikov N, Cohen-Adad J. Real-time shimming of the human spinal cord using a 24-channel shim array coil. In: Proceedings of the 25th Annual Meeting of ISMRM, Honolulu, 2017. Abstract 964.

112. De Zanche N, Barmet C, Nordmeyer-Massner J a., Pruessmann KP. NMR Probes for measuring magnetic fields and field dynamics in MR systems. Magn Reson Med 2008;60:176–186.

113. Haeberlin M, Kasper L, Barmet C, et al. Real-time motion correction using gradient tones and head-mounted NMR field probes. Magn Reson Med 2015;74:647–660.

114. Bianciardi M, Polimeni JR, Setsompop K, Eichner C, Bilgic B, Wald LL. Evaluation of dynamic off-resonance correction of respiratory instability in MRI signals for high-order spherical harmonic basis set and multivariate modeling of respiratory sources. In: Proceedings of the 22nd Annual Meeting of ISMRM, Milan, 2014. Abstract 1623.

115. Stockmann J, Witzel T, Arango N, et al. An Integrated 32ch RF-Shim Array Coil for Improved B0 Shimming of the Brain at 7 Tesla. In: Proceedings of the 25th Annual Meeting of ISMRM, Honolulu, 2017. Abstract 967.

116. Wilson JL, Jezzard P. Utilization of an Intra-Oral Diamagnetic Passive Shim in Functional MRI of the Inferior Frontal Cortex. Magn Reson Med 2003;50:1089–1094.

117. Stockmann JP, Wald LL. In vivo B0field shimming methods for MRI at 7 T. Neuroimage 2018;168:71–87.

118. Topfer R, Foias A, Rios NL, et al. Integrated ΔB0/Rx coil array for improved spinal cord imaging at 3T. In: Proceedings of the 26th Annual Meeting of ISMRM, Paris, France, 2018. Abstract 8930.

119. Topfer R, Rios NL, Foias A, Arango N, Wald LL, Stockmann JP. Real-time shimming in the cervical spinal cord using an 8-channel AC / DC array and a capacitive respiratory sensor. In: Proceedings of the 27th Annual Meeting of ISMRM, Montreal, Canada, 2019. Abstract 0925.

120. Power JD, Lynch CJ, Silver BM, Dubin MJ, Martin A, Jones RM. Distinctions among real and apparent respiratory motions in human fMRI data. Neuroimage 2019;201:116041.

121. Rios NL, Topfer R, Foias A, et al. Integrated AC/DC coil and dipole Tx array for 7T MRI of the spinal cord. In: Proceedings of the 27th Annual Meeting of ISMRM, Montreal, Canada, 2019. Abstract 0220.

122. Astous AD, Topfer R, Cereza G, et al. Shimming-Toolbox: An open-source software package for performing realtime B0 shimming experiments. In: Proceedings of the 29th Annual Meeting of ISMRM, 2021. Abstract 3111.